

**A Neuromuscular Junction-Based Neural Interface:
The Myotube-integrated Microelectrode Array**

By

Christopher Gresham Langhammer

A Dissertation submitted to the

Graduate School-New Brunswick

Rutgers, The State University of New Jersey

and

The Graduate School of Biomedical Sciences

University of Medicine and Dentistry of New Jersey

in partial fulfillment of the requirements

for the degree of

Doctor of Philosophy

Graduate Program in Biomedical Engineering

written under the direction of

Dr. Bonnie L. Firestein

and approved by

New Brunswick, New Jersey

October, 2010

©2010

Christopher Gresham Langhammer

ALL RIGHTS RESERVED

Abstract of the Dissertation

A Neuromuscular Junction-Based Neural Interface: The Myotube-Integrated Microelectrode Array

By Christopher Gresham Langhammer

Dissertation Director:

Dr. Bonnie Firestein

Neural interface designs are diverse, including multiple cortical, deep brain, spinal, non-invasive, and PNS-based approaches to stimulation and recording. There are an estimated 1.7 million Americans living with limb loss, and many more suffering from PNS injury without expected motor recovery, who may benefit from a neural interface that can help place a prosthetic actuator directly under neural control. Technologies exist capable of recording neural activity from both the PNS and CNS, but they face problems acquiring large enough numbers of independent and appropriately tuned neural signals to provide reliable dexterous control. This dissertation introduces a new neural interface design that uses myotubes cultured on a topographically modified MEA as a means of extracting large numbers of independent neural signals pertaining to motor control from the PNS. To provide proof of principal for the basic science concepts underpinning this design, the following three aims are pursued and results are discussed:

Aim 1 – To develop a bio-interface capable of modulating myotube behavior and guiding myotube formation and contractility to specific locations.

Aim 2 – To integrate the bio-interface from Aim 1 with a substrate-embedded MEA for the purpose of recording myotube activity selectively from independent myotubes within a culture.

Aim 3 – To integrate the interface designed in Aims 1 and 2 with neuronal culture, as the first step towards developing a structured co-culture system.

Acknowledgements

I would like to thank my advisor, Dr. Bonnie Firestein, as well as all members of the Firestein Laboratory for their contributions to this work. Special thanks go out to Melinda Kutzing, Vincent Luo, Anthony Ferrer, Miki Quin, and Sylvia Kim, whose advice and assistance was crucial to the completion of much of this work.

I would additionally like to thank Dr. Zahn and all members of the Zahn laboratory for their assistance, especially Larry Sassou, Mercedes Moralez, and Jean Lo.

Finally, I would like to thank my friends and family, whose love and support ultimately underlie all of my scientific success.

Much of the work herein is being prepared for, or has been accepted for, publication in a variety of formats. I would like to acknowledge the efforts of all who assisted, and continue to assist, our efforts to make this work accessible to the scientific community (as in [1, 2]).

Specific Aims

The ideal neural interface is a bidirectional transducer that establishes contact between a technical device and neural structures within the body. The objective of such devices is to record bioelectrical signals from the nervous system or to implant such signals in order to restore motor and sensory function in disabled patients [3, 4]. Research in the fields of neural interfaces and neural prostheses focuses on restoring motor and sensory function in patients with limb amputations [5, 6], spinal cord injury (SCI) [7, 8], stroke [4, 9], and degenerative diseases [3, 4, 9]. However, advances in these fields have thus far translated into only modest clinical improvements despite the technologies' tremendous potential [10]. A modification of the known "cultured-probe" design, a neural interface in which neurons cultured directly onto an electrode surface prior to implantation facilitate incorporation into the host nervous system [11-13], may significantly improve the recording capabilities of current neural interfaces. By using myotubes rather than neurons as the electrogenic cell type cultured onto the electrode surface and by targeting the peripheral nervous system (PNS) as the implantation site, we hope to overcome many of the critical barriers to progress in this field. This project aims to develop a modified planar microelectrode array (MEA) designed to facilitate integration of muscle cells (myotubes) grown in culture. The MEA surface will be tailored specifically to improve the sealing between myotubes and electrodes for improvement upon the ability of current devices to distinguish electrical activity of individual cells. Principles of this new interface will be developed to optimize the specificity with which the myotubes are able to interact with the electrodes, including the development of computational algorithms meant to interpret the multi-modal data a prototype is likely to generate. These myotubes may then act as biological signal amplifiers for action

potentials received from regenerated motor neuron axons following amputation, creating a gateway for acquiring motor intention from the nervous system. We are using a highly reductionist approach to a complex clinical problem to demonstrate that recording motor intention along its final common pathway is an achievable goal.

HYPOTHESIS: An MEA can be designed to guide myotube formation to specific sites and can interact with these myotubes (recording or stimulating) in a selective manner. It may be possible to use this technology in a novel type of neural interface or in development of laboratory systems requiring the study of ordered muscle cell cultures or muscle/nerve co-cultures.

To demonstrate the ability of myotubes to transduce APs transmitted along α -motoneuron axons, we propose the following aims:

Aim 1 – To develop a bio-interface capable of modulating myotube behavior and guiding myotube formation and contractility to specific locations, while maximizing the number of independently active myotubes.

Aim 2 – To integrate this bio-interface with a substrate-embedded MEA for the purpose of recording myotube activity selectively from independent myotubes within a culture.

Aim 3 – To integrate the interface designed in Aims 1 and 2 above with neuronal culture, as the first step towards developing a co-culture system in which we can observe the transmission of action potentials from a neuronal population to a myotube population.

Table of Contents

Abstract of the Dissertation.....	ii
Acknowledgements.....	iv
Specific Aims.....	v
Table of Contents	vii
List of Illustrations	xiii
 1 Introduction: a review of current technology in neural interfaces and the health relevance of the myo-MEA.....	 1
1.1 Current state of neural interface technology	1
1.1.1 Abstract:	1
1.1.2 Acquiring Neural Signals Related to Motor Intention:	1
1.1.3 CNS Interfaces:.....	4
1.1.4 PNS Interfaces:	4
1.1.5 EMG Surface Interfaces:.....	6
1.2 The myotube-integrated MEA (myo-MEA) as a next step	8
 2 Developing and characterizing novel tools for quantifying muscle cell and neuronal behaviors	 10
2.1 Identification and quantification of skeletal myotube contraction and association in vitro by video microscopy	10
2.1.1 Abstract:	10

2.1.2	Introduction:	11
2.1.3	Materials & Methods:	13
2.1.3.1	Cell Culture	13
2.1.3.2	In Vitro Video Capture & Synthetic Data Generation	14
2.1.3.3	Automated Data Analysis	16
2.1.3.4	Validation of VTA Program Performance on In Vitro and Synthetic Data	23
2.1.4	Results:	25
2.1.4.1	Analysis of In Vitro Video Data	25
2.1.4.2	Single Object Identification	26
2.1.4.3	Multiple Object Identification	28
2.1.4.4	Analysis of Example Video Micrographs	28
2.1.5	Conclusion:	30
2.1.5.1	Selection of Processing Steps and Parameter Values	30
2.1.5.2	Sources of Error and Error Reduction	32
2.1.5.3	Implications and Future Directions	33
2.2	Automated Sholl analysis of digitized neuronal morphology at multiple scales:	
	Whole-cell Sholl analysis vs. Sholl analysis of arbor sub-regions	35
2.2.1	Abstract:	35
2.2.2	Introduction:	36
2.2.3	Materials & Methods:	39
2.2.3.1	Cell Culture & Imaging	39
2.2.3.2	Program Mechanics & Usage	40
2.2.3.3	Branch Identity-specific Data Analysis	43
2.2.4	Results:	45
2.2.4.1	Global analysis:	46
2.2.4.2	Local analysis:	46
2.2.5	Discussion and Conclusions:	47
2.2.5.1	Morphological Analysis:	47
2.2.5.2	Biological Findings:	49
2.2.5.3	Future Directions:	49
2.2.5.4	Conclusions:	50

2.3	Semi-automated spike sorting for increased information retrieval from microelectrode array recordings.....	51
2.3.1	Abstract:	51
2.3.2	Introduction:.....	52
2.3.2.1	<i>A New Type of Data</i>	52
2.3.2.2	<i>Extracellular Voltage Traces (EVTs)</i>	53
2.3.2.3	<i>Spike Sorting Process</i>	56
2.3.2.4	<i>Program Goals</i>	56
2.3.3	Materials & Methods:	57
2.3.3.1	<i>Cell culture and sample data acquisition</i>	57
2.3.3.2	<i>Data analysis</i>	59
2.3.4	Discussion and Results:.....	64
2.3.4.1	<i>Performance Tradeoffs</i>	64
2.3.5	Conclusion:.....	67

3	Tunable culture environments affect myotube and motor neuron behaviors	68
----------	---	-----------

3.1	The effect of microscale grooves on skeletal myotube alignment and independence in a 2D culture system	68
3.1.1	Abstract:	68
3.1.2	Introduction:.....	69
3.1.3	Methods:.....	70
3.1.3.1	<i>Substrate fabrication and characterization</i>	70
3.1.3.2	<i>Myotube isolation and culture</i>	71
3.1.3.3	<i>Quantification of myoblast and myotube alignment</i>	72
3.1.3.4	<i>Quantification of myotube contractility</i>	72
3.1.4	Results and Discussion:.....	74
3.1.4.1	<i>Myotube morphology on PDMS substrates with microscale topographical trenches</i>	74
3.1.4.2	<i>Myotube contractility on PDMS substrates with microscale topographical trenches</i>	78
3.1.4.3	<i>Myotube contractility selectively guided to trenches</i>	81

3.1.5	Conclusions:.....	83
3.2	Spatially selective detection of extracellular action potentials and neurite	
	outgrowth in spinal cord explant culture vs. dissociated neuronal culture.....	86
3.2.1	Abstract:	86
3.2.2	Introduction:.....	87
3.2.3	Methods:.....	88
3.2.3.1	<i>Isolation and culture of spinal cord explants and dissociated neurons</i>	<i>88</i>
3.2.3.2	<i>Immunostaining</i>	<i>89</i>
3.2.3.3	<i>Chemical patterning</i>	<i>90</i>
3.2.3.4	<i>Topographical patterning</i>	<i>90</i>
3.2.3.5	<i>MEA recording and data analysis</i>	<i>91</i>
3.2.4	Results and Discussion:.....	93
3.2.4.1	<i>Spatial localization of EAPs in dissociated cortical vs. spinal cord explant culture.....</i>	<i>93</i>
3.2.4.2	<i>Axonal and dendritic outgrowth from spinal cord explants.....</i>	<i>95</i>
3.2.5	Conclusions:.....	97
4	Myo-MEA design considerations.....	99
4.1	Skeletal myotube integration with planar microelectrode arrays <i>in vitro</i> for	
	spatially selective recording and stimulation: A comparison of neuronal and myotube	
	extracellular action potentials	99
4.1.1	Abstract:	99
4.1.2	Introduction:.....	100
4.1.3	Methods:.....	102
4.1.3.1	<i>Myotube and neuronal isolation and culture</i>	<i>102</i>
4.1.3.2	<i>Acquisition and analysis of electrophysiological data</i>	<i>103</i>
4.1.3.3	<i>Analysis of contractile activity</i>	<i>104</i>
4.1.4	Results & Discussion:	104
4.1.4.1	<i>Myotube vs. neuronal extracellular action potentials</i>	<i>104</i>
4.1.4.2	<i>Myotube network vs. neuronal network activity patterns.....</i>	<i>107</i>
4.1.4.3	<i>Selective stimulation of myotube networks</i>	<i>109</i>

4.1.5	Conclusions:.....	110
4.2	A topographically modified substrate-embedded MEA for directed myotube formation at electrode contact sites.....	112
4.2.1	Abstract:	112
4.2.2	Introduction:.....	113
4.2.3	Methods:.....	115
4.2.3.1	<i>Device fabrication.....</i>	<i>115</i>
4.2.3.2	<i>Myoblast isolation and culture.....</i>	<i>117</i>
4.2.3.3	<i>Electrophysiological and optical data acquisition and analysis.....</i>	<i>117</i>
4.2.4	Results and Discussion:.....	119
4.2.4.1	<i>Device characterization.....</i>	<i>119</i>
4.2.4.1	<i>Myotube formation guided by trenches.....</i>	<i>120</i>
4.2.4.1	<i>Detection of myotube EAPs</i>	<i>121</i>
4.2.4.2	<i>Changes in myotube dynamics due to topographical modification</i>	<i>123</i>
4.2.5	Conclusions:.....	125
4.2.5.1	<i>Structured myotube culture on a topographically modified substrate embedded MEA</i>	<i>125</i>
4.2.5.2	<i>Future Directions.....</i>	<i>125</i>
5	Future directions in co-culture	127
5.1	Spinal cord explant culture on a topographically modified substrate-embedded MEA guides axonal outgrowth and facilitates selective recording: Toward a neuromuscular system on a chip.....	127
5.1.1	Abstract:	127
5.1.2	Introduction:.....	127
5.1.3	Methods:.....	129
5.1.3.1	<i>Cell culture</i>	<i>129</i>
5.1.4	Results:	130
5.1.4.1	<i>Spatial distribution of neuronal and myotube EAP sources sources</i>	<i>130</i>
5.1.5	Discussion and Conclusions:	131

5.1.5.1	<i>Feasibility of detecting information transmission from a neuronal population to a myotube population in structured cocultures.....</i>	<i>131</i>
6	Appendices.....	134
6.1	Protocols.....	134
6.1.1	Myocyte Isolation and Culture Protocol:	134
6.1.2	Freezing Myotubes for “Long-Term” Storage and Thawing for Use:	137
6.1.3	F-10 Based Myocyte Growth Medium:.....	139
6.1.4	Neurobasal (NB) Medium:.....	140
6.1.5	Collagenase – Dispase Preparation Protocol:	142
6.1.6	Immunofluorescence Staining Protocol:	143
6.1.7	Hoechst Staining Protocol:.....	145
6.1.8	Alpha-Bungarotoxin Labeling Protocol:.....	146
6.1.9	Substrate Regeneration (Electrode & Topographical):	148
6.1.10	Plasma Generator Protocol:.....	149
6.1.11	SU-8 Photolithography Protocol:.....	152
6.2	Visual Twitch Analysis Online Supporting Material	159
6.2.1	Description of Success and Failure Metrics.....	159
6.2.2	VTA Program Analysis of TTX Treatment on Spontaneous Contractility in Skeletal Myotubes	162
6.3	VTA MATLAB CODE.....	163
7	Bibliography	213
8	Curriculum Vitae	226

List of Illustrations

Figure 2.1-1. Information density in neural interfaces	3
Figure 2.1-2. Invasive PNS interfaces schematized by selectivity and invasiveness (Reproduced from [37])	5
Figure 2.1-3. Postoperative anatomy for two patients receiving TMR.....	7
Figure 3.1-1. VTA program processing path	16
Figure 3.1-2. Representative videomicrograph and accompanying VTA analysis	17
Figure 3.1-3. Success vector, failure vector, and net success score	22
Table 3.1-1. Description of synthetic and <i>in vitro</i> data sets.....	24
Figure 3.1-4. Program performance	27
Figure 3.1-5. Frequency and sources of misclassification errors	29
Figure 3.2-1. Schematic of several classic morphological analysis tools.....	37
Figure 3.2-2. Schematic of the digitization and analysis process available through the Bonfire program	40
Figure 3.2-3. Two structure-dependent labeling schemes that assign an identity to neurite segments based on their location within their arbors	43
Figure 3.2-4. Results of Bonfire analysis for hippocampal neurons treated with 25 ng/ml BDNF and untreated control neurons	45
Figure 3.3-1. Recording and interpretation of EVTs using and MEA	54
Figure 3.3-2. Schematic of spike-sorting algorithm.....	59

Figure 3.3-3. Spike-sorting by principal component analysis (PCA)	63
Figure 4.1-1. Characterization of PDMS Substrate	70
Figure 4.1-2. Myotube morphology on chemically and topographically patterned substrates.....	74
Figure 4.1-3. Myoblast alignment with major trench axis in DIV 0 – DIV 8	76
Figure 4.1-4. The number of independently active cells per unit surface area in grooved and smooth myotube cultures as a function of culture age	78
Figure 4.1-5. VTA-Identified regions of contractility on grooved PDMS substrates with 100 μm – 400 μm trench geometries and unpatterned control	79
Figure 4.1-6. Myotube contractility spatial relationship with trenches	81
Figure 4.2-1. EAP Spatial distribution in dissociated cortical culture vs. spinal cord explant culture.....	93
Figure 4.2-2. SC Explant Morphology and Outgrowth.....	95
Figure 4.2-3. Topographical and chemical guidance of explant outgrowth	96
Figure 5.1-1. Characteristic myotube-electrode and neuronal-electrode interactions..	105
Figure 5.1-2. Synchronous multi-electrode activation in myotube cultures and neuronal cultures.....	108
Figure 5.1-3. Stimulation of myotube networks using a substrate-embedded MEA.....	110
Figure 5.2-1. myo-MEA schematic.....	115
Figure 5.2-2. Schematic of microfabrication process	116
Figure 5.2-3. Myo-MEA prototype	119

Figure 5.2-4. Myotube differentiation and guidance on myo-MEA topographical features	121
Figure 5.2-5. Myo-MEA recordings of myotube EAPs.....	121
Figure 5.2-6. Patterns of myotube activation on topographically patterned vs. uninsulated myo-MEAs	123
Figure 6.1-1. Conceptual coculture possible using myo-MEA design	128
Figure 6.1-2. Explant integration with the myo-MEA.....	130
Figure 6.1-3. Myo-MEA coculture schematics demonstrating potential patterns of synaptic connectivity	132
Supplemental Figure 1 Spontaneous contractile activity in myotubes before and during treatment with tetrodotoxin (TTX) at 500 nM. N = 12	162

1 Introduction: a review of current technology in neural interfaces and the health relevance of the myo-MEA

1.1 Current state of neural interface technology

1.1.1 Abstract:

Neural prosthetics are “artificial extensions to the body that restore or supplement functions of the nervous system lost during disease or injury [14].” Typically, a neuroprosthetics device consists of some sensor or actuator that interacts with the environment and a “neural interface” responsible for communicating with the nervous system. The neural interface is the point at which the machine exchanges information with the nervous system (reviewed recently in the popular press [15]). In the case of sensory prostheses, such as a cochlear implant [16, 17], the neural interface is designed to insert signals into the nervous system by stimulating the nervous tissue, while in the case of motor prosthetics [18-20], such as those currently under development in many laboratories, the purpose is to extract signals from the nervous system by recording the activity of the nervous tissue. Long-term efforts are aimed at creating hybrid systems capable of two-way communication with the nervous system for restoring full function to amputees as well as to other patient groups [21, 22]. The major hurdle to progress in the clinical advancement of neuroprosthetics devices is the development of neural interfaces capable of efficient communication with the nervous system [5].

1.1.2 Acquiring Neural Signals Related to Motor Intention:

The mechanical capabilities of currently available prosthetic devices have become sophisticated [5, 18]. However, motor tasks are driven by gross anatomic movements or low bandwidth myoelectric couplings, making them cumbersome [5, 13]. For such

prostheses, communication with the user is the weakest link in the chain of components that includes electronics, computing, actuators, mechanisms, and materials, all of which are adequate for the application [18]. Neuroprosthetic devices aim to correct this deficiency by placing the prosthetic actuator directly under neural control. One subtype of neuroprosthetic device, a neuromuscular prosthesis, captures neural signals involved in motor intention and redirects them for use in controlling an artificial device. Efforts to move such devices into clinical practice have been slowed by the lack of a neural interface capable of recording neural signals effectively enough to restore fine motor control or sensory function [5, 6, 23].

Current reviews of neural interface design highlight the following functional criteria as bottlenecks in the continued progress of this field [6, 23-25]: 1) obtaining stable, long-term recordings of large populations of neurons, 2) developing computationally efficient algorithms for translating neuronal activity into command signals capable of controlling a complex artificial actuator, and 3) determining how to use brain plasticity to incorporate prosthetics. While small populations of highly tuned neurons can accurately predict movement parameters, highly tuned neurons are rare in a random sample of cortical cells. Because motor information is represented in this highly distributed way, large samples of recorded cortical neurons are preferred [23, 26, 27]. It has been estimated that recordings from 500 to 700 cortical neurons would be needed to achieve 95% accuracy in predicting one-dimensional hand movements [28]. The minimum number of recordings required to transform thoughts into a reasonable range of motions most likely exceeds 1000 [18], a number presently exceeding the capabilities of cortical probes. As an analogy, imagine trying to read a computer screen with only a small number of pixels (Fig. 2.1-1). The more complex the message, the larger the number of pixels required to read it. As a research community, we should pursue diverse approaches to both

simplifying the message and improving our ability to read it. This will require the development of diverse methods to record and decode motor intention as well as targeting multiple regions of the nervous system.

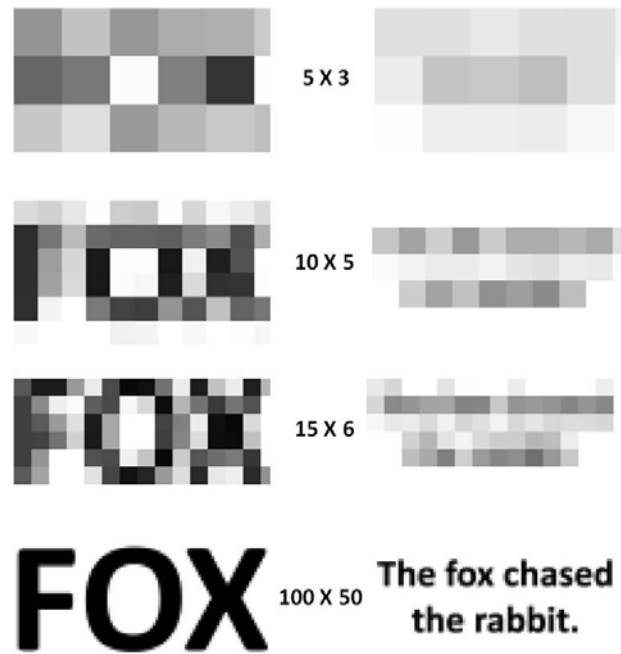


Figure 2.1-1. Information density in neural interfaces

More complex messages require a larger number of independent signals sources (in this case pixels) for proper decoding

The intention to perform an action is born in the cortex of the brain, is processed through multiple regions of the brain and spinal cord, comprising the central nervous system (CNS), and is transmitted along the axons of the PNS, finally arriving at the neuromuscular junction (NMJ) where it triggers the depolarization and contraction of the specific muscle cells required to perform the desired action. There is continual debate on where in this chain of transmission is the best location from which to derive a useful motor signal, and therefore, to target with a neural interface [6, 12, 23, 29-31].

1.1.3 CNS Interfaces:

Historically, many have designed neural interfaces with the intention of communicating directly with cortical tissue [9]. Most of these efforts use penetrating MEAs to record depolarization of cell bodies [3, 5, 12, 23]. With these designs, electrodes located at the end of micron-scale spikes are inserted directly into central nervous system (CNS) tissue. While there are a number of benefits to this approach (most notably that it is technically simple to record a neural signal from a region where the large neuronal cell bodies may be accessed), progress is confounded by the complicated encoding of information in cortical brain regions [32] and by the highly invasive nature of implanting any foreign device in the CNS [33, 34]. Complicating issues for these electrodes include poor long-term recording due to fibrous encapsulation, inflammation, death of surrounding neurons, and insufficient data transfer and decoding ability to interpret signals recorded at the cortical implantation site [9, 35, 36]. These devices have yet to perform at the level necessary to justify their use in large-scale clinical trials [6] but are in use in a limited number of clinical trials with a small number of patients [10].

1.1.4 PNS Interfaces:

As an alternative to targeting the CNS, other groups have developed means of targeting the PNS [3]. An MEA-based neural interface that targets the PNS improves on current technology by taking advantage of the specific nature of the PNS in managing motor control. Each conscious action originates with upper motor neurons in the motor cortex that trigger a neural network distributed across brainstem nuclei, cerebellum, and spinal cord. This neural network synthesizes input from thousands of tactile, positional, and visual sources with motor intention from the primary motor cortex to derive controlled motor output [18]. Recording neural activity in the PNS after it has passed

through the many processing steps occurring in the spinal cord, brainstem, and cerebellum may result in increased information content in the resulting signal. A clinically relevant example of this phenomenon is cochlear implants, which restore hearing by directly stimulating the nerve cells in the cochlea. Attempts to stimulate more central areas of the auditory pathway have been less successful. Experts suspect this failure is secondary to the loss of important signal processing in the periphery [25]. Due to its comparative physical accessibility, the discrete encoding of motor and sensory signals, the regenerative capacity of peripheral axons [4, 26, 37], and the reasons discussed above, the PNS may represent a more convenient location for accessing neural signals.

Neural interfaces that target the PNS pose a good compromise between the benefits and drawbacks of many types of neural interfaces [29, 30]. However, even in the PNS, interfaces with good specificity (i.e., the ability to record the activity of specific neurons) pay the price of being more invasive (Fig. 2.1-2). Consequently, there are multiple PNS interface designs (reviewed in [12]).

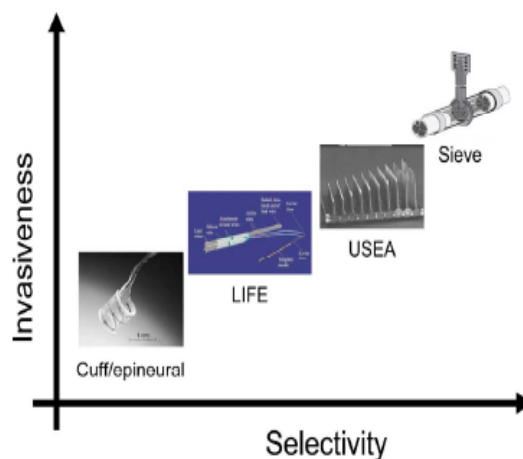


Figure 2.1-2. Invasive PNS interfaces schematized by selectivity and invasiveness
(Reproduced from [38])

Extraneural electrodes, such as the cuff or epineural designs (relatively noninvasive and unspecific), attach to the outside of peripheral nerves. The most popular current examples are cuff electrodes [39], which attach to the outside of nerve bundles and record the activity of the fascicles (large, related axon clusters) with the nerve, but are only capable of recording a small amount of information [40].

Intraneural electrodes (more invasive but more specific) are inserted directly inside of the peripheral nerve where the recording sites can make nearly direct contact with the axons transmitting information. Notable examples include longitudinal intrafascicular electrodes (LIFEs) [30], but also a number of other penetrating electrode designs have also been deployed in the PNS [41], though at this point these are primarily used for stimulation rather than recording purposes (such as the Utah staggered electrode array – USEA).

Regenerative electrodes, such as the sieve electrode (highly invasive and highly specific), are placed in the gap of peripheral nerves that have been fully transected and record from axons which regenerate through the electrode [42]. Problems with this type of interface are currently being addressed by the redesigning the recording sites to be tubular rather than planar [43-46]. These tubular recording sites are frequently fabricated by rolling arrays of parallel microchannels (microgrooves) with incorporated substrate-embedded MEAs into cylindrical constructs for implantation [47, 48].

1.1.5 EMG Surface Interfaces:

The most clinically successful means of establishing a control signal for powered prosthetic devices has been recording the electromyographic (EMG) activity of residual muscles [49, 50]. Traditionally, this has been accomplished using residual muscles that were related to the activity of the prosthesis prior to amputation or by using EMG activity recorded from other unrelated muscles that have been retrained for prosthetic control

[51]. More recently, a technique titled “targeted muscle reinnervation” (TMR) has been developed, in which the residual peripheral nerves left after an amputation are rerouted to muscles left useless by the loss of the limb (Fig. 2.1-3) [52]. These nerves regenerate onto the new musculature allowing the amputee to contract them by trying to perform actions with the missing limb, and providing a new EMG source from which more intuitive control over a powered prosthetic may be derived [53]. All currently available myoelectric technologies depend on EMG recordings made at the skin’s surface, and while muscle-implantable electrodes have been shown to be stable for long periods of time, such devices are almost exclusively used for functional electrical stimulation (FES) rather than EMG recording (with the notable exception of devices intended for diagnostic purposes) [12].

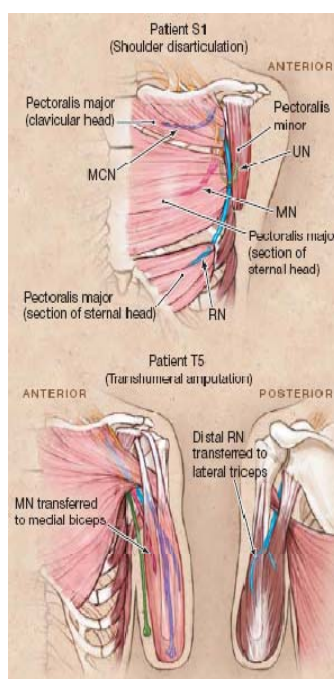


Figure 2.1-3. Postoperative anatomy for two patients receiving TMR

This illustration shows where the surviving peripheral nerves have been rerouted to residual muscled for reinnervation (reproduced from [53])

1.2 The myotube-integrated MEA (myo-MEA) as a next step

The proposed neural interface employs a combination of electromyography, which takes advantage of the larger extracellular voltage changes caused by the depolarizations of muscle cells relative to those of neurons [54-56], and a cultured-probe technique, which takes advantage of the high degree of specificity available to dissociated cultures grown on MEAs [13, 57, 58]. Such a device is necessary because recording from individual PNS axons is not feasible with traditional approaches. Recording from motor axons *in vitro* is not currently feasible because they are comparatively small and create extracellular voltage changes below the detection limit for traditional MEAs [9, 59]. Developing a myo-MEA may enable researchers to use myotubes as a biological signal amplifier to record neural signals carried in spinal motoneuron axons. The myotube amplifies the signal traveling down the motoneuron axon by virtue of coupling through the neuromuscular junction (NMJ) in much the same way a loud speaker amplifies the voice of someone speaking into a microphone.

Based on the relative success of EMG-based and PNS-based neural interfaces, the myo-MEA is a neural interface design meant to combine the benefits of the two approaches. In this thesis, we culture myotubes on an electrode array in a modification of the traditional cultured probe concept [11], specifically employing microscale grooves to accomplish two goals: 1) direct the formation of myotubes to specific electrode sites, and 2) to preserve myotube independence from one another. This is important in terms of increasing the number of independent signals available per unit surface area and maximizing the capability of such a device to record neural signals. Additionally, the topographical modification serves to stabilize the myotube culture, which can be

mechanically disrupted by the contractions of the myotubes themselves over extended periods of time.

There are three primary ways targeting the PNS by using myotubes as signal receiver/amplifiers will improve on current neural interface designs: 1) the current understanding of cell-electrode contact suggests that the increased physical size and transmembrane current of myotubes will improve electrode sealing [60-62], 2) the bi-directional communication between myotubes and motoneurons may promote growth of axon collaterals from the native PNS into the cultured probe [26, 37], and 3) current knowledge about neural information processing suggests that targeting the PNS for neural interface implantation will simplify the algorithms involved in decoding motor intention [3, 5]. The myo-MEA design stands to increase R_{seal} between the cell and electrode, specifically targets neural signals that are highly tuned to motor intention, and targets a portion of the nervous system where motor intention has already undergone cerebellar processing.

2 Developing and characterizing novel tools for quantifying muscle cell and neuronal behaviors

2.1 Identification and quantification of skeletal myotube contraction and association *in vitro* by video microscopy

2.1.1 Abstract:

Ex vivo cell-based experimental systems used to study muscle cell contraction, and others based on incorporation of cells into sensitive force transducers or electrophysiology equipment, are time-consuming, invasive, and not universally available, slowing the pace of research. Video microscopy provides a noninvasive way to record the contractile behavior of skeletal muscle cells *in vitro*. We have developed a numerical procedure, using image processing and pattern recognition algorithms, that makes it possible to quantify contractile behavior of multiple myotubes simultaneously, based on video data. We examined the ability of the program to identify movement using a simplified graphical model of myotube contraction and found that the program's success is dependent on the morphology and movement characteristics of the objects. However, the program performs optimally over the types of motions approximating those observed in culture and identifies contracting myotubes in sample videomicrographs of muscle cells *in vitro*. This program quantifies contractility on a population level, can be adapted for use in laboratories capable of digital video capture from a microscope, and may be coupled with other experimental techniques to supplement existing research tools.

2.1.2 Introduction:

Skeletal muscle is the largest tissue in the body by weight and plays many roles in maintaining homeostasis and health. Muscle tissue engineering has been recognized as important for the replacement of both cardiac [63] and skeletal [64] muscle cells, as actuators in biointerfacing robotic applications [65], as protein delivery vehicles in gene replacement therapies [66], and as biological sensors in lab-on-a-chip applications [67-69]. Experimental systems used to study muscle cell contraction are time-consuming, invasive, and not universally available, thus slowing the pace of research [65, 70-72]. Traditionally, tools for examining muscle cell function fall into several categories: biochemical, morphological, and kinetic.

Biochemical studies focus on the molecular composition of muscle, measuring the quantities of myosin or actin subtypes or other proteins relevant to the intracellular contractile machinery [64, 73, 74], and can reveal shifts from fetal to mature phenotypes. Such studies are limited in their ability to directly show the involvement of specific proteins in generating excitation or contraction and in demonstrating a change in functionality associated with the changing levels of these proteins. As a result, biochemical techniques are frequently used in conjunction with other methods.

Morphological studies consist of static examinations of cell shape, size, and appearance [56, 63, 73-76]. Looking at the organization of cellular structures unique to myotubes, such as the sarcomere or neuromuscular junction, is an important means of identifying stages in muscle cell development. However, by only examining the way the cells look and not how they act, these methods miss the dynamic aspects of myotube behavior.

Kinetic studies are meant to quantify muscle cell excitation and contraction by one of several methods. Contractile force can be measured by integrating muscle preparations

with macroscopic [63, 64, 77] or microscopic [72] force transducers. Force generation is a very direct endpoint for quantifying myotube function, but such studies depend on the use of dissected tissues or trypsin-digested cells and their time-consuming manual integration with force transducers. Muscle cell kinetics can also be studied using traditional electrophysiology [56] or can be visualized by imaging Ca^{2+} sparks or voltage changes within myotubes [73, 78, 79] using dyes with voltage- or Ca^{2+} -dependent fluorescence. Voltage- or Ca^{2+} -based techniques provide information about the intracellular handling of Ca^{2+} or depolarization events on a very short timescale with high resolution. However, some dyes have been shown to have an effect on Ca^{2+} handling and cell health when used over long periods [80].

Finally, muscle cell kinetics can be studied using video recordings based on transmitted light. Most frequently, optical data are acquired through careful placement of photodiodes used for spot or edge detection of cell boundaries or through the application of digitized spot detector algorithms to full digital recordings [71]. Current optical techniques are highly sensitive to cell geometry, specimen focus, and detection methods [71]. As a result, they are overwhelmingly geared toward application to single cells and still require complicated cell preparations. Finally, the need for clear visual fields, precisely shaped and positioned single-cell targets, and the necessity for bulky optical equipment means that these techniques cannot be used simultaneously with many of the biochemical, morphological, or kinetic techniques mentioned previously [71].

One of the problems facing all of the kinetic studies mentioned above is the variability among muscle cells. Cardiac and skeletal muscle cell differentiation and development *in vitro* varies greatly between preparations [71] or even across the same culture [68]. Only a partial understanding of muscle cell kinetics can be inferred from limited observations of events since the activities and morphologies observed in different viewing fields may

be very different. Because myotube behavior can be so complex, there is no single comprehensive method to examine myotube contractility. It is therefore crucial to use combinations of techniques and to generate supplemental new techniques to provide novel insight into myotube excitation/contraction [68, 71, 81].

We have developed a video-based research tool to facilitate population-level studies of developing myotube functionality, termed the Visual Twitch Analysis (VTA) algorithm, which can be easily combined with other existing research tools. The full text of the MATLAB code for the VTA algorithm is available in the appendices of this thesis. Video microscopy provides a noninvasive way to record the contractile behavior of skeletal muscle cells *in vitro* [56, 71, 76, 82-87]. Visual analysis of such data by hand, however, is confounded by the small and sporadic nature of spontaneous muscle cell contractions *in vitro*, by the difficulty of assigning some form of graded quantification to these events, and by the unavoidable introduction of bias, either through visual identification of contraction events or through hand selection of specific regions that are then passed to an automated analysis tool [71]. Having a fully automated system to perform video analysis makes it possible to quantify large amounts of data in an unbiased way and with a high degree of reproducibility and flexibility.

2.1.3 Materials & Methods:

2.1.3.1 Cell Culture

Myoblasts were isolated, cultured, and imaged as previously described in the literature [54, 88, 89]. Briefly, pregnant Sprague Dawley rats were sacrificed by CO₂ inhalation at gestational day 21, in accordance with Rutgers University animal care procedures. Pups were removed by Cesarean section, and hind limb muscles were removed to a separate container of Hanks' Balanced Salt Solution (Invitrogen, Carlsbad, CA) + 1% HEPES Buffer (Mediatech, Inc., Herndon, VA). Tissue was finely minced and

brought to a final volume of 7 ml in PBS containing 1.5 U/ml collagenase (type D, Roche, Mannheim, Germany) and 2.5 U/ml dispase (type II, Roche, Mannheim, Germany). Tissue slurry was then incubated for 20 min at 37° C and triturated using a pipette to break up remaining tissue clumps. Solid debris were allowed to settle for 15 minutes, and remaining cells were pelleted out of the supernatant by centrifugation. The cell pellet was resuspended in growth medium consisting of Ham's F-10 medium including 20% fetal bovine serum, 1% Penicillin/Streptomycin, (all from Invitrogen, Carlsbad, CA) and 2.5 ng/ml human b-FGF (Promega Corporation, Madison, WI). Cells were then plated into 75 cm² flasks and incubated for 24 hrs to allow for attachment of viable cells. Cultures were washed 3X with PBS to remove non-adherent cells and debris. Cells were then resuspended and plated onto smooth or grooved PDMS surfaces at a density of 150,000 cells/cm² in differentiation medium consisting of Neurobasal medium including 2% B27 Supplement, 1% Penicillin/Streptomycin, and 1% GlutaMAX (all from Invitrogen, Carlsbad, CA). Prior to seeding, surfaces were coated with laminin (Sigma Aldrich, St. Louis, MO) at 40 µg/ml.

2.1.3.2 *In Vitro* Video Capture & Synthetic Data Generation

Videos were acquired at day *in vitro* (DIV) 7 – 14, using an inverted microscope (Olympus, Center Valley, PA) with a SensiCam digital camera (PCO Imaging, Kelheim, Germany) and Image-Pro Plus image acquisition software (MediaCybernetics, Bethesda, MD). Thirty second videos of myotube behavior were acquired over 200 frames using a 10× objective and 512 × 640 pixel resolution, recording an area of 0.55 mm². To create the standardized set of videos used for subsequent program validation, example videos were hand sorted into groups containing 0, 1, 2, 3, 4, or 5 contractile cells. The number of videos in each group are as follows; N₀₋₃ = 5, N₄ = 3, N₅ = 2.

Synthetic data were generated to correlate with the *in vitro* video data above. Bars were created by randomly generating the coordinates for two points in a viewing field of 512×640 pixels. These points were connected with a black line of varying width. The amplitude of bar movement was determined by randomly generating a horizontal and vertical deviation for each of the bar endpoints from a predetermined range. The frequency of oscillations was selected from a range of 0.0 to 13.3 Hz (or 0 to 400 times over the course of the movie). Movies were simulated for 200 frames, with a timing of 0.15 sec/frame, which was the maximum acquisition rate for our software/camera combination (see Discussion for a description of how acquisition frame rate may affect further analysis of video data). Bar width and endpoint deviation were drawn from a distribution yielding the final behaviors indicated in Table 1.

2.1.3.3 Automated Data Analysis

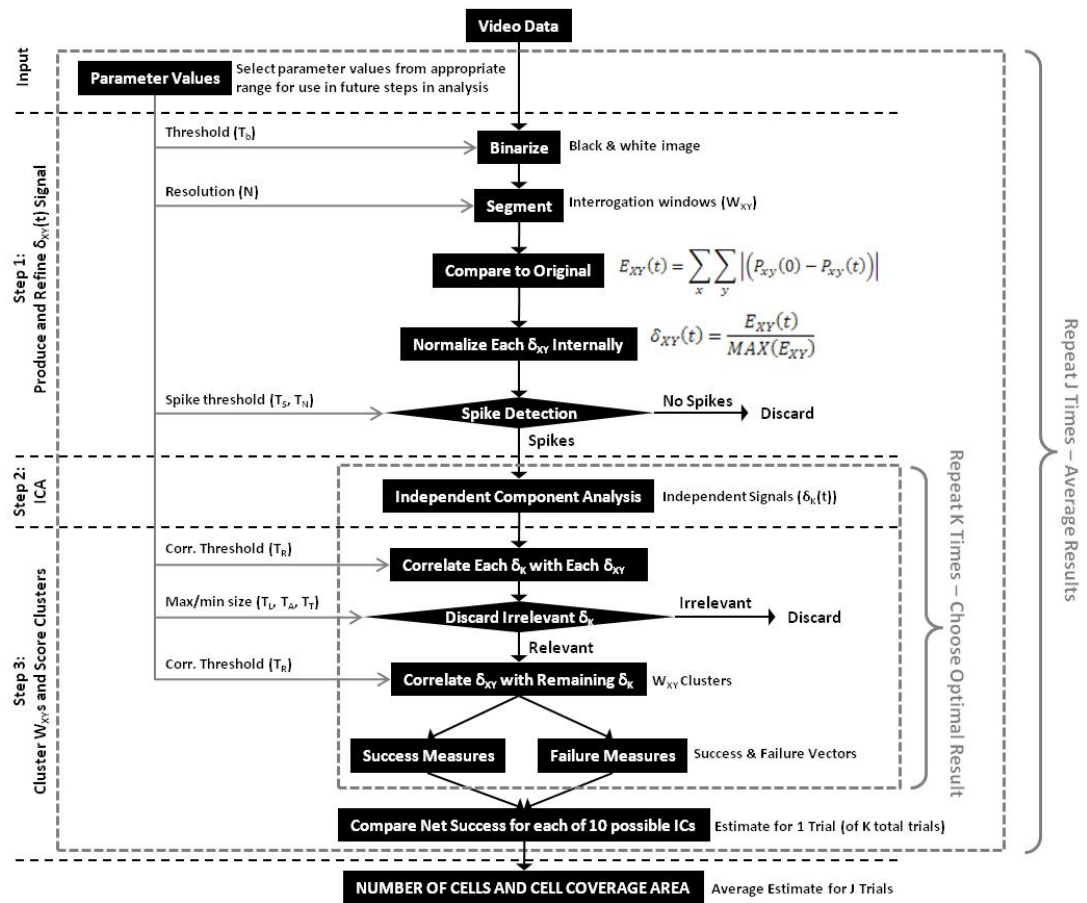


Figure 3.1-1. VTA program processing path

Blocks indicate individual processing steps (rectangles) or decision points at which irrelevant data can be discarded (diamonds). Arrows indicate the inputs of experiment-derived data (black arrows) or external parameters (gray arrows) to each processing sub-step to the next. The algorithm is conceptually broken into three fundamental steps (black dashed lines) discussed in the text. Portions are run iteratively (gray dashed boxes) to improve accuracy.

The VTA program involves an automated three part process, shown in Fig. 3.1-1: 1) image processing and data extraction, 2) generating sets of possible myotube conformations that explain the data, and 3) selecting the best set of myotube conformations. In the first step, the VTA program breaks each frame of the video into

multiple regions and compares it to the initial frame. This generates a measure of how local pixel intensity changes as a function of time. These changes can be caused by myotube contractions or by culture artifacts, such as changes in lighting and floating debris. In the second step, these time-variant functions are used to identify contractile regions of the video. In the third step, these regions are judged for “fitness” in explaining the data. Because the process is partially dependent on several parameters used in the image processing and fitness testing steps, this process is repeated several times and averaged to yield the final estimate of the number and location of cells (see Discussion section for description of how parameter values affect program performance).

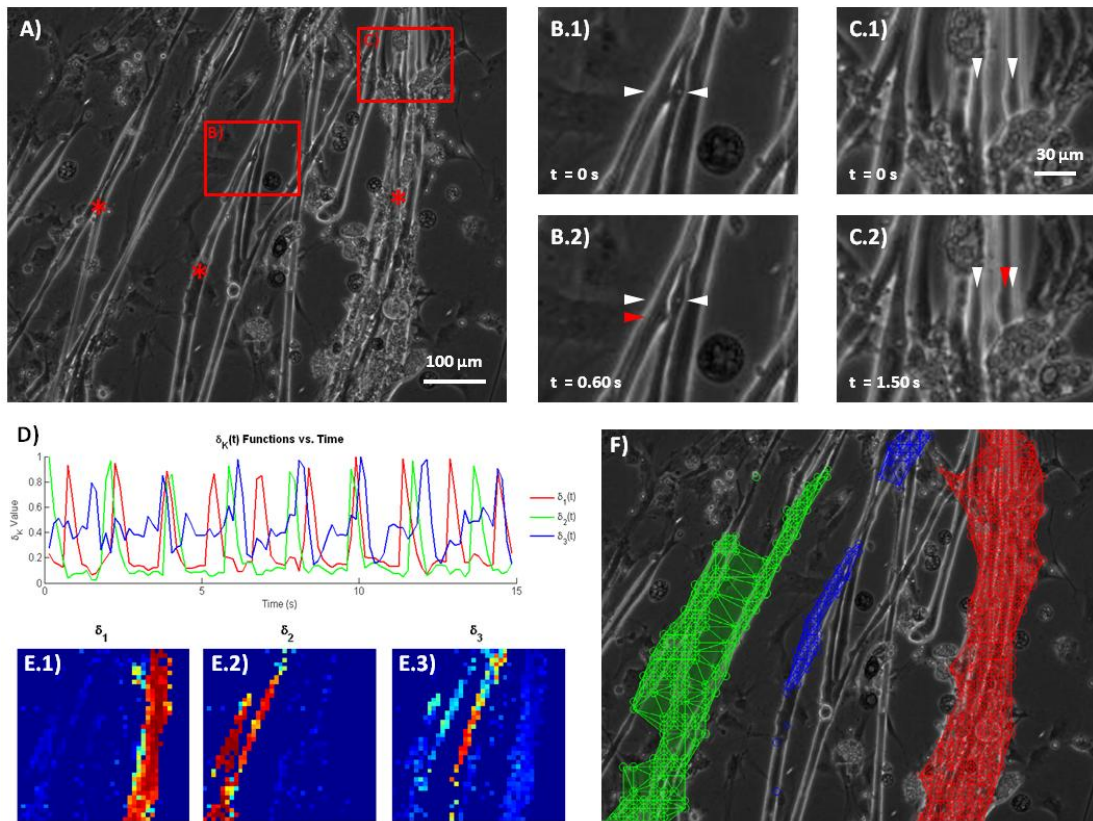


Figure 3.1-2. Representative videomicrograph and accompanying VTA analysis

(A) Full image of the viewing field; in this case containing multiple independently active myotubes, at $t = 0\text{ s}$ (*red stars*). Selected areas (*red boxes*) are magnified and shown at separate time points in B and C, respectively. (B)

and (C) Magnified image of the area boxed and labeled in A. *B.1* and *C.1* show these regions at $t = 0$ s; noteworthy features (*white arrowheads*) are noted for comparison with later time points. Myotube movement is apparent from the displacement of these features in *B.2* and *C.2* from their initial positions (again indicated by *white arrowheads*) to their position at maximum deflection some time later (*red arrowheads*). (D) Example output from the VTA program, demarcating the areas covered by the 3 active cells (*color-coded hatchwork*). (E) The $\delta_K(t)$ function for each of the 3 cells plotted over time. Individual contractile events can be visualized as the peaks occurring semi-rythmically throughout. (F) The correlation of each $\delta_{XY}(t)$ function with the $\delta_K(t)$ functions shown in E. Activity is clearly correlated in regions associated with particular cells.

In the first part, a series of image processing steps transform the video into a collection of time-variant functions representing the extent to which a given region in the image has deviated from its initial position over the course of the movie. The first step is to threshold each frame of the video to turn it into a black and white image. Pixels with a value above the binarization threshold (T_B) are assigned a value of 1 while all others are 0. Next, each image is divided into an $N \times N$ grid. Each block of the grid is treated as its own interrogation window (W_{XY}), where the capital subscripts X and Y refer to the block's location in the $N \times N$ grid. For each W_{XY} , the quantity of binarized pixels (P_{xy}), which switch values (i.e., from $1 \rightarrow 0$ or from $0 \rightarrow 1$) as compared to first frame in the video ($t = 0$), are summed over x and y , where the subscripts lower-case x and y indicate the position of each pixel within its interrogation window (W_{XY}) (Fig. 3.1-2, *B-C*). This is repeated for each subsequent frame ($t = 1, 2, \dots, n$), generating a time-variant indicator of deviation from the starting point for each W_{XY} (referred to as $E_{XY}(t)$). This is repeated for all W_{XY} , according to Eq. 1:

$$E_{XY}(t) = \sum_x \sum_y \left| \left(P_{xy}(0) - P_{xy}(t) \right) \right| \quad (1)$$

Significant change from the initial position in a particular E_{XY} may indicate contractile activity in the corresponding window. W_{XY} windows that contain $E_{XY}(t)$ peak values above

the product of the “spike threshold” value (T_S) and the standard deviation of the $E_{XY}(t)$ function are assumed to include contractile information, while those without peaks over this level are excluded from further analyses. Inclusion criteria for further analysis are expressed in Eq. 2:

$$MAX(E_{XY}) \geq T_S \times STD(E_{XY}) \quad (2)$$

Videos containing fewer than a threshold number (T_N) of windows demonstrating contractility are classified as containing no contractile cells. Finally, the remaining $E_{XY}(t)$ functions are each normalized to themselves, to yield the “delta function” ($\delta_{XY}(t)$). The $\delta_{XY}(t)$ functions are therefore essentially a unitless measure of displacement as a function of time, which allows the rest of the algorithm to identify portions of the images that move synchronously. $\delta_{XY}(t)$ is calculated according to Eq. 3:

$$\delta_{XY}(t) = \frac{E_{XY}(t)}{MAX(E_{XY})} \quad (3)$$

In the second stage, the Jade algorithm [90] is used to perform independent component analysis (ICA) on the $\delta_{XY}(t)$ functions. ICA is a computational technique used to recover original independent data streams when the data are sampled on multiple recording devices, each of which records a different linear mixture of the original data. An example is recording two people speaking at a cocktail party from microphones placed at four arbitrary locations around the room (the “cocktail party problem”). ICA is ideally suited to regenerate the original sound information of each speaker based on the recordings from the four microphones, each of which records a different mixture of both speakers based on its location relative to the two signal sources [91]. In its most basic form, the ICA algorithm must be instructed of the number of original signal sources it is

meant to identify. Further explanation of the algorithms used to perform ICA has been discussed extensively by other groups [91-94].

Performing ICA on the $\delta_{XY}(t)$ functions returns new time-variant functions in the form of K separated data streams (termed $\delta_K(t)$), where K is the number of signals the ICA algorithm was instructed to extract. These $\delta_K(t)$ functions represent the presumed activity of the contractile myotubes, which have been recorded in a mixed fashion in the $\delta_{XY}(t)$ functions (Fig. 3.1-2, *D*). The $\delta_{XY}(t)$ functions act like an array of N^2 microphones, recording contractile activity from K independent myotubes, which are like the cocktail party guests in the example above. This is performed iteratively for $K = 1, 2, \dots, K$, generating K possible prospective myotube sets. After each iteration, the results are analyzed in the third stage of our algorithm, and judged for overall fitness.

The third stage is concerned with determining which of the myotube sets generated in the second stage most closely resemble the natural behavior of myotubes while explaining the observed data. The first step in this process is to exclude $\delta_K(t)$ functions that are obviously not generated by myotubes. This is accomplished by grouping W_{XY} windows into clusters based on the correlation coefficient of their respective $\delta_{XY}(t)$ functions with each $\delta_K(t)$ function (Fig. 3.1-2, *E1-3*). Any window (W_{XY}) is included in cluster K according to the inclusion criteria in Eq. 4:

$$\text{corrcoef}(\delta_K(t), \delta_{XY}(t)) \geq T_R \quad (4)$$

where T_R is the correlation threshold. At this point, the center of W_{XY} becomes a “node” for the purposes of identifying myotube location. All nodes within a cluster are then joined according to the Delaunay triangulation [95]. Edges over a certain length (T_L) are then eliminated, leaving an arbitrarily shaped graph denoting the location of a likely contractile body (Fig. 3.1-2, *F*). The area of the resulting compound polygon is taken to

be the estimated area of that prospective myotube (A_i). This process allows us to generate a two-dimensional map of each prospective myotube in a set based on correlation of each $\delta_{XY}(t)$ function with the set of $\delta_K(t)$ functions.

Clusters are then screened for validity based on morphological characteristics, and clusters that are unlikely to be real myotubes are eliminated. For example, clusters covering more than a threshold percentage (T_A) of the viewing area are more likely to be lighting artifacts than they are to be myotube contractions. Similarly, clusters composed of a smaller number of triangular sections than a threshold number (T_T) are more likely to be floating debris than contracting myotubes. If a cluster does not pass both of these criteria, the corresponding $\delta_K(t)$ function is excluded from further analyses. While excluded $\delta_K(t)$ functions are not counted in further analysis, their initial inclusion is important because it provides the program with the opportunity to identify artifacts in the video and isolate their effect from the relevant data.

The remaining W_{XY} clusters are then used to measure the overall fitness for a given set of $\delta_K(t)$ functions. These measurements take the form of “success” and “failure” metrics, calculated from the geometry of the nodes in each cluster and the behavior of the $\delta_{XY}(t)$ functions, meant to identify how well the W_{XY} cluster explains the video data all within the context of looking for contractile myotubes. There are three success metrics, “Success Spread” (S_1), “Area Coverage” (S_2), and “Cell Number” (S_3), as well as three failure metrics, “Correlation Difference” (F_1), “Scatter” (F_2), and “Missed Twitch” (F_3) (see the appendix of this thesis an expanded explanation of how success and failure metrics are calculated). Each of these success and failure metrics is normalized to itself, creating a range of values between 1 and 0 for each of the cluster sets. They are then used to create a vector within the unit cube representing the total success and total failure of the cluster set (Fig. 3.1-3, A-B). The magnitude of the failure vector is then

subtracted from the magnitude of the success vector to assign a final score to the cluster set called the “Net Success” score (S_N), according to Eq. 5 (Fig. 3.1-3 C):

$$S_N = (S_1^2 + S_2^2 + S_3^2)^{1/2} - (F_1^2 + F_2^2 + F_3^2)^{1/2} \quad (5)$$

The set with the greatest net success score is considered the winner, and the number and location of the W_{XY} clusters is taken to be the number and location of contractile cells in the video (Fig. 3.1-3, C, *blue bar*).

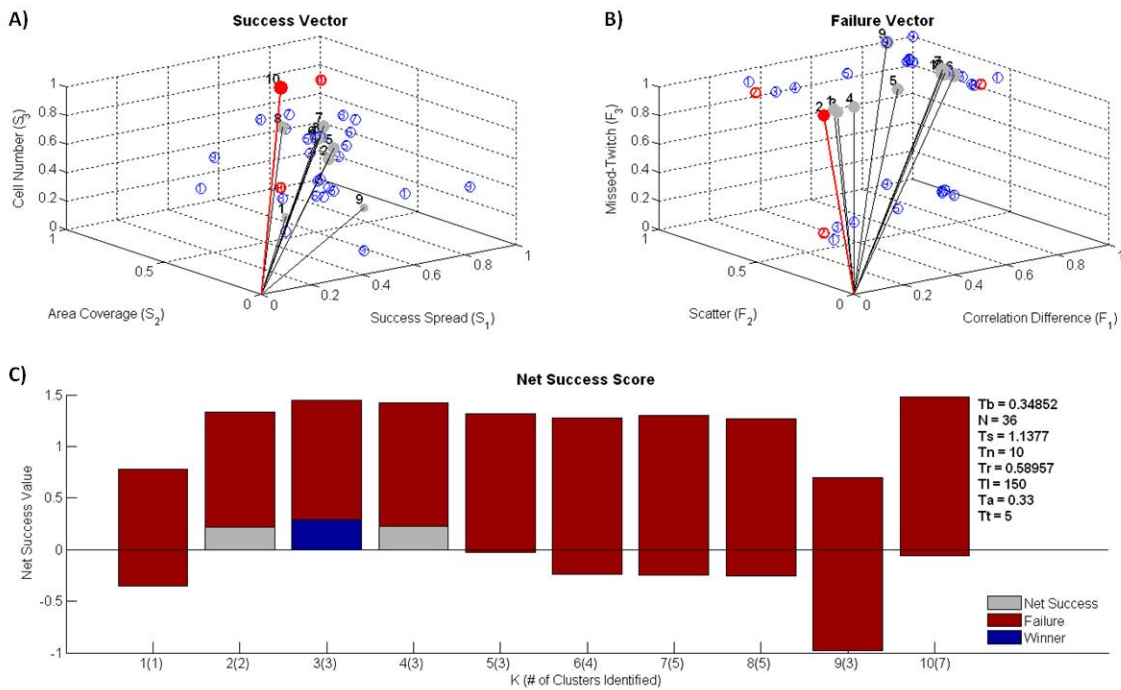


Figure 3.1-3. Success vector, failure vector, and net success score

Illustrative data from video pictured in Fig. 3.1-2 ($K = 10$). (A – B) The total success vector and failure vector, respectively, represented in their own unit cubes. Each cluster set receives a score on all three success metrics and all three failure metrics, defining a spot in “success space” and “failure space” (*gray circles sequentially labeled 1-10*). The distance from this point to the origin is the magnitude of the success and failure vectors (*black lines*). The highest success score and lowest failure score are indicated in the figure (*red lines*). The “shadow” of each point is projected on the 3 planes created by the 3 axes (*blue circles*). (C) The net success score shown for each cluster set examined. The height of the bar above the x-axis represents the length of the success vector. From this amount, the length of the failure vector is subtracted (*red bars*), leaving either residual positive net

successes (*gray bars*), or a negative net success score. The cluster set with the highest residual net success score is considered the “winner” (*blue bars*). Values for the parameters used in this analysis are indicated to the right.

Because several of the steps indicated involve external parameters, specifically all of the thresholding steps, the result of VTA analysis is sensitive to the values selected for these parameters (Fig. 3.1-1, *gray arrows*). For this reason, the analysis is performed several times for each video, and the parameters are drawn randomly from an appropriate range at the beginning of each trial (Fig. 3.1-1, *gray dashed boxes*). For additional information on the VTA algorithm (including MATLAB code and parameter values), see the appendix of this thesis.

2.1.3.4 Validation of VTA Program Performance on In Vitro and Synthetic Data

The VTA program was used to identify the number of contractile myotubes in the standardized *in vitro* video data set 1 in Table 1. The algorithm generated three cell number guesses for each video of each group. All the guesses generated for a given group were then averaged together to provide the VTA estimate of that group’s average number of cells per video. This estimate can be easily compared against the number of cells actually present in each video for that group as a means of gauging program performance.

Set:	# of Bars:	Task:	Behavioral Range:
1	0 – 5 (Cells)	Identify the average number of contractile myotubes in groups of videos hand-selected to contain 0, 1, 2, 3, 4, or 5 myotubes.	As observed <i>in vitro</i>
2	1 (200 videos)	Identify a single moving bar over a range of behaviors exceeding the	Frequency = 0.0 – 13.3 Hz
			Footprint = 0.0 – 0.30 mm ²

program's detection ability.			Oscillation Area = 0.0 – 0.23 mm ²
3	1 (200 videos)	Identify a single moving bar over a	Frequency = 0.0 – 1.0 Hz
		range of behaviors simulating	Footprint = 0.0 – 0.06 mm ²
		biological data.	Oscillation Area = 0.0 – 0.03 mm ²
4	0 – 10 (200 videos)	Identify multiple randomly placed,	Frequency = 0.0 – 1.0 Hz
		and potentially overlapping bars.	Footprint = 0.0 – 0.06 mm ²
			Oscillation Area = 0.0 – 0.03 mm ²
5	0 – 10 (200 videos)	Identify multiple randomly placed,	Frequency = 0.0 – 1.0 Hz
		and non-overlapping bars.	Footprint = 0.0 – 0.06 mm ²
			Oscillation Area = 0.0 – 0.03 mm ²

Table 3.1-1. Description of synthetic and *in vitro* data sets

In order to examine the performance envelope of the VTA program in situations atypical of those observed in our culture system, analysis of computer-generated data sets (synthetic data) was performed. Videos consisted of an oscillating black bar against a white field, meant to simulate the most basic movement of myocytes seen in video micrograph recordings. Bars of varying dimensions, orientations, and activity levels (frequency and amplitude) were simulated. Parameters determining the behaviors of the synthetic myotubes were randomly selected for each video from a pre-defined range. Five sets of videos were analyzed, as described in Table 1.

We use two metrics to measure VTA program performance: 1) number estimate error (N_E), and 2) area estimate error (A_E). The number estimate error is calculated as the difference between the number of bars identified by the program (N_I) and the true number of bars in the video (N_T), as in Eq. 6. Area estimate error is calculated as the difference between the contractile area identified by the VTA program (A_I) and the true area over which a bar moves during its oscillation (A_T), as in Eq. 7:

$$N_E = N_I - N_T \quad (6)$$

$$A_E = A_I - A_T \quad (7)$$

These error metrics are measured against features of the videos in the synthetic data sets, such as oscillation frequency, bar footprint, oscillation area, and number of bars present. The bar footprint is defined as the area covered by the stationary bar. Oscillation area is defined as the area through which the bar oscillates minus the bar footprint, allowing for the quantification of completely arbitrary bar movements. All synthetic data were generated and analyzed in MATLAB (The MathWorks, Natick, MA).

2.1.4 Results:

2.1.4.1 *Analysis of In Vitro Video Data*

Rather than creating additional synthetic data, which included artificially generated noise artifact as a means of testing the algorithm's robustness to biological and culture noise, the VTA algorithm was instead used to analyze a standardized set of videos, data set 1 in Table 1. Figure 3.1-4 A shows the average number of contractile cells per video identified for 6 groups of videos, containing 0, 1, 2, 3, 4, and 5 contractile cells, respectively. The VTA algorithm is sensitive enough that it identifies an average of 1.58 cells per video in the group where no contractile cells are present. In these cases, the algorithm incorrectly identifies lighting artifact and vibrational noise as contractile motion. This same inclusion error is repeated in each group, resulting in identified cell numbers of 2.60, 3.80, 4.27, 5.11, 5.83 for the other 5 groups (an average overestimation of 1.37 cells in each case). However, at this level of sensitivity, the algorithm is clearly able to provide an indication of the different activity levels in each group relative to other groups, differing by even a single contractile myotube.

2.1.4.2 Single Object Identification

The program's ability to identify a single bar was examined over two ranges of parameter values as described in Table 1 (data sets 2 and 3). Over the range of bar footprints, a noticeable decline in the area estimate error begins after 0.065 mm^2 , after which each step results in a noticeable worsening of the area estimate error (Fig. 3.1-4, B). Prior to this crossing point, the program overestimated the area by 0.01 mm^2 , while after the crossing point, it underestimates the area of coverage by an average of 0.08 mm^2 . Also noticeable is the program's failure to detect bars with a footprint below 0.0004 mm^2 , consistent with the VTA algorithm excluding signal sources below a minimum size.

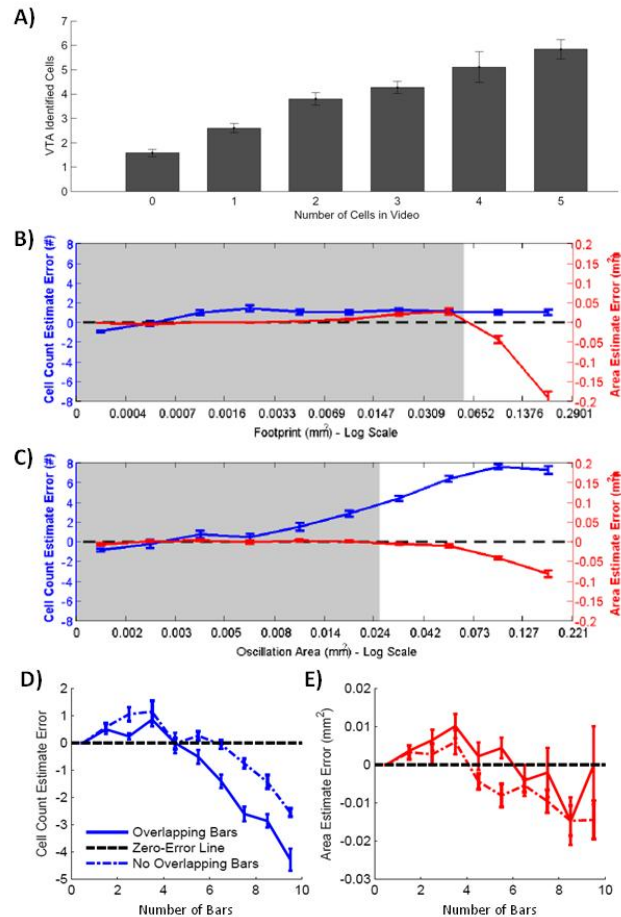


Figure 3.1-4. Program performance

(A) VTA performance on standardized *in vitro* data. Program performance at single bar identification vs. bar footprint (B), and oscillation area (C), respectively, examined over the range of behavioral characteristics described in Table 1. The Number Estimate Error is displayed (*blue lines and left y-axis*), as well as the Area Estimate Error (*red lines and right y-axis*). For comparison, these graphs also show the range of behaviors observed in cell culture (*shaded area*). (D) The Number Estimate Error as a function of bar number. (E) The Area Estimate Error as a function of bar number. Results at multiple object identification are shown for overlapping bar (*solid line*) and non-overlapping bar (*dashed line*) data sets as described in Table 1. Error bars represent the standard error of the mean.

Both the number estimate error and the area estimate error are sensitive to the oscillation area (Fig. 3.1-4, C). Similar to the trend observed with the increasing footprint size, there is a marked falling off in the accuracy of the area prediction past 0.07 mm^2 . Prior to 0.07 mm^2 , the program performs well, underestimating the area by only 0.004 mm^2 , while after that point, this number increases to 0.05 mm^2 . The number error is even more sensitive to the oscillation area, beginning a steep increase in the number estimate error at 0.01 mm^2 . Between 0.01 mm^2 and 0.08 mm^2 , there is a marked increase in the number estimate error with each step before this error metric plateaus.

Despite sensitivity of some performance measures to the extreme value of footprint and oscillation area, the program performs consistently at the single bar identification task over the range of behaviors meant to mimic culture behaviors *in vitro*, discussed in data set 3 in Table 1 (Fig. 3.1-4, A-C, *gray shading*). In analysis of synthetic data set 3 (data not shown), the VTA program overestimated the number of bars present by only 0.62. Over this same range of parameter values, the program performs similarly well at the area-identification task, overestimating the area by an average of 0.007 mm^2 .

2.1.4.3 Multiple Object Identification

Analysis was run on synthetic data sets 4 and 5, as described in Table 1. In both cases, the cell count estimate error stays low until some threshold is reached. When the overlapping bar data set is analyzed, the program can successfully classify videos containing up to 6 bars without overestimating or underestimating the number of bars by more than 1. When the non-overlapping data set is analyzed, by comparison, the program maintains a similar level of accuracy (overestimating or underestimating by less than 1) until more than 8 bars are present. However, program performance on both the overlapping and non-overlapping data sets drops off steeply past 6 and 8 bars, respectively, decreasing almost linearly with the number of bars past that point (Fig 3.1-4, *D*). In comparison, the area estimate error does not change past 6 bars with the exception that it starts to underestimate the contractile area. The magnitude of the area estimate error remains consistently low, however, even though the sign is reversed (Fig. 3.1-4, *E*).

2.1.4.4 Analysis of Example Video Micrographs

To expose the program to a wide range of behaviors, we performed analysis on several example videos taken under multiple culture conditions. Conditions included growth on a smooth substrate to encourage the formation of syncitial networks (Fig. 3.1-5, *A*) and on a grooved substrate to encourage the formation of independent and aligned myotubes (Fig. 3.1-5, *B*).

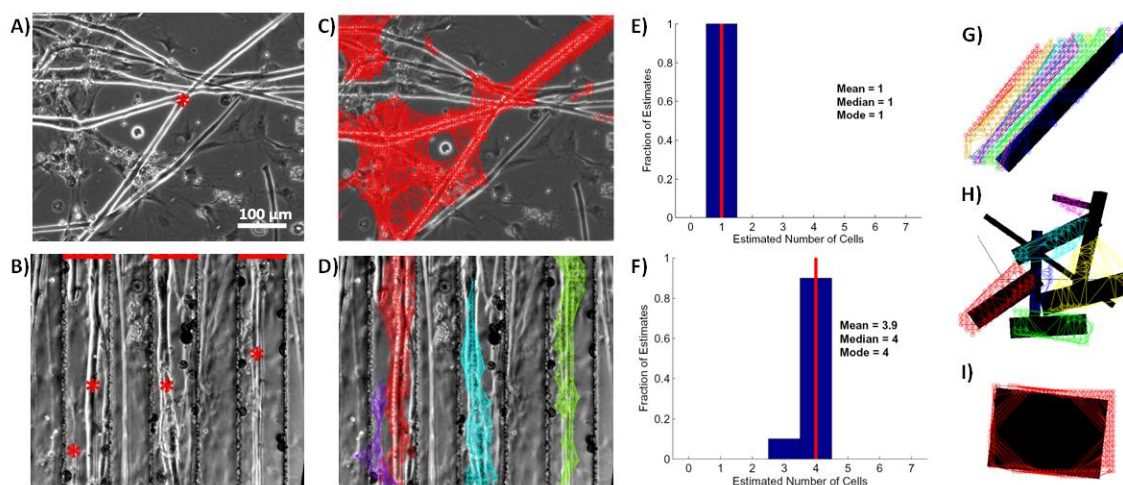


Figure 3.1-5. Frequency and sources of misclassification errors

(A) A syncytial network of contractile myotubes grown on a smooth surface (*single red star*). (B) Contractile myotubes (*red stars*) grown on surfaces modified with 100 µm grooves (*red bars*). (C – D) Locations of contractile cells identified by the VTA program from the videomicrographs shown in A and B, respectively. (E – F) Histograms of the VTA estimated number of cells in each video (*blue bars*), relative to the actual number of cells (*vertical red line*). The mean, median, and mode of the estimates are also shown in each case. (G) Single bar misclassification by identifying one or both of the edges as multiple bars. (H) Two mostly overlapping bars identified as the same object (*yellow hatch work*). (I) The omission of the center area of the bar resulting in underestimation of area coverage.

Inspection revealed that the network shown in Fig. 3.1-5 A was electrically coupled and contracted as a single network. The program was able to identify the network as a single contractile entity in 10 out of 10 trials (Fig. 3.1-5 E). Fig. 3.1-5 B shows myotubes cultured in 100 µm wide grooves which are 35 µm deep. Culturing the cells on the grooves resulted in the alignment of the myotubes and prevented myotubes in neighboring grooves from touching one another and forming networks. As a result, the myotubes contract independently of one another. Visual inspection revealed that this video contained 4 independent myotubes, one in each of two trenches and two located in the same trench (Fig. 3.1-5 B, *red stars*). These myotubes are successfully identified

and localized by the VTA program, which identified 4 cells in 9 out of 10 trials, with an average estimate of 3.9 cells (Fig. 3.1-5 F). Example videos for the above analysis may be found in the online supplementary material.

2.1.5 Conclusion:

2.1.5.1 *Selection of Processing Steps and Parameter Values*

Image processing for the automated analysis of biological data is a constantly evolving field. Selecting an appropriate method for specific projects usually means selecting from a grab bag of available algorithms and recombining them or tuning them to meet the needs of a particular application. There is no guide in this process other than experience, and more importantly, experimentation. The algorithm we have developed is meant to identify contractile myotubes in vitro. It consists of a series of image processing steps meant to generate trackable features, pattern recognition steps meant to extract the relevant patterns of behavior, and a cost-benefit analysis step meant to determine the overall fitness, all as a means of determining the number and location of the contractile myotubes. The result is a novel technique for quantifying functional population-level behaviors of myotubes and a generalizable blueprint for algorithm development in a wide range of other potential applications. While the optical analysis of myotube contractility has been performed previously [71, 83-86], the technique described in this paper expands on the utility of preexisting methods by fully automating the process of data extraction and increasing applicability in a wider variety of experimental situations.

As mentioned previously, the VTA algorithm is sensitive to the values for the parameters used in each of the processing steps. For example, the number of horizontal and vertical divisions the image is segmented into (N) affects the sensitivity and resolution of the subsequent analysis. Large N results in an image which is finely diced

into small W_{XY} windows, increasing spatial resolution. Because each W_{XY} is small, however, it contains a smaller number of pixels (P_{xy}), and the $E_{XY}(t)$ function (calculated as in Eq. 1) for that W_{XY} will contain a reduced signal to noise ratio (SNR). While this increases spatial resolution, it diminishes the ability of the program to use ICA to extract meaningful $\delta_k(t)$ functions. Alternatively, small N values result in large W_{XY} windows containing contractile information with a higher SNR, at the expense of spatial resolution. Similarly, there is a trade-off in the relative sensitivity vs. specificity of the algorithm, which can be tuned by altering the parameter values. If the algorithm is made more sensitive, by relaxing cluster exclusion thresholds for example, the algorithm can identify contractile cells in videos where there are none (Fig. 3.1-4 A). Alternatively, raising detection thresholds to increase specificity can result in the exclusion of contractile activity from smaller sources. Even in such cases, however, the program has the benefit of applying the same parameter set in the analysis of each video, and therefore maintaining consistency.

Ultimately, the optimal values for many of the parameters used in the VTA algorithm are related to the apparatus used to acquire the video data. Different set-ups may have very different optical qualities, including different levels of contrast, magnifications, frame acquisition rate, and pixel spatial resolution, which would change the appearance of myotubes within the video. All of these changes would therefore change the optimal thresholding values. The parameter values used in this study were tuned experimentally, using a procedure where VTA program output was compared to by-hand analysis for a small sub-set of randomly selected videos, and parameters were tuned to minimize the difference. Parameter values selected using this process were then applied in the analysis of all videos. Use of the VTA algorithm on other sets of data will likely require application-specific fine-tuning. Furthermore, while we use units on the scale of single

mm² and Hz because they are relevant to the size and activity levels of our subject in this study, skeletal myotubes, these units may be altered depending on the capabilities of individual recording equipment and subject. While the opportunity to improve program performance by automating parameter selection exists (see Future Directions below), the exercise exceeds the scope of this paper

2.1.5.2 Sources of Error and Error Reduction

Despite the selection of the most relevant and useful image processing, pattern recognition, and fitness-checking algorithms, the program still makes errors. In the single bar identification task, overestimation of the number of bars results from identifying one or both of the edges as multiple bars (Fig. 3.1-5 G). This is responsible for the chronic, low level overestimation of bar number occurring at all activity levels and is especially pronounced for bars with high oscillation areas. A second type of error, occurring during the multiple bar identification task, is when the VTA program assumes that two mostly overlapping bars are the same object (Fig. 3.1-5 H). For this to happen, the bars must move through approximately the same region, causing the program to identify only one pattern of behavior within that region. The cells need to be closely overlapping for this to happen, however, which is why this effect does not appear until there are >6 bars per image in the overlapping bar data set and >8 bars in the non-overlapping bar data set.

Additionally, there are two types of errors that cause the observed underestimation of area: 1) the omission of the center area of the bar (Fig. 3.1-5 I) and 2) the omission of alternating portions of the area through which the bar oscillates (Fig. 3.1-5 G). The first occurs because when the bar is large, the pixels in the central region never change values as the bar oscillates. Therefore, it appears to the VTA program as an inactive region. The second occurs because at large amplitudes, the multiple fronts do not add up to cover the whole area of oscillation.

In practice, myotube contraction is bound by connections with the substrate and extracellular matrix, causing feature behavior in videos of myotube contraction in vitro to fall well within the optimal performance envelope seen in Figure 3.1-4. The first type of error (identifying one front as multiple bars) is a result of large displacements of the bar during oscillation and is unlikely to occur when the myotube is partially substrate-adherent. However, contraction can also cause a deflection in the local extracellular matrix, causing the VTA algorithm to identify it as a portion of the myotube and generating an overestimate of the myotube area (Fig. 3.1-5C, webbing between myotube branches). The second type of error (identifying two bars as one bar) is a result of the close overlap between two or more bars. This is unlikely to happen in culture because the cells grow in a monolayer, making it difficult for two or more cells to occupy the same space in videos of contracting myotubes in vitro.

2.1.5.3 Implications and Future Directions

This program fills a gap in researchers' ability to monitor muscle cell function. The image processing steps successfully generate trackable features from video data, and the success and failure metrics are flexible enough to exclude extraneous information, such as changing lighting conditions or floating debris, while capturing a wide range of myotube morphologies and activities. It provides a way of looking at contractility on a population level, rather than in individual cells, and may be performed in most laboratories. Additionally, it is non-invasive and can be performed at multiple time points on the same culture or even on the same group of cells within a culture. The flexibility of this new analytical tool allows its use in a way that supplements the other biochemical, morphological, and kinetic techniques currently employed.

There are several areas of the VTA program, which may be improved through further development. The addition of a filtering step of the $\delta_{xy}(t)$ functions or the $\delta_k(t)$ functions

that occurs prior to the ICA or W_{XY} clustering steps may increase the efficacy of the program by removing high-frequency noise [91]. This may be especially interesting to pursue because it may also open the possibility of using $\delta_K(t)$ function-based approaches to generating additional success and failure metrics, which may improve program performance. Additionally, the VTA algorithm currently runs a user-determined number of times (J) and averages the estimates of the results. Many data processing algorithms include a feedback loop measuring some objective function of error and will alter parameter values iteratively in an effort to reduce the error measure below some threshold [78], and the incorporation of such an element into the VTA algorithm may improve performance accordingly. Finally, the weighting of each success and failure metric within the cost/benefit analysis affects program performance and may be optimized in a similar fashion to the other parameters. Currently each metric is weighted equally. However, a nonlinear combination of these same metrics may result in an improved fitness testing outcome. Such improvements, however, are beyond the scope of this paper.

Additional gains may be made by incorporating a controlled lab-on-a-chip device into the experimental design. The integration of substrate-based, microfabricated sensor arrays with the described optical technique could create new and sensitive dual-modality sensing arrays. For example, the application of the VTA algorithm to myotubes grown on an arrays of micropillars meant to accommodate and quantify cell contractility [96] would generate a sensitive mechanism to detect force generation in populations of myotubes. Another useful combination would be the application of the VTA algorithm to cells grown on, or immobilized on, microelectrode arrays (MEAs), which would provide a sensitive way to quantify the correlation between excitation and contraction in populations of single cells. Additionally, the use of the VTA algorithm in conjunction with MEA

technology would enable the incorporation of a contraction triggering mechanism, eliminating the dependence of many procedures on spontaneous activity.

2.2 Automated Sholl analysis of digitized neuronal morphology at multiple scales: Whole-cell Sholl analysis vs. Sholl analysis of arbor sub-regions

2.2.1 Abstract:

The morphology of dendrites and the axon determines how a neuron processes and transmits information. Neurite morphology is frequently analyzed by Sholl analysis or by counting the total number of neurites and branch tips. However, the time and resources required to perform such analysis by hand is prohibitive for the processing of large data sets and introduces problems with data auditing and reproducibility. Furthermore, analyses performed by hand or using course-grained morphometric data extraction tools can obscure subtle differences in data sets because they do not store the data in a form that facilitates the application of multiple analytical tools. To address these shortcomings, we have developed a program (titled “Bonfire”) to facilitate digitization of neurite morphology and subsequent Sholl analysis. Our program builds upon other available open-source morphological analysis tools by performing Sholl analysis on subregions of the neuritic arbor, enabling the detection of local level changes in dendrite and axon branching behavior. To validate this new tool, we applied Bonfire analysis to images of hippocampal neurons treated with 25 ng/ml Brain-Derived Neurotrophic Factor (BDNF) and untreated control neurons. Consistent with prior findings, conventional Sholl analysis revealed that global exposure to BDNF increases the number of neuritic intersections proximal to the soma. Bonfire analysis additionally uncovers that BDNF treatment affects both root processes and terminal processes with no effect on intermediate neurites. Taken together, our data suggest that global exposure of

hippocampal neurons to BDNF results in a reorganization of neuritic segments within their arbors, but not necessarily a change in their number or length. These findings were only made possible by the neurite-specific Sholl data returned by Bonfire analysis.

2.2.2 Introduction:

Neuronal morphology is important for determining how action potentials propagate, how information is processed [97-100], and neuronal function [101-104]. Neurite branching affects how single neurons integrate synaptic inputs [105, 106] and how they communicate as networks [107]. Alterations in neuronal morphology and branching patterns have been observed in a wide range of developmental or acquired disorders [108-111] in which it is thought that altered arbor structure plays a role in the pathogenesis of the disorder. Understanding the factors affecting neuronal morphology is, therefore, integral to understanding nervous system health and disease.

Neuronal morphology is a complex phenomenon to study due to the wide range of metrics which may be quantified [112, 113]. The need for streamlined methods of acquiring neuronal morphological data has given rise to a growing number of fully-automated and semi-automated tools [114-118]. Each has unique strengths and weaknesses associated with removing user control and relying on computers for neurite identification, resulting in a trade-off between speed and reliability. Often, neurite morphology is analyzed by counting the total number of neurites, branch points, tips, or by Sholl analysis (Fig. 3.2-1 A) [119]. Each of these methods used in isolation falls short of providing a full description of arbor morphology because it is possible to generate the same output from two different input arbors (Fig. 3.2-1 B-C) [113]. Additionally, the pattern of dendritic and axonal extensions is a result of cytoskeletal assembly and disassembly processes regulated by intracellular and extracellular factors. Because of the highly local role of many of these regulatory processes, final arbor morphology is a

product of specific effects acting locally in each neurite. Axons and dendrites, for example, develop distinct morphological behaviors even when exposed to the same global environment [120]. The application of these data extraction techniques to whole neuronal arbors destroys the ability to observe local changes. These failures of neuronal arbors destroys the ability to observe local changes. These failures of traditional data-generating tools make it difficult to test specific hypotheses about the biochemical processes driving arborization. This problem is compounded by the time associated with manual quantification, which makes it impossible to practically employ more than a very few quantification techniques, limits data sharing opportunities between laboratories, and creates problems with reproducibility and data auditing [117].

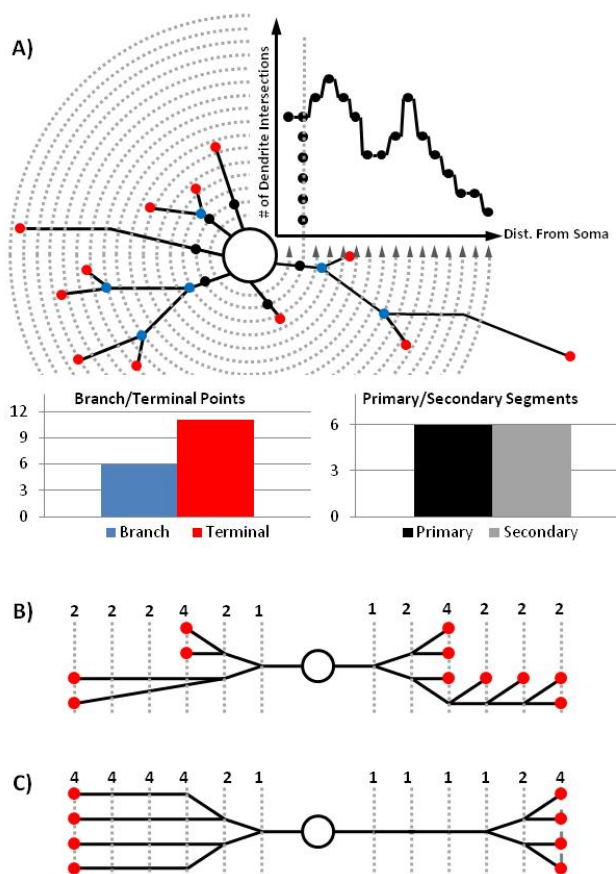


Figure 3.2-1. Schematic of several classic morphological analysis tools

A) Schematic of Sholl analysis, branch/terminal point counting, and segment counting. B) Two distinct arbors

(left and right) that generate identical Sholl curves. C) Two distinct arbors (left and right) that generate identical terminal point and branch counts.

In this study, we report the release of a unique tool that incorporates two existing morphological analysis platforms, along with custom analytical components, to provide detailed neurite-level morphological data. The program incorporates NeuronJ [114] to acquire spatial information about the position of neuritic segments in space relative to the rest of the cell (Fig. 3.2-2 B). It then exports this information to NeuronStudio [121] to allow the user to define structural information about the connectivity between neurites (Fig. 3.2-2 C). Custom portions of the program then assign “identities” to each neuritic segment according to its location within an arbor. Assigning an identity to each segment allows the program to perform a series of analyses relating morphological metrics to segmental identity (Fig. 3.2-3). The workflow created is intended to streamline data digitization and storage processes while preserving the reliability of user control.

We validate the program’s ability to detect changes in arbor morphology by applying this analysis to neurons incubated with BDNF, a well-studied extracellular factor that regulates neurite morphology [122-124]. Most studies have found that BDNF increases dendrite number close to the soma and reduces distal dendrite number [125, 126]. BDNF promotes similar increases in proximal axon complexity [127-129]. Historically, BDNF has been shown to increase dendrite complexity [130, 131] and number [132] by altering the rates at which new dendrite branches are gained and lost [132]. The exact mechanisms by which these effects are mediated are still debated and may differ by cell type or location in the same cell [133-136]. Bonfire analysis was applied to our experimental data to assess whether this novel analysis detects effects of BDNF on neurites that may have been missed by conventional Sholl analysis.

2.2.3 Materials & Methods:

2.2.3.1 *Cell Culture & Imaging*

Hippocampal neurons were isolated from E18 rat embryos and cultured as previously described [137]. Briefly, embryos were removed by Cesarean section at 18 days gestation and decapitated. The hippocampi were manually dissected under a microscope, and cells were triturated with a fire polished glass pipette tip, counted on a hemocytometer, and plated at a density of ~1800 cells per mm² on 35 mm petri plates (Corning) coated with 1 mg/ml poly-D-lysine (Sigma-Aldrich). Cultures were maintained in Neurobasal medium containing penicillin, streptomycin, glutamine, and B27 supplement (NB; all purchased from Invitrogen).

At 5 days *in vitro* (DIV5), cells were transfected with cDNA encoding GFP using Effectene (Qiagen), as previously described [138-141]. The low efficiency of this transfection technique in this cell system allows the easy identification of the processes associated with single neurons. In the BDNF treatment groups, treatment occurred from DIV7-10, during which regular NB was replaced with NB containing 25 ng/ml BDNF. This BDNF concentration does not stimulate p75 or other Trk (A and C) receptors, [142]. Cultures were fixed in 4% paraformaldehyde on DIV10 and immunostained with rat anti-GFP (a gift from Dr. Shu-Chan Hsu, Rutgers University) and MAP-2 (Sigma-Aldrich). Neurons were imaged in the GFP channel at 200x using an Olympus Optical IX50 microscope with a Cooke Sensicam CCD cooled camera, fluorescence imaging system, and ImagePro software (MediaCybernetics). Images were acquired in 8-bit TIFF format, measuring 512 X 640 pixels.

2.2.3.2 Program Mechanics & Usage

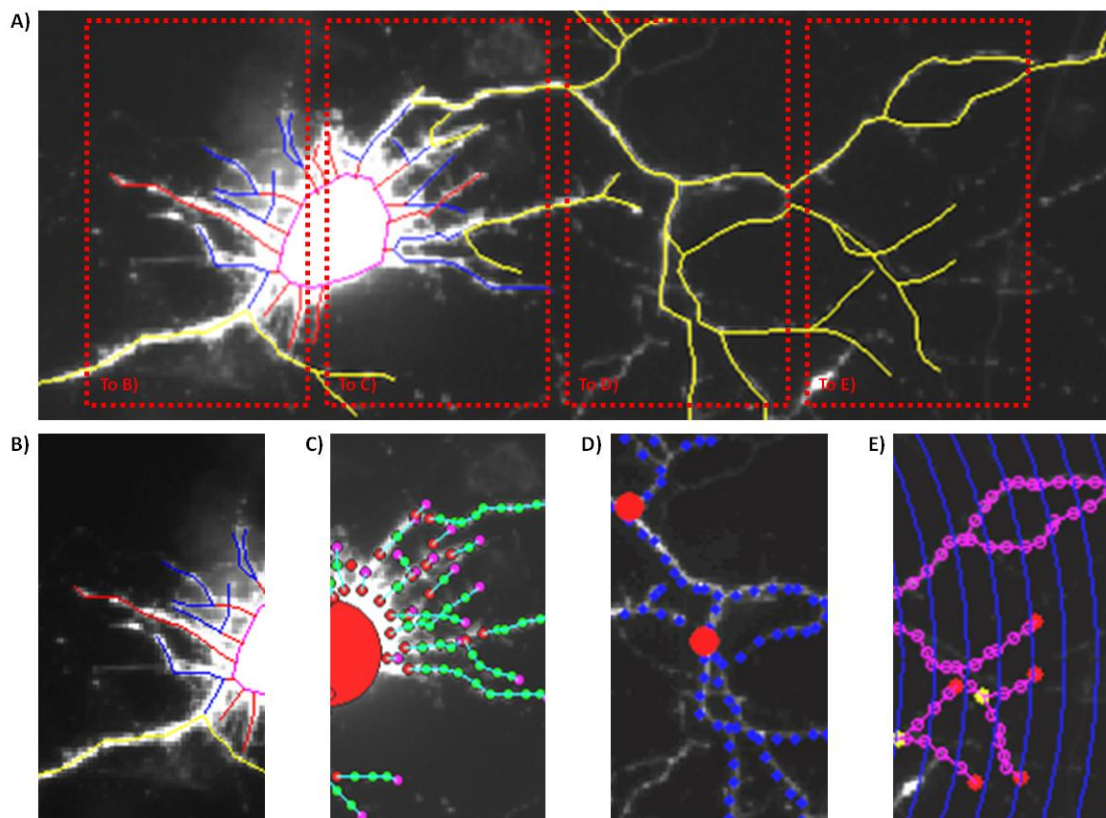


Figure 3.2-2. Schematic of the digitization and analysis process available through the Bonfire program

A) A neuron that has been “skeletonized” as a first step in digitizing its structure. B-E) Example graphical output of each step of the Bonfire procedure, as applied to segments of the image shown above in A). Example non-linkage errors (D, red spots) have been left in the figure intentionally to demonstrate Bonfire program error identification. Each step is performed on the entire neuron, but are shown in panels to emphasize the sequence in which they occur.

The Bonfire program is a series of custom scripts written in MATLAB (MathWorks). Neuronal morphology was digitized in three stages based on the initial images. In the first stage, the semi-automated tools available through the NeuronJ plugin [114] to ImageJ (NIH, Bethesda MD) were used to define positions of all neurites (Fig. 3.2-2 A-

B). The data for each neurite are exported using NeuronJ in the form of a series of nodes with defined positions in the X-Y plane, where nodes belonging to an individual neurite segment are linked by association. These tools allow the user to guide the tracing of each neuritic segment with course resolution by hand but reduce tracing time by using a curve-fitting algorithm to fine-tune the exact location of the nodes defining the neurite position.

In the second stage, portions of the Bonfire program were used to convert the strings of nodes provided by NeuronJ into SWC format [143] for further manipulation. NeuronStudio [121] is then used to define the pattern of connectivity between neurite segments (Fig. 3.2-2 C). The transformation of the data into SWC format allows for the linkage of the simple strings of nodes defined previously into more complex branching structures. After linking is complete, another component of the Bonfire program checks the resulting structure for errors and non-linkages (Fig. 3.2-2 D), based on the assumption that each neuritic segment may only give rise to two or less daughter segments [144]. This assumption is made to facilitate future integration with theoretical growth models [145] and does not result in significant loss of data [146]. These two steps fully determine the structure of each cell's neuritic arbor in 2-dimensional space and encode it in a digital format.

Using these digitized neuritic arbors, a second component of the Bonfire program was then used to perform process identification and extract the following metrics: number of primary neurites, number of secondary neurites, number of branch points per cell, number of terminal neurite tips per cell, and Sholl analysis performed with a 3.0 μm ring interval (Fig. 3.2-2 E). Sholl analysis is performed conceptually by drawing concentric circles around the cell body at incrementally increasing radii and counting the number of times each circle crosses a neuritic segment (shown counting around the

circle counterclockwise for demonstration in Fig. 3.2-1 A). The number of intersections is graphed as a function of radial distance from the cell body (Fig. 3.2-1 A upper right quadrant) to give a quantitative representation of how neurite density varies spatially.

Because the location and linkage pattern of neurites is user-defined using external tools, the algorithms associated with data extraction are geometric in nature and do not depend on conceptually complex image analysis. For example, the algorithm for Sholl analysis is based on the assumption that if a neuritic segment starting at one node (node N_n with Cartesian coordinates X_n, Y_n) lies inside of a soma-centric circle with radius r (C_r), and its daughter node (node N_{n+1} with Cartesian coordinates with coordinates X_{n+1}, Y_{n+1}) lies outside of radius r , then that neurite must cross the circle with radius r . C_r is also intersected by this neuritic segment if the reverse is true. Therefore, C_r is intersected by a neuritic segment when the criteria outlined in Equation 1 are met, as follows:

$$\left[\left(\sqrt{X_n^2 + Y_n^2} < r \right) \cup \left(\sqrt{X_{n+1}^2 + Y_{n+1}^2} \geq r \right) \right] \cap \left[\left(\sqrt{X_n^2 + Y_n^2} \geq r \right) \cup \left(\sqrt{X_{n+1}^2 + Y_{n+1}^2} < r \right) \right] \quad \text{Eq. 1}$$

The above holds true regardless of the spacing between nodes defining a neurite path, and so can be used for all mother-daughter node pairs. To return the cumulative Sholl curve, this same check is performed between every mother-daughter node pair and every circle, and the results are summed by circle. Because every node is checked for the existence of a mother node, this reliably returns the Sholl information for the entire arbor. Furthermore, because every node-pair can be tagged with a structure-based identity, it is possible to later tabulate which identity-classes intersect with specific circles. Additional descriptions of the algorithms involved in data management can be found as comments in the MATLAB code accompanying this article. Afterward, data

were transferred to Excel to facilitate statistical analysis. The experimenter was blinded to experimental conditions during all data analysis.

2.2.3.3 Branch Identity-specific Data Analysis

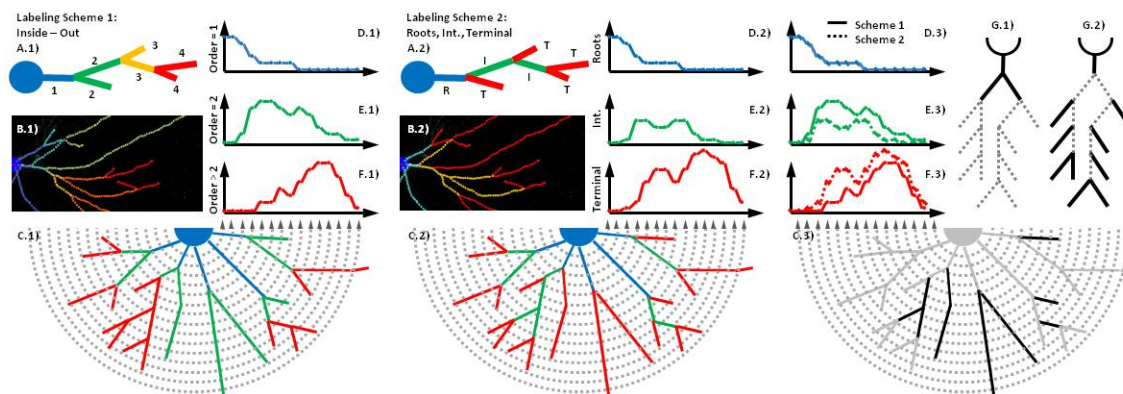


Figure 3.2-3. Two structure-dependent labeling schemes that assign an identity to neurite segments based on their location within their arbors

A) Randomly generated arbor, labeled according to the “Inside-out” scheme (I/O – A.1) or the “Roots, Intermediate, Terminal” scheme (RIT – A.2) [113], and color-coded according to order. B) An example neuritic arbor, which has been digitized and color-coded according to branch order using I/O labeling (B.1) and RIT labeling (B.2), respectively. C) Schematized example neuritic arbor, color-coded according to I/O labeling (C.1) and RIT labeling (C.2), respectively, with super-imposed Sholl rings. D-F) The order-specific Sholl curves resulting from the arbors shown in Fig 3.2-2C. C.3) Example arbor in gray, showing neuritic segments that change groupings between the two labeling schemes (black), accompanied by a schematic showing the relative areas of emphasis for the I/O (G.1) and RIT (G.2) labeling schemes.

Two labeling schemes were used to assign structure-based identity to segments, which allow us to analyze subregions of the arbor with varying degrees of specificity. Neuritic segments, or branches, are the uninterrupted stretches of neurite starting at one branch point, or starting at the cell body in the case of root segments, and ending when the neurite terminates or at the next branch point. These segments can be grouped together in different ways. In the most frequently used convention, these processes are

assigned a number, or branch order. In this convention, termed “inside-out” labeling (I/O) here, branch order starts at 1 with any branch initiating at the soma and increases by 1 with each branch point reached, moving from the soma to the branch tips (Fig. 3.2-3 A.1 – F.1) [113]. The second convention is the “roots, intermediate, terminal” (RIT) convention (Fig. 3.2-3 A.2 – F.2), in which any neurite originating in the soma is a root segment, any neurite with no daughter neurites is a terminal segment, and any neurite not a root or a terminal is an intermediate segment [113].

Having neurites assigned segmental identities in I/O and RIT labeling allows the performance of more traditional forms of analysis on specific subregions of the arbor. For example, Figure 3.2-3 A.1 – F.1 shows Sholl analysis performed on neurite segments that have been consolidated into three separate groups based on their structural identity, resulting in three separate Sholl curves for the same cell. This technique is performed the same way as standard Sholl analysis but uses three possible groupings of segments. In the example shown in Figure 3.2-3, the first grouping contains only primary segments, and therefore, only the intersections of primary segments with the Sholl rings are tallied in the generation of the Sholl curve for that group (Fig. 3.2-3 D.1). In the second group, only secondary processes are counted, and in the third group, all segments with order ≥ 3 are counted, generating the Sholl curves shown in Figure 3.2-3 E.1 – F.1, respectively. A similar analysis can be performed using the RIT labeling scheme in which only the Sholl intersections with root segments (Fig. 3.2-3 D.2), intermediate segments (Fig. 3.2-3 E.2), or terminal segments (Fig. 3.2-3 F.2) are counted. Note that the sum of all the component Sholl curves adds up to the total Sholl curve for the cell, and therefore, is the same in both of these cases.

2.2.4 Results:

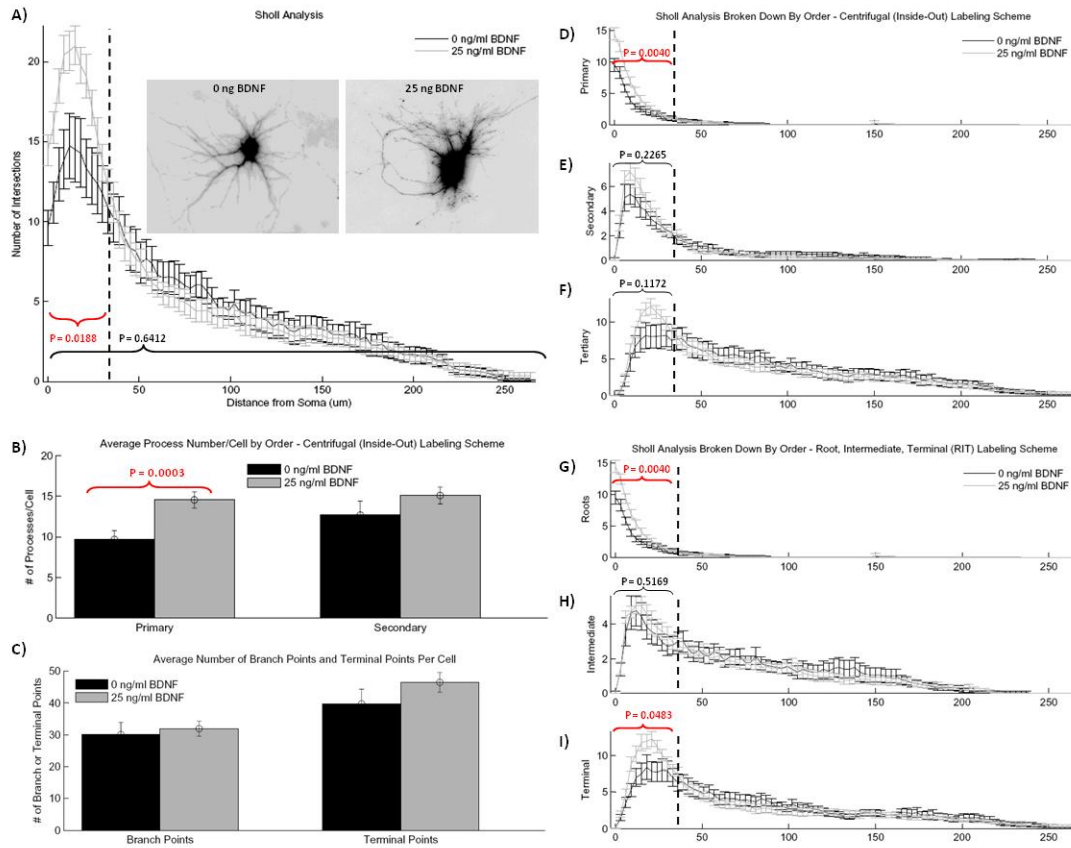


Figure 3.2-4. Results of Bonfire analysis for hippocampal neurons treated with 25 ng/ml BDNF and untreated control neurons

A) Total Sholl curves with example inverted GFP images (inset). B) Average number of primary and secondary processes per cell. C) Average number of branch points and terminal points per cell. D-F) Segment identity-specific Sholl analysis according to the I/O labeling scheme, where segments have been grouped as either primary (D), secondary (E), or tertiary and greater (F). G-I) Segment identity-specific Sholl analysis according to the RIT labeling scheme, where segments have been grouped as either root segments (G), intermediate segments (H), or terminal segments (I). All error bars represent the standard error of the mean (SEM). Statistical analysis of dendrite number was performed on the total number of Sholl intersections in the bracketed regions using two-tailed unpaired t test with Welch correction ($n = 18$ for 0 ng/ml BDNF condition, $n = 24$ for 25 ng/ml condition).

2.2.4.1 Global analysis:

As seen by other groups [127], global exposure to BDNF *in vitro* increases proximal neurites within the first 35 μm of the soma but has no effect on distal neurites (Fig. 3.2-4 A). Quantification of the number of primary and secondary neurites shows that BDNF treatment causes a statistically significant increase in the number of primary extensions, and while there is a trend of an increasing number of secondary neurites it does not reach statistical significance (Fig. 3.2-4 B). In addition, we analyzed the effect of global BDNF administration on the average number of branch points and number of terminal branches per cell (Fig. 3.2-4 C), which showed no change between conditions. Similarly, global BDNF exposure causes no significant change in average process length or total arbor length (data not shown). While the specifics of BDNF treatment vary based on the type of neuron and system (*in vitro* vs. *in vivo*) [125-129], these results are broadly consistent with the general scientific consensus that BDNF treatment increases arbor “complexity.”

2.2.4.2 Local analysis:

A more detailed picture of BDNF-induced morphological changes is created by the local-level Sholl analysis. RIT-based Sholl analysis identifies that the increased number of proximal Sholl intersections is due to two effects: 1) there is an increase in the number of primary neurites (Fig. 3.2-4 B), which causes an increase in the number of Sholl intersections with primary neurites (Fig. 3.2-4 D and G), and 2) there is an increase in the number of Sholl intersections with terminal neurites (Fig. 3.2-4 I). However, when the I/O labeling scheme is used (Fig. 3.2-4 D-F), only primary neurites appear to change significantly between conditions. This is because the neurite sub-type responsible for much of the change (terminal neurites) is split between the second two classifications using the I/O labeling scheme, making a statistically significant change impossible to

detect. Taken together, these two schemes indicate that the increase in proximal Sholl intersections is caused by increased primary sprouting as well as increased presence of low-order branches that terminate rather than branch into daughter segments.

2.2.5 Discussion and Conclusions:

2.2.5.1 *Morphological Analysis:*

The data generated during the study of neuroscience are as variable as the subject itself, including genetic, proteomic, morphological, electrophysiological, histological, and behavioral data. Even within the subtype of morphological data, there is no consensus on which metrics are most significant, and there are frequently multiple means of capturing, analyzing, and storing the data [118]. Consequently, every laboratory accumulates a unique set of tools according to their means and needs. Recently, researchers have turned increasingly to the field of neuroinformatics, which aims to create tools and standards to help integrate information across research platforms and laboratories [147]. In an environment where such diversity is required for its continued productivity, the development of tools meant to bridge existing platforms can be more effective than the development of tools which aim to vertically integrate all steps in analysis in one platform.

Digitizing neuronal morphology generally consists of 6 steps: 1) image acquisition, 2) skeletonization, 3) generation of meta-data, such as arbor structure, 4) quantification, 5) analysis and interpretation, and finally, 6) data storage. Numerous software packages have been developed to assist neuroscientists in these various steps, including automated [115, 117, 148] and hand-assisted [114] skeletonization tools, neurite linking tools [121, 149, 150], automated data-analysis tools [116, 151], and database tools [152, 153]. One notable absence from the collection of available open-source tools is a method for deriving Sholl profiles, which interfaces with the other tools used to digitize

neuronal morphology. Current Sholl tools available for download operate by simple image thresholding [154], are entirely user-driven [149, 155], or provide limited and highly specific output [121]. While commercial alternatives exist, they are frequently cost-prohibitive and cannot be altered to meet unique demands.

The Bonfire program integrates with two existing tools used in neuronal digitization (NeuronJ and NeuronStudio) and provides a means of extracting Sholl profiles from digitized neurons stored in standard SWC format. Furthermore, the linkage of an automated, structure-based labeling system with an automated Sholl analysis algorithm creates a powerful new method for quantifying highly specific changes occurring in dendrites and axons following genetic or pharmacologic manipulations. The reason for having multiple methods of segmenting the data is that each method only focuses on a small region of the neuritic arbor, making it better suited to identify effects in that region. The I/O scheme focuses on primary and secondary neurites at the expense of higher order neurites (Fig 3.2-3 G.1, D.3 – F.3). Such a scheme may uncover morphological effects caused by factors acting at the cell body but may miss changes preferentially affecting only the more terminal regions of the arbor. Conversely, the RIT scheme captures effects of factors at terminal segments but causes a loss of resolution in the intermediate segments since they are grouped together (Fig. 3.2-3 G.2, D.3 – F.3). The RIT scheme is best for identifying factors that affect the stability or creation of terminal segments, but this scheme misses effects that occur close to the cell body. The difference in regions of focus between the two schemes is generated by their accounting for the same set of processes differently (Fig. 3.2-3 C.3). This identity-specific information reveals trends in neurite patterning, which were previously obscured by global-level analyses.

2.2.5.2 Biological Findings:

Primary segment numbers confirm that BDNF exposure increases primary neurite number. However, the absence of a significant change in the number of branch points or terminal points and the lack of a change in the average segment length implies that the effect of BDNF is not due to overall increased neurite branching. Taken together with the absence of a change in the total arbor length, these findings, which represent an entirely new function for BDNF, suggest that global exposure of hippocampal neurons to BDNF *in vitro* results in a reorganization of neuritic segments within their arbors but not necessarily a change in overall neurite number or length.

Data extracted using Bonfire analysis provide a more detailed view of these morphological changes, and for the first time, tie the effects of BDNF to specific regions of the arbor. The importance of having the multiple methods of data segmentation provided by the two labeling schemes is clarified by the fact that the analysis identified not only a global effect of bath application of BDNF but also that this global effect is predominantly driven by a change in two specific arbor subregions. These details about the local nature of morphological changes have not been identified using conventional methods [139, 155, 156].

2.2.5.3 Future Directions:

One of the most exciting opportunities opened by the generation of morphological data containing local-level detail on arbor structure is the ability to fuel mathematical exploration of the molecular processes locally guiding arborization [157-161]. Much work has been done deriving generative models of neuronal morphologies [162-165]. These models are based on observation, but their mechanics are meant to represent biological processes driving cellular morphology [157-159, 166]. Providing these models with a more detailed source of experimental data would improve mathematicians' ability to

generate and test specific hypotheses about biochemical regulatory networks. As mentioned previously, final arbor structure is a result of balanced cytoskeletal assembly and disassembly processes which are regulated by local and global factors. Detailed morphological analysis of specific regions of the dendritic and axonal arbors may provide a convenient window into the regulation of neuronal structure by locally active factors. The result would be a closer integration of mathematical modeling with experimental science.

For example, the mathematical interpretation of Sholl data can be performed using multiple methods [161]. The selection of the most informative one may be dependent on cell type, or even the process type within one cell, implying that the biological drivers of neurite branching and growth may change based on context. However, even using multiple mathematical approaches, interpretation of standard Sholl analysis is not straightforward. An observed increase in Sholl intersections may be due to a variety of changes in branching behavior, including increased sprouting from the soma, more rapid neurite bifurcation, delayed termination, or even neurite extension from the periphery back toward the soma. It is therefore necessary to determine the contribution of each process type to the overall Sholl curve if such information is to be instructive of the underlying biological processes.

2.2.5.4 Conclusions:

The Bonfire program provides a useful bridge to integrate several existing digitization tools, makes the data available in a variety of formats (.swc morphological descriptions of individual neurons, .xls summary reports, and graphical analysis provided within MATLAB), and assists in the generation of morphological databases where information is stored concisely and can be revisited with unique analyses or audited for correctness as the need arises without having to re-digitize the data. The Bonfire program capitalizes

on the strengths of previously developed tracing programs to reduce the time required for high-fidelity tracing, while preserving the flexibility of laboratories to generate digitized neuronal files using their own preferred method. Though the program currently integrates most effectively with NeuronJ and NeuronStudio, it operates on standard SWC encoded neuronal information, which can be created using a variety of methods. Furthermore, the MATLAB code is readily available for modification, enabling users to modify or expand on the analysis to meet their own needs. In making this tool freely available, we hope to increase the accessibility of high-quality morphological analysis tools to the scientific public and to establish a precedent for building and sharing open-source tools for improved morphological analysis of neurons.

2.3 Semi-automated spike sorting for increased information retrieval from microelectrode array recordings

2.3.1 Abstract:

Microelectrode arrays (MEAs) measure the activity of multiple neurons on a single channel. In order to take full advantage of this technology's ability to measure neuronal or muscle cell activity, on both the scale of single cells and the scale of cell networks, it is necessary to identify the activity of individual cells within MEA data. There are many techniques for doing so, and no consensus on which one works the most effectively. Selection of an appropriate process is, therefore, based on the requirements of particular experiments and constraints of the experimental set up. We have composed a program which successfully allows a user to identify the activity of individual cells in MEA data. It is flexible enough to identify activity from multiple cell types (myotubes and neurons) and returns accurate information on the morphology, as well as the timing, of their action

potentials. Furthermore, the program reduces the time required to analyze the data and the user-introduced bias by partially automating the process.

2.3.2 Introduction:

2.3.2.1 *A New Type of Data*

Neuroscience research produces data on a wide range of scales. At the molecular level, genes encode protein structure, and protein activity is regulated through protein/gene interaction networks. At the single neuron level, protein activity affects morphology and membrane composition, which can in turn affect how single neurons process and transmit action potentials. At a multicellular level, the behavior of such individual units affects how networks of neurons will behave. At a tissue level, the behavior of large neuronal networks dictates the function of the central nervous system and goes on to control organism behavior. Therefore, nervous system health and disease is a function of events occurring across multiple levels of complexity and scale. Understanding the linkages between levels increases our depth of understanding, and the potential for findings at one level to have implications on other scales.

The relatively recent popularization of MEA technology now allows neuroscientists to examine neuronal behavior on a single neuron- and network-level. MEAs record extracellular voltage traces (EVTs) from multiple interacting neurons, for relatively long periods of time, both *in vivo* and *in vitro*. Analyzing and interpreting this wealth of new data has created a challenge that requires the convergence of computational and experimental techniques [167]. Researchers using this technology must have an understanding of the nature of the data that are recorded, the mathematical and computational methods for processing these data, and the biological basis for data generation and significance.

2.3.2.2 Extracellular Voltage Traces (EVTs)

Recording neuronal EVT is performed by placing a conductor, which is connected to a recording device, in the vicinity of a neuron's soma where neuronal action potentials create their largest transmembrane currents [168, 169]. This rapidly changing current creates voltage transients that can be transmitted along the conductor and subsequently recorded. A conductor will transmit all such activity along its length, so regional specificity is achieved by insulating all of the conductor except the points from which you want to record activity. *In vivo* MEAs, for example, usually consist of arrays of conducting wire, insulated along their length except for the tip. *In vitro* MEAs consist of conducting layers deposited on top of a glass slide and insulated everywhere except at the contact pads (Fig. 3.3-1, A).

Extracellular voltage at any point is the sum of a number of factors, including the activity of any neurons close enough that their APs can be detected (Fig. 3.3-1, B) [167], as well as noise [170]. Because neurons are frequently packed closely together (*in vitro* and especially *in vivo*), this means that any EVT may contain information from any number of neurons. The interpretation of data from multiple neurons recorded on a single channel is a complex problem that has been likened to trying to understand the function of an orchestra without any knowledge that the final sound is generated by different instruments playing simultaneously [168]. Similarly, the most meaningful interpretations of neuronal activity depend on knowing the activity of single cells, due to the nature of information exchange through action potentials (APs). Figure 3.3-1, E shows a schematic of one possible arrangement of neurons on an MEA. Neurons are networked selectively (and color-coded by network), and contact pads are shown in black. Synchronous depolarization of a network would result in nearly simultaneous event detection on each of the pads contacted by that network. The blue network and

green network would be easily differentiated based on the pattern of activated electrodes because they do not spatially overlap. However, the green network completely overlaps the red network, making differentiation between the two far more difficult. Figures 3.3-1, F-G show unsorted sample data recorded from 22 electrodes in a culture where the situation of overlapping networks likely exists. The vertical banding apparent in Figure 1, F indicates that networks are present, and are causing synchronous activity. The expanded view (Fig. 3.3-1, G) further shows that this activity is likely a combination of a large network causing activation of a majority of electrodes (indicated on the bottom of Fig. 3.3-1, G with green arrows), and a smaller network on a subset of these electrodes (bottom of Fig. 3.3-1, G with red arrows). Teasing out the behavior of these networks, and therefore making full use of the EVT information, requires determining the firing patterns of each neuron whose activity is recorded by any one electrode.

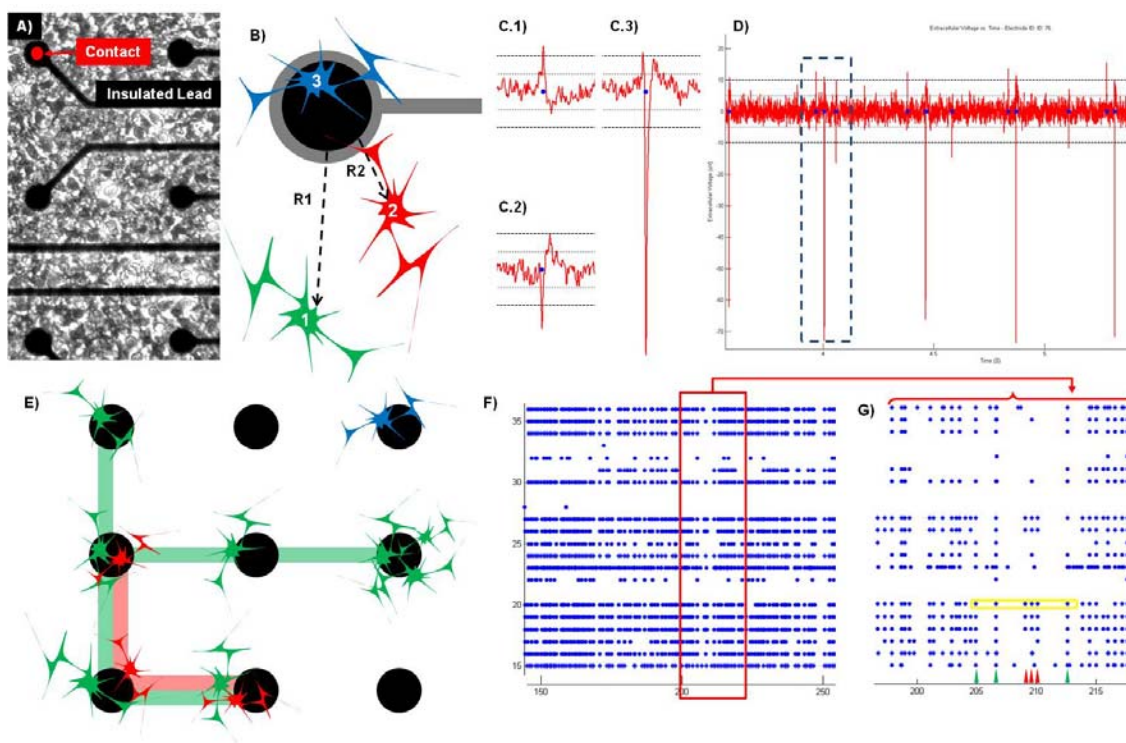


Figure 3.3-1. Recording and interpretation of EVT using and MEA

A) Phase microscopy of muscle-cell culture on commercially available MEA. B) Schematic representation of potential neuron locations relative to contact pad on MEA. C) Example segments of EVT recorded from a single electrode, showing three distinct spike morphologies (small-positive, small-negative, and large-negative), indicating the likely presence of three nearby neurons. Threshold levels used for spike detection indicated by black dashes. D) 2 Seconds of example EVT data recorded demonstrating temporal relationship of spike events. E) Schematic representation of neuronal culture on MEA, showing multiple active units with multiple patterns of connectivity. F) Example spike trains from unsorted EVTs (Time is on the X axis, electrode ID is on the Y axis). Each row corresponds to an electrode, and each blue dot indicates a spike occurrence at that time. G) A close-up of 20 s of data. The vertical alignment of events qualitatively shows that there is network activity (green and red arrows on the bottom axis), but because the units are not sorted by biological source (only by electrode location), it is impossible to quantitate the linkage between cells.

Neurons are believed to communicate through discrete events (APs), which occur at specific points in time. Such phenomena are modeled using “point processes” in probability theory [167]. The EVTs recorded from an MEA, however, are continuous measures of extracellular voltage over time (an example segment of an EVT is shown in in Fig. 3.3-1, D). The computational techniques used to translate continuous EVTs to point processes representing the single cell activity of an unknown number of neurons are therefore the mandatory first step in analysis of this type of data [167]. Though this task is a formidable one, it is made possible by the fact that every neuron fires action potentials resulting in EVTs with a signature shape specific to only that neuron [167, 168]. Figure 3.3-1, C shows three differently shaped events recorded in an EVT from a single electrode. This is because each individual neuron has a unique location and orientation relative to the electrode contact, and the quality of extracellular environment separating the two is unique [169]. The process by which each depolarization event recorded in an single-electrode EVT is assigned to a particular neuron is known as “spike sorting [171].”

2.3.2.3 Spike Sorting Process

The process of spike sorting can be roughly broken into a three step process shown in Figure 3.3-2 [172]: 1) likely spike events are identified in the continuous EVT, 2) features that may be used to identify the origins of these events are defined, and 3) the events are classified into multiple groups based on the clustering of these features. While there are additional methods of interpretation that do not rely on spike sorting [173-175], these will not be considered here. There are multiple methods for performing each step of the process mentioned above, and there is no consensus on which performs best [167, 171]. Technique validation is further complicated by the fact that each step is largely modular and may therefore be used with many combinations of the other steps and that there is a large amount of variability associated with hand sorting of the data (considered the gold standard) [172]. Consequently, there are essentially limitless permutations of analytical techniques and no real means for comparing their efficacy.

Selecting the best set of algorithms is, therefore, primarily a function of what the data are needed for subsequently. Experimenters looking to answer specific questions may be able to tolerate one type of uncertainty in favor of gaining specificity on some other metric. This unique set of constraints, determined by their experimental design, will dictate the correct assembly of their spike-sorting process.

2.3.2.4 Program Goals

Our experimental designs aim to assess the ability of substrate-embedded MEAs to record from or stimulate muscle cells as well as neurons. Furthermore, we would ultimately like to be able to identify coupling of biological, signal-producing units. We are therefore interested in being able to observe and quantify the characteristics of the EVTs generated by both cell types as well as the sequence with which they occur. Finally,

because the task of spike sorting by hand is such a long one and can introduce so much bias, we need to develop a semi-automated process which reduces the burden on the experimenter and improves reproducibility.

Because we are working with muscle cells, we will face a number of unique problems. In particular, the APs generated by the muscle cells are likely to produce widely variable spike shapes between units due to the unique shape of each cell. Additionally, even the EVTs produced by a single cell are likely to show wide variability because the cell is capable of movement relative to the electrode over the course of AP generation. Finally, we will be using custom electrode designs where each electrode is likely to have differing noise levels because of their different dimensions.

A program to semi-automate the process of spike sorting was designed with the above goals in mind and composed in MATLAB (Mathworks, Natick MA) to accept data from a Multichannel Systems MEA recording setup. In this program, an attempt is initially made to automatically analyze all data. The program then prompts the user to “proof” the data and guides the user through a revision analysis on data segments where the automated process failed to sort the units correctly. The algorithms involved in the program, and the rationale for their selection, are discussed below. Sample data sets of neuronal and myotube recordings were analyzed to confirm functionality.

2.3.3 Materials & Methods:

2.3.3.1 Cell culture and sample data acquisition

Myoblasts and cortical neurons were isolated and cultured as previously described in the literature [1, 54, 88, 89]. Briefly, pregnant Sprague Dawley rats were sacrificed by CO₂ inhalation at gestational day 21 for myoblasts and 18 for cortical neurons, in accordance with Rutgers University animal care procedures. To isolate cortical cells, pups were removed by Cesarean section and cortex was isolated and the meninges

removed, and cortex was triturated to create a single cell suspension. Cortical cells were then seeded onto MEAs in MEM medium plus 1% penicillin/streptomycin, 10% horse serum, and 3% v/v of 20% glucose solution at a surface density of 225,000 cells/cm². Prior to use, the medium was glutamate depleted by 24 hr exposure to astrocytes culture, and the MEA surface was incubated overnight in 3% PEI dissolved in borate buffer. To isolate myoblasts, pups were removed by Cesarean section and hind limb muscles were removed to a separate container of Hanks' Balanced Salt Solution (Invitrogen, Carlsbad, CA) + 1% HEPES Buffer (Mediatech, Inc., Herndon, VA). Tissue was finely minced and brought to a final volume of 7 ml in PBS containing 1.5 U/ml collagenase (type D, Roche, Mannheim, Germany) and 2.5 U/ml dispase (type II, Roche, Mannheim, Germany). Tissue slurry was then incubated for 20 min at 37° C and triturated using a pipette to break up remaining tissue clumps. Solid debris was allowed to settle for 15 minutes, and remaining cells were pelleted out of the supernatant by centrifugation. The cell pellet was resuspended in growth medium consisting of Ham's F-10 medium including 20% fetal bovine serum, 1% Penicillin/Streptomycin, (all from Invitrogen, Carlsbad, CA) and 2.5 ng/ml human b-FGF (Promega Corporation, Madison, WI). Cells were then plated into 75 cm² flasks and incubated for 24 hrs to allow for attachment of viable cells. Cultures were washed 3X with PBS to remove non-adherent cells and debris. Cells were then resuspended and plated onto commercially available MEAs (Multichannel Systems) at a density of 100,000 – 300,000 cells/cm² depending on the experiment in differentiation medium consisting of Neurobasal medium including 2% B-27 Supplement, 1% Penicillin/Streptomycin, and 1% GlutaMAX (all from Invitrogen, Carlsbad, CA). Prior to seeding, surfaces were coated with laminin (Sigma Aldrich, St. Louis, MO) at 40 µg/ml. Recordings were made using a standard MCS recording array, sampling the extracellular voltage from 60 contact pads at 20,000 Hz. Contact pad

spacing was 200 μm and diameter was 10 μm . Recordings were made throughout the development of cultures to observe a wide variety of behaviors.

2.3.3.2 Data analysis

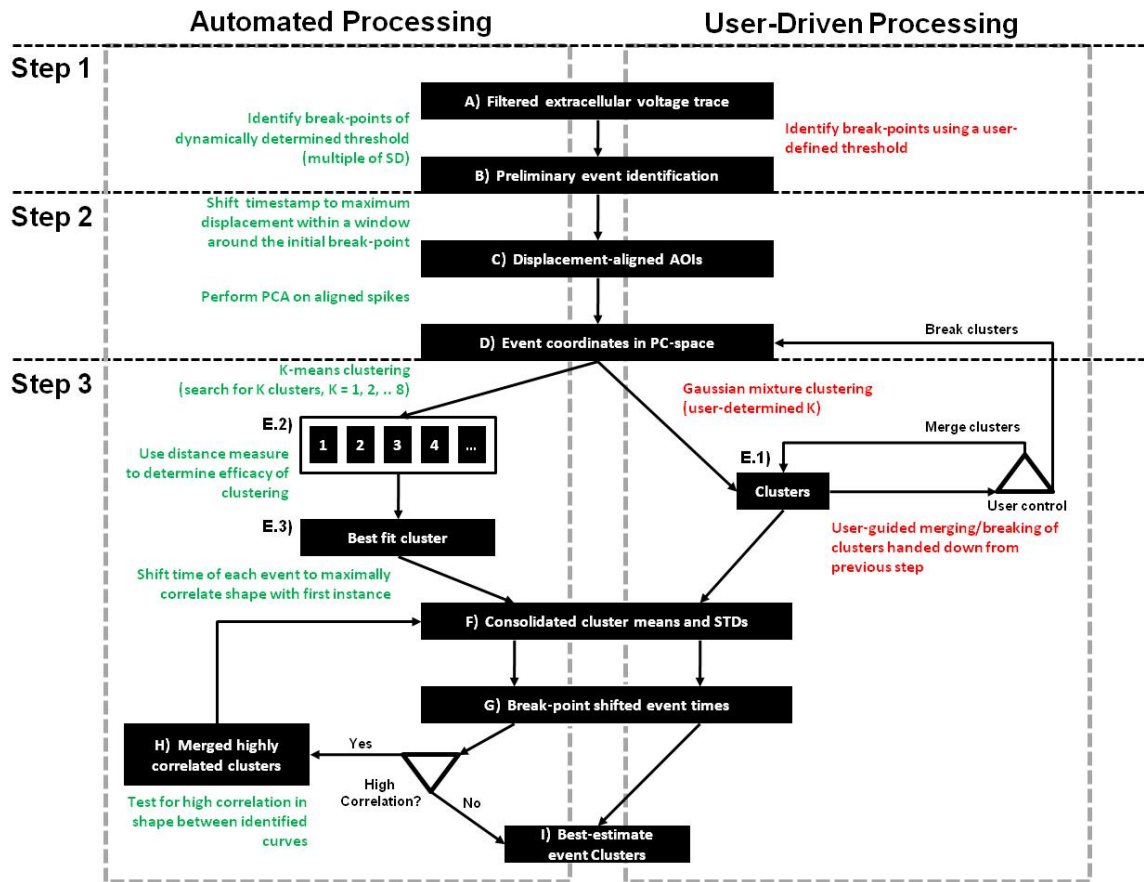


Figure 3.3-2. Schematic of spike-sorting algorithm.

2.3.3.2.1 Event Detection

The detection of unsorted spike events is typically performed by amplitude thresholding in which all instances where the EVT exceeds a certain threshold are recorded as potential spikes [176]. While other methods exist [171, 172], they were not considered here for reasons of algorithmic simplicity and because they are based on assumptions best suited for neuron-only EVT. The highly variable EAP morphologies

expected from myotube cultures, however, and the variable noise amplitude expected on custom MEAs makes selection of an appropriate threshold level complicated. An adaptive thresholding technique was therefore used, in which the spike-threshold is set to a multiple of the SD for the entire data segment [172] (Fig. 3.3-2, B). Additionally, because myotubes are expected to depolarize over a variable length of time, a variable “blanking window” was imposed after each instance where the threshold was broken. After an event is detected, the blanking window prevents the identification of subsequent events for a set time.

2.3.3.2.2 Feature Generation

Features representing spike characteristics can be generated based on a wide variety of techniques. Some draw from very obvious morphological characteristics which are apparent to the naked eye, such as amplitude and duration [171], or template matching [176, 177]. Others draw on computational techniques to generate less obvious characteristics, involving Fourier [178] and wavelet transforms [179]. Principal Component Analysis (PCA) was selected for our algorithm because of the high degree of flexibility it provides relative to its computational simplicity [172]. A full discussion of PCA is outside the scope of this discussion, but briefly, it identifies the variance between sets of vectors and returns basis-vectors that explain this observed variance in rank order of importance, known as the principal components (PCs). In other words, it is a way of automatically generating features based on the variability in the dataset it is run on. This means that a custom set of PCs is created for each electrode’s EVT recording rather than needing a set that is applied to all EVTs equally.

The first step of PCA is creating the set of vectors it is run on. This is done by taking each fragment of the full EVT that was identified as a likely spike and aligning them. In our case this is a multi-step process in which we 1) identify an instance of where the

EVT breaks the spike-threshold, 2) establish an investigation window around that point, 3) identify the maximum amplitude of the EVT within that window, 4) assign the point of maximum amplitude as the event center, and 5) realign each event to that point (Fig. 3.3-2, B-C). Figure 3.3-3, A shows three example incidences where the spike threshold was broken and establishment of the interrogation window (thick red line) and blanking window (dashed red line) around that point. The size of the interrogation window (both lead time and lag time) can be adjusted as needed. Figure 3.3-3, B shows all incidences from 60 S of example data aligned to maximum deflection point, as described above. PCA is then run on the set of aligned spike vectors (Fig. 3.3-2, D), and the first two PCs (Fig. 3.3-3, B blue lines) are used to generate a 2 dimensional feature space. Figure 3.3-2, C.1 shows this feature space (the first and second PCs are the X- and Y-axis, respectively), in which every spike instance can be placed as a point based on its resemblance to PC1 and PC2, respectively.

2.3.3.2.3 *Clustering*

While a number of alternative clustering algorithms are available [179, 180], our program uses either K-means or a Gaussian mixture (GM) algorithm, depending on what phase of operation the program is in. Automatic analysis utilizes the K-means approach, while user-assisted analysis takes advantage of the GM process. In either approach, the process roughly progresses as a series of trial-and-error attempts to identify the “correct” number of clusters that best explains the data, followed by an assessment of how successful the effort was.

During user-assisted analysis, the user defines the number of clusters the GM process should look for. Then, based on these clusters, the user may select clusters to split or join until optimal sorting is achieved as defined by the user. Each time a cluster is split, it is reanalyzed in its own PC space rather than the PC space of the full data set,

which resulted in the original poor clustering (Fig. 3.3-2, E.1). During automatic clustering, the K-means algorithm is used. The program successively identifies 1 – 8 clusters in the data and scores the efficacy of the clustering based on a measure of the distance between all points in each cluster. Cluster sets where all points in each cluster are close to each other and far from the points in the other clusters are scored well, while cluster sets where points in each cluster are closer to the points from other clusters than they are to each other are scored poorly (Fig. 3.3-2, E.1). The cluster set receiving the highest score is assumed to be the most appropriate clustering of the data and is passed to the next step in the process. Figure 3.3-3, C1 shows example data that has been clustered (3 clusters were identified)

2.3.3.2.4 Post-processing and Recombination of Correlated Clusters

Following clustering, groups are “tightened” by shifting the time stamp for all events to the location where they are all maximally correlated with the first instance in their cluster. The cluster average and SD are then calculated (Fig. 3.3-2, F). All events in the cluster are therefore maximally correlated with this mean curve. The time at which the cluster average breaks the threshold is then assigned as the event time for all events in that group (Fig. 3.3-2, G). Finally, all curves are aligned to this break point and are cross-correlated. Spike groups where the correlation between their shapes is above a threshold value are then combined (Fig. 3.3-2, H). Figure 3.3-3, C shows the three traces from Figure 3.3-3, B after they have been assigned to clusters, corresponding to the activity of individual cells. Once this has been successfully completed, the firing sequence of each of these cells can be observed in the original EVT (Fig. 3.3-3, C.2).

2.3.3.2.5 Recursive Evaluation and Workflow

Once all data have been sorted automatically, the program allows the user to “proof” the spike identification process by showing the clusters obtained on each electrode. The

user then has the opportunity to accept the sorting, exclude the electrode altogether (as would be done with nonfunctional/noise electrodes), or to mark the electrode for revision analysis. The program uses the information to build a list of electrodes which need to be revisited and then allows the user to perform spike sorting by hand on these electrodes (Fig. 3.3-2, right side).

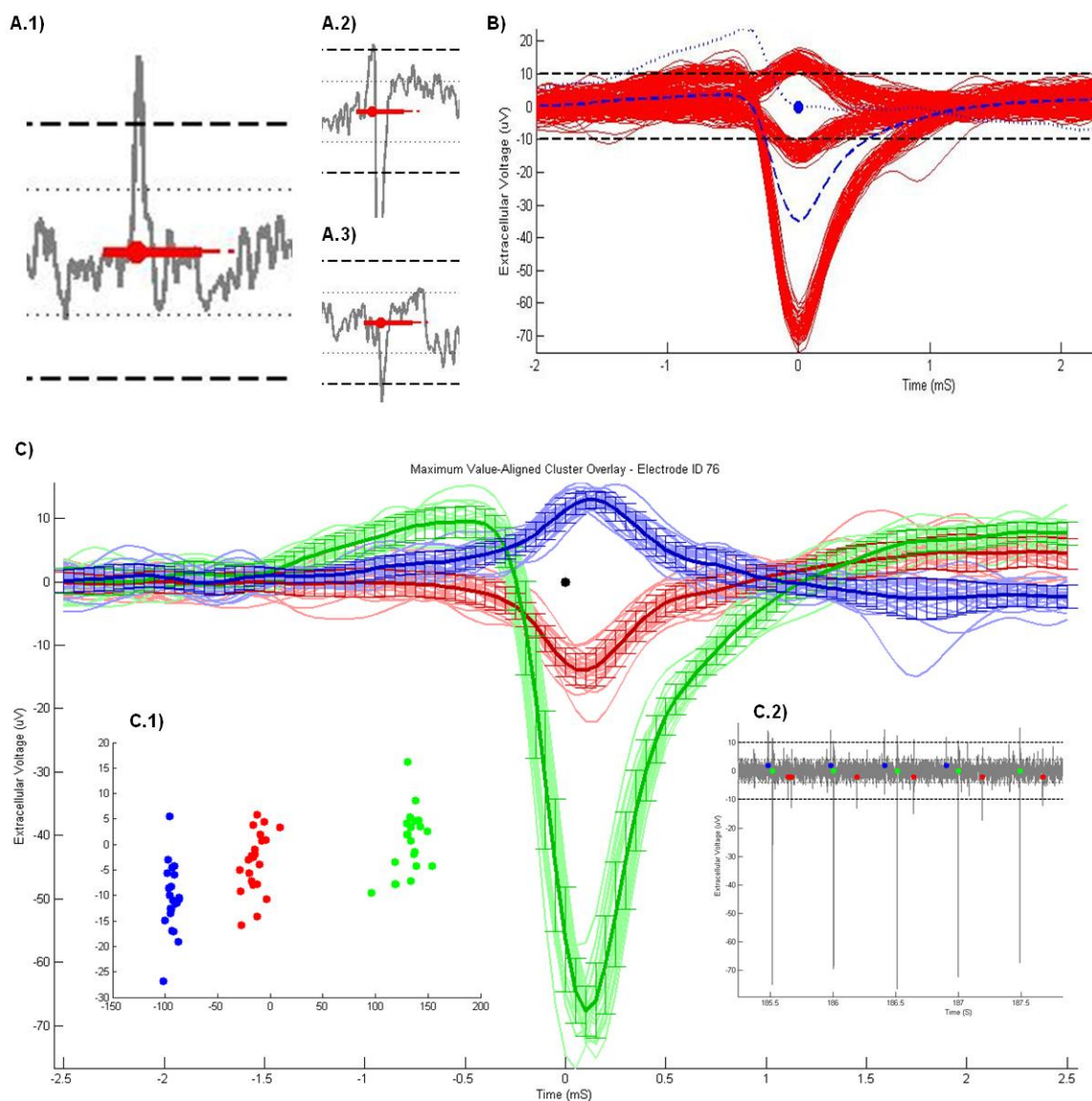


Figure 3.3-3. Spike-sorting by principal component analysis (PCA)

A) Example data (same as from Fig. 3.3-1 B), now showing the location of the placement window (bold red bar) and the blanking window (dashed red bar), relative to the point at which the EVT crosses the spike threshold (black dashed line). B) EVT spikes following alignment to their point of maximum displacement (red lines) along with the first two PCs identified by the PCA process (dashed and dotted blue lines, respectively). C) Spike assignment by clustering. C) Spikes after clustering. Each individual trace appears in the faded color, while the average of all spikes in that cluster and their standard deviation appear in darker lines. C.1) Each spike is represented by a point at a unique location in PC-space (PC1 = x-axis, PC2 = y-axis), based on its similarity to the PCs shown in panel B. Clusters identified by K-means algorithm are color coded, and correspond to the colors shown in panel C. These spikes can then be identified by location in the full EVT (C.2). This returns the information on the firing sequence of three individual neurons, even though they are all recorded on only one electrode.

2.3.4 Discussion and Results:

2.3.4.1 *Performance Tradeoffs*

Many forms of feature identification and clustering exist for use in spike sorting algorithms, and there are many permutations used by laboratories to address this problem. No “off-the-shelf” approach works across the board because of the unique aspects of every experimental system and different goals of different experimenters. As a result, many laboratories develop customized means to perform their analysis, driven by their particular situation. The huge diversity seen in myotube EVTs is the driving factor behind the development of our spike sorting algorithm. We needed a process capable of identifying completely arbitrary spike morphologies over a wider range of amplitudes and durations than is typically observed with neurons and in a variable environment. The most efficient means of doing this is a user-informed automated process in which a computer takes a try at the data, and then a user is allowed to proof the computer’s work and correct deficiencies. In the process of developing enough flexibility to account for the variability, a number of tradeoffs in performance were made, which should be considered.

In the event detection step, we use an adaptive threshold that is set automatically based on the RMS noise for the entire data segment. This allows for electrodes with different base levels of noise to be more easily included in analysis by eliminating the need to hand select a threshold level (i.e., higher thresholds are assigned to channels where there is a high noise floor). This has the added benefit of raising the threshold on channels where there is high amplitude activity, reducing the number of erroneous units that are identified from long-lasting, multiphasic muscle cell depolarizations. However, this elevation of the threshold also has the effect of reducing sensitivity to small amplitude spikes, allowing units with large amplitude to effectively silence units with small amplitude. Similarly, the user-defined blanking window has both pros and cons. A large blanking window can prevent the double identification of events where the EVT breaks the threshold twice, as can happen with exceptionally large neuronal APs or the multiphasic and large amplitude muscle cell APs. However, it also has the potential to mask events that immediately follow other events. An appropriate window should be selected based on whether the characteristics of the spikes, or their temporal relationship, is considered more important in a particular experiment.

Aligning the initially detected spikes to their point of maximum deflection is done to account for the variability in muscle cell depolarizations, which tends to be reduced in the higher amplitude regions. While this addresses the high variability in the lead and lag regions observed in muscle cell depolarizations, it creates problems based on the symmetry of some APs. APs that are equally biphasic can be split between the positive and negative peaks, effectively breaking a single biological unit into two units as detected by the algorithm. Despite this shortcoming, aligning to the maximum deflection is generally much better than aligning to break point. Ultimately, the goal of the alignment step is to reduce the irrelevant variability between spikes to allow a more

effective PCA process to occur. Once alignment has been achieved and PCA has identified the PCs, there is some debate on the number of PCs needed to appropriately cluster. Typically 2 or 3 are used, but some have found that four or more may provide better robustness against noise. Including more PC dimension in our clustering process may start to explain irrelevant variance (again, the consequence of highly variable myotube APs, particularly in the leading and lagging zones). Additionally, the problem of non-stationarity will be exacerbated by the use of superfluous PCs, as it systematically creates a region of variability in spikes known to come from a single neuron.

Either K-means or GM clustering methods perform well. GM works best in the hands of a human because the distribution of the points when non-stationarity is a problem is largely non-Gaussian [180]. Most large scale variance is caused by non-stationarity effects and causes slurring of the clusters along some manifold. Of particular note in the clustering step is the reanalysis of split clusters in their own PC space. This creates a higher definition feature space in which other clusters do not reduce the ability to distinguish more “closely” related clusters by creating a false relative proximity. This makes the process of splitting and joining clusters accurate and comparatively bias-free, as points are still always clustered based on either of the two algorithms above.

Another unique aspect of this algorithm relative to many currently in use, is the consolidation of clusters and time shifting to align them to the threshold breakpoint. Muscle cell APs can go on for over 10 μ s and can have multiple peaks and valleys, which means considerable delays are possible between the onset of an AP and the point of maximum deflection. Identifying the time stamp for an event that allows for accurate identification of event onset will facilitate the identification of an accurate firing sequence, and therefore, potentially causal relationships within a network.

2.3.5 Conclusion:

The program is successfully able to sort spikes based on the EVT morphology. A fully-automated (i.e., unsupervised) analysis of 1 min of data recorded on 60 channels requires ~ 3 hr to complete but does not require any user intervention. By hand analysis of this same data segment typically takes ~5hrs of user-intensive labor. While automated clustering is successful in ~50% of cases, the program unable to appropriately group the spikes in the more complicated channels. Therefore, by hand analysis is still generally required to correct deficiencies in the automated spike-sorting process. Once channels requiring hand sorting have been identified, the program provides enough structure to assist the user in the logical grouping of spikes but also enough flexibility to adequately guide the grouping process. Because the automated process correctly deals with ~50% of the channels, however, it reduces the time it takes to analyze these large data sets by half. Most importantly, it provides an accurate measure of spike morphology, which can be used in subsequent analysis, and also an accurate firing sequence for all identified units, which will provide appropriate input for subsequent network identification processes.

Future directions include the development of network ID algorithms so that network dynamics can be examined quantitatively in addition to examining the properties of individual units. More effective automated clustering algorithms can also be employed that will further reduce the time it takes to analyze these large data sets.

3 Tunable culture environments affect myotube and motor neuron behaviors

3.1 The effect of microscale grooves on skeletal myotube alignment and independence in a 2D culture system

3.1.1 Abstract:

The development of tissue engineering techniques capable of recapitulating features of skeletal muscle tissue has applications in both lab-on-a-chip and clinical applications. There are many tools available which have the ability to cause the development of contractile and aligned myotubes in both two and three dimensions. However, little has been done to assess the ability of these techniques to preserve the independent function of neighboring myotubes that allows for the controlled development of graded force in skeletal muscle *in situ*. This study examines the effects of microscale topographical trenches in promoting myotube alignment and studies the effect of these substrate modifications on myotube independence. We find that cell alignment is promoted by narrower microscale trenches, especially in the early stages of myoblast adhesion and spreading, but that the same degree of orientation is ultimately achieved across the full range of trench geometries. Similarly, the presence of microscale trenches resulted in the earlier onset of spontaneous contractions without altering the maximum number of spontaneously contractile myotubes ultimately achieved. Furthermore, the use of microscale trenches resulted in concentrated spontaneous contractions in the trench regions with geometry-dependent specificity. Implications of these findings on potential mechanisms regulating myotube differentiation are discussed as well as potential applications of microscale trenches for controlled myotube culture preparation.

3.1.2 Introduction:

The ability to control the formation of muscular tissue-engineered constructs holds potential in the treatment [181], diagnosis [182, 183], and study of disease processes [184, 185]. Additional applications exist in nonclinical bioengineering fields, such as biorobotics [65] and biodetection [81, 186]. One of the most unique aspects of skeletal muscle cells is the large morphological change that myoblast cultures undergo when fusing into contractile myotubes during development. As differentiation and maturation occurs, singly-nucleated myoblasts first adhere to the substrate, then align and fuse into multinucleated myotubes, and finally mature into contractile myotubes, which can be several orders of magnitude larger than their precursor myoblasts [187]. Each step of this process is instructed by each cells' genetic program, communication with neighboring cells [188], and interactions with the chemical [189], physical [190], and electrical [191, 192] extracellular environment. In skeletal myotube cultures, two basic morphologies are usually present: 1) branching multipolar and 2) spindle-shaped bipolar. Because the multipolar myotube is a single, continuous cell, it contracts as a single unit. In the case that two separate myotubes are next to each other but are not fused, they retain the ability to contract independently of one another.

Great progress has been made in the field of skeletal muscle tissue engineering, and the wide range of potential applications is reflected in the wide range of tools employed to control myotube growth [181, 193]. Most tissue engineering tools take advantage of topographical or chemical means of inducing ordered culture architecture similar to that observed *in vivo*. However, while myotube alignment is clearly important to muscle tissue's ability to efficiently develop large forces, the generation of controlled, sustainable, repeatable contractions requires the selective and coordinated activation of independently operable motor units [194, 195]. While a great deal of effort has been

placed on cataloguing our ability to encourage myotube differentiation, development, and alignment, less effort has been directed at developing ways to exert control over myotube independence [1]. Unraveling the mechanisms by which these independent motor units are produced and maintained from a nearly homogenous pool of progenitor cells is therefore an important step in muscle tissue engineering [196]. Additionally, control of myotube formation has implications in creating microscale devices or sensors based on biological elements [81]. Preserving independent control over myotubes, rather than allowing them to fuse randomly, will improve such devices by increasing the number of independent cellular signal transducers (for biosensor applications) or actuators (in biorobotics applications).

3.1.3 **Methods:**

3.1.3.1 *Substrate fabrication and characterization*

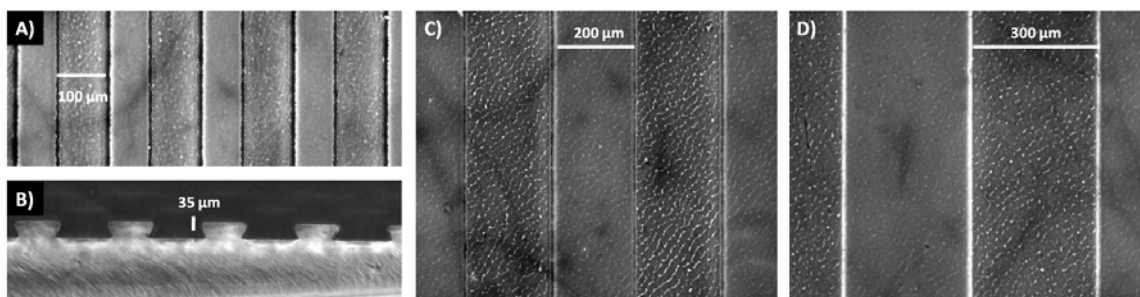


Figure 4.1-1. Characterization of PDMS Substrate

A) Top-down microscopic view of PDMS substrate with 100 μm trench width and spacing. B) Side view of substrate from A. Similar substrates with different geometries were produced using the same technique with trench spacing an width of up to 500 μm (200 μm and 300 μm shown in C and D, respectively).

PDMS monomer (Dow Corning, Sylgard 184) was mixed 10:1 with curing agent. The solution was poured over a silicon wafer, which had been coated with SU-8, into which the negative pattern of our groove geometries had been developed. After degassing under vacuum for 30 min, the PDMS was cured overnight at 37° C. The PDMS was then

peeled from the surface of the silicon SU-8 master, resulting in a positive pattern of grooves. The geometry of the grooves on the resulting substrates was characterized using bright field microscopy (Fig. 4.1-1). Sample substrates were imaged top down (Fig. 4.1-1 A), and in cross section following transaction (Fig. 4.1-1 B). The size of each feature in pixels was counted using ImageJ software (NIH, Bethesda MD)] and converted into μm using a known conversion factor specific to the microscope objective. A pattern of parallel grooves with equal pitch and width were selected for the experimental geometry so that each viewing field contained an equal quantity of groove and plateau surface area.

3.1.3.2 Myotube isolation and culture

Myoblasts were isolated and cultured as previously described [1]. Briefly, pregnant Sprague Dawley rats were sacrificed by CO_2 inhalation at gestational day 21, and pups were removed by Cesarean section. Hind limb muscles were removed, and tissue was finely minced and digested (20 min at 37°C) in PBS containing 1.5 U/ml collagenase (type D, Roche, Mannheim, Germany) and 2.5 U/ml dispase (type II, Roche, Mannheim, Germany). Single cells were separated from debris, pelleted by centrifugation, and resuspended in growth medium consisting of Ham's F-10 medium plus 20% fetal bovine serum, 1% Penicillin/Streptomycin, (all from Invitrogen, Carlsbad, CA) and 2.5 ng/ml human b-FGF (Promega Corporation, Madison, WI). Cells were then plated into 75 cm^2 flasks and incubated for 24 hrs. Adherent cells were resuspended and plated onto PDMS substrates in differentiation medium consisting of Neurobasal medium including 2% B-27 supplement, 1% Penicillin/Streptomycin, and 1% GlutaMAX (all from Invitrogen, Carlsbad, CA) at a surface density of $200,000\text{ cells/cm}^2$. Prior to seeding, surfaces were plasma treated (O_2 plasma for 120 S at 50 Watts) and adsorbed overnight with $40\text{ }\mu\text{g/ml}$

laminin (Sigma Aldrich, St. Louis, MO). Medium changes were performed every other day.

3.1.3.3 Quantification of myoblast and myotube alignment

Myoblasts were seeded onto PDMS substrates bearing either 100 μm X 100 μm , 200 μm X 200 μm , or 400 μm X 400 μm trenches (*trench width μm X separation μm*). PDMS substrates with a smooth surface were used as an unaltered control, and each surface was prepared in triplicate. Two randomly selected fields, showing 0.55 mm^2 , from each myoblast-seeded substrate were imaged using a phase contrast microscope at 12 hrs post seeding and every 24 hours after that until DIV 8. Myoblast alignment in these images was assessed using a modification of the image intensity gradient algorithm [197, 198]. Briefly, each image was broken into square tiles. The intensity gradient of each pixel in this square interrogation window in both the X direction (δ_x) and Y direction (δ_y) is calculated and then averaged across the field. An angle, θ , is then calculated based on the arctan of δ_y/δ_x , which represents the average orientation of optical density within that field. This series of operations is repeated for every square tile, and the distribution of resultant θ 's provides a measure of bulk culture alignment. Squares located on trench edges were excluded to prevent the introduction of substrate-based alignment bias.

3.1.3.4 Quantification of myotube contractility

To dynamically analyze contractile activity of myotubes, videos of cell behavior were acquired after the onset of spontaneous contractility and were analyzed as described in [1]. Briefly, videos were analyzed using a series of image processing and pattern recognition steps, which made it possible to identify regions of synchronized contractility within videos of myotube cultures. This analysis provided the number and location of the contractile myotubes. An additional step was added to this process in which the

orientation and locations of the trenches were identified in each video, allowing additional analysis examining the spatial relationship of spontaneous contractility to the trenches. Three measures relating contractility and trench location were examined. The first was the percentage of the contractile activity that is located in the trenches, calculated as the sum of all contractile area located inside of the trenches divided by the total area identified as contractile in the video. The second metric was the average number of trenches spanned by each myotube, where at least 5% of the myotube must be located in a trench in order for it to be counted. The final metric was the average number of myotubes that exist in each trench, again where at least 5% of the myotube must be located in a trench in order for it to be counted. Because there were no trenches on the smooth control surfaces, videos of myotubes on trenches were compared to smooth surfaces on which the same orientation and trench pattern had been artificially imposed. Thirty second videos of myotube behavior were acquired over 200 frames using a 10× objective and 512 × 640 pixel resolution, recording an area of 0.55 mm². Two videos for each triplicate replication of PDMS substrates bearing 100 μm, 200 μm, and 400 μm trench geometries as well as a smooth control were analyzed.

3.1.4 Results and Discussion:

3.1.4.1 Myotube morphology on PDMS substrates with microscale topographical trenches

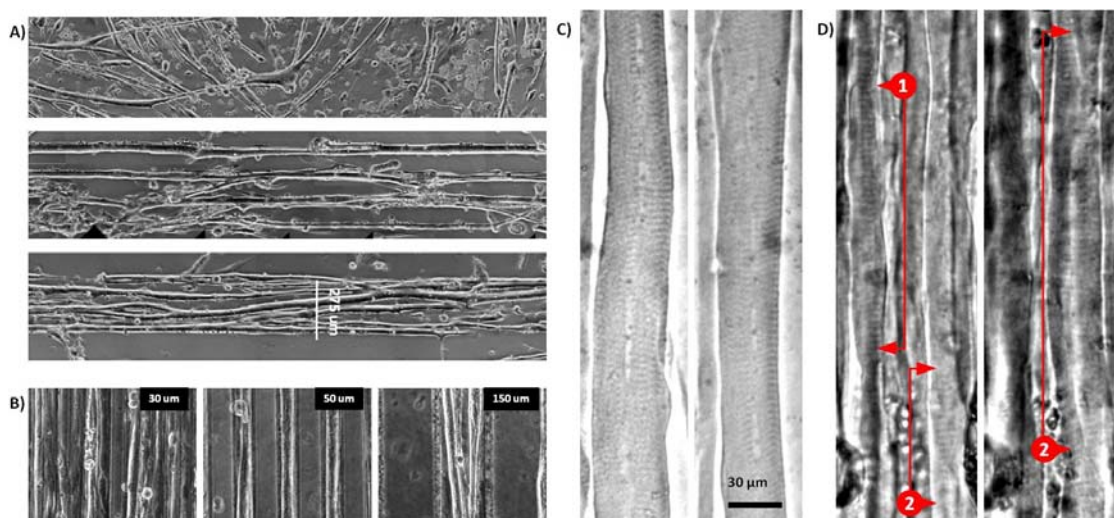


Figure 4.1-2. Myotube morphology on chemically and topographically patterned substrates

A) Myotubes at DIV 11 grown on unpatterned (top) and laminin-stripped (middle and bottom) glass. B) Myotubes at DIV 11 grown on PDMS substrates topographically modified with 30 μm grooves (left), 50 μm grooves (middle) and 150 μm grooves (right). Striations in myotubes at DIV 14 grown in the plateau region (C) and groove regions (D) of a topographically modified PDMS substrate.

Consistent with prior results, we found that both microscale chemical [184, 189, 190, 199] and topographical [54, 197, 200-202] patterning techniques were effective at directing myotube alignment (Fig. 4.1-2 A and B). Conditions affecting the rate of fusion and the final myotube morphology (shape and size) include seeding density and surface chemistry. Surfaces adsorbed with pro-fusion proteins, such as laminin, promoted myotube differentiation while those adsorbed with non-bioactive adhesion promoters, such as polyethyleneimine (PEI) or poly-D-lysine (PDL), did not (data not shown). On laminin adsorbed surfaces, myoblast fusion and maturation into striated myotubes was

robust. Myotubes in the intertrench plateau regions tended to be flattened out and non-overlapping, pushing more of the myotube into one focal plane and facilitating visualization of the striations (Fig. 4.1-2 C). Cell growth in the trench regions tended to be more three-dimensional and allowed for multi-layered growth, requiring images from serial Z-planes to show myotube striations (Fig. 4.1-2 D). While this produced local changes in cell density, each low magnification image contained a constant cell density because it contained equal portions of trench and plateau regions regardless of trench geometry, due to our selection of substrates with equal trench width and spacing.

Also consistent with previous studies [189], we found that there is an optimal width for creating patterns of physically isolated, unbranching myotubes (Fig. 4.1-2 A). For chemical patterns, it has been observed previously that as the feature size is reduced below this critical size, myotubes either connect between features or fail to adhere and mature, and as feature size is increased over the critical size, several myotubes are able to associate within each feature. Optimal trench spacing for achieving a 1:1 trench-to-myotube relationship was similar to the dimensions for chemical spacing. Fig. 4.1-2 B shows primary myocyte cultures on trench widths of 30 μm , 50 μm , and 150 μm . On 50 μm trench geometry, each feature contained a single myotube. In the larger groove geometries, multiple myotubes co-localized within the same feature, and on smaller trench geometries, myotubes were able to reach across trenches. The width of individual myotubes, however, appeared largely unchanged between these different scenarios.

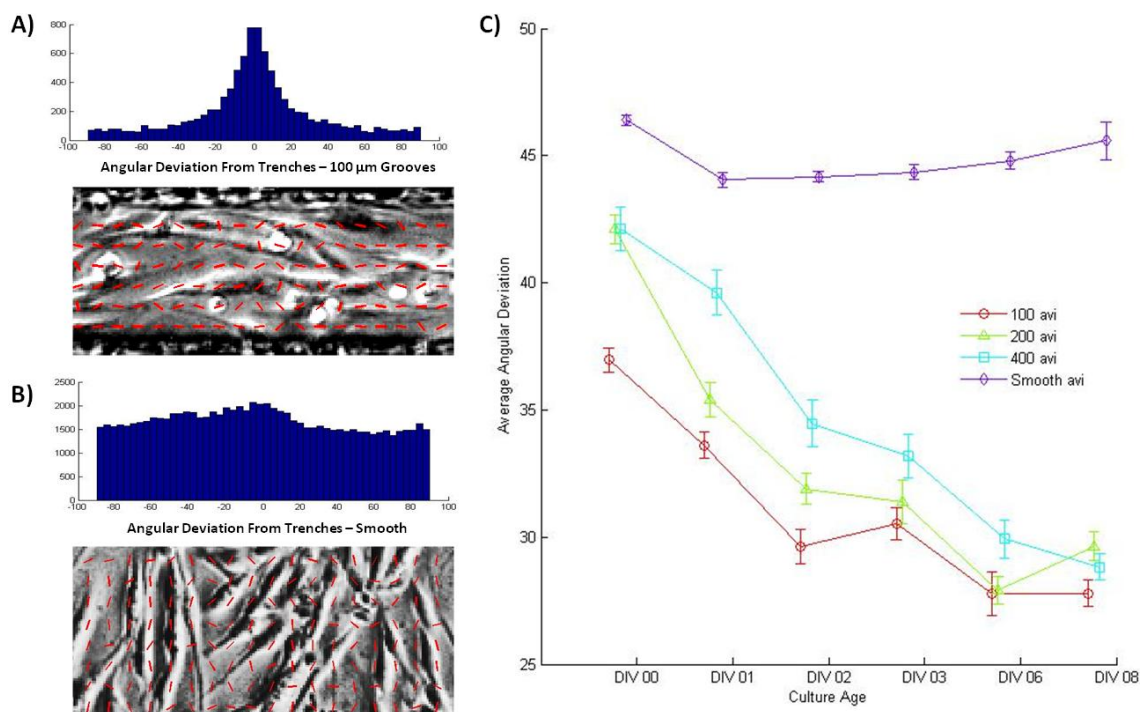


Figure 4.1-3. Myoblast alignment with major trench axis in DIV 0 – DIV 8

A) Angular deviation distribution (top) of local alignment fields detected using gradient method (example field bottom) for myoblasts on 100 μm trenches 12 hr after seeding. **B)** Angular deviation distribution (top) of local alignment fields detected using gradient method (example field bottom) for myoblasts on an unpatterned PDMS substrate. **C)** Average amplitude of angular deviation from the major trench axis for substrates with 100 μm, 200 μm, 400 μm, and unpatterned control for timepoint from 12 hr following seeding to DIV 8.

We used the optical gradient method to identify the effective angle of alignment for each square field of the microscope image based on the average X- and Y- intensity gradients of the pixels therein (Fig. 4.1-3 A and B – bottom, red bars). The orientation of each square field can then be compared to the orientation of the trenches. The distribution of orientations for the entire image relative to the primary trench direction will be highly concentrated around zero for cultures that are highly aligned with trench axis (Fig. 4.1-3 A – top) or will be flat for cultures with random growth (Fig. 4.1-3, B – top). To characterize this distribution, the average angular deviation from the trench axis can

be calculated, which will be approximately 45° in the case of random growth and will be lower in the cases of more organized growth [197, 203].

Analysis of myoblast and myotube alignment using this method showed that myotube alignment was induced by topographical guidance cues, consistent with prior studies on guidance cues of similar size. Myotube cultures seeded on PDMS substrates with trenches had an average angular deviation noticeably lower than that observed in cultures grown on smooth PDMS substrates, which was approximately equal to the 45° expected from truly random growth (Fig. 4.1-3 C).

Analysis over the timescale of DIV 0 through DIV 8, however, showed a number of additional trends in myoblast alignment and fusion into myotubes. While myotubes on all grooved substrates ultimately reach the same degree of directed orientation by DIV 8, there are transient differences between substrates bearing 100 μm , 200 μm , and 400 μm trench geometries during early time points (Fig. 4.1-3 C). Alignment of myoblasts, even before they have begun to fuse into myotubes, occurs sooner on the narrower trench geometries, as exhibited by the alignment of unfused myoblasts as early as 12 hours after seeding on 100 μm trenches (Fig. 4.1-3 A) relative to an unpatterned control (Fig. 4.1-3 B).

3.1.4.2 Myotube contractility on PDMS substrates with microscale topographical trenches

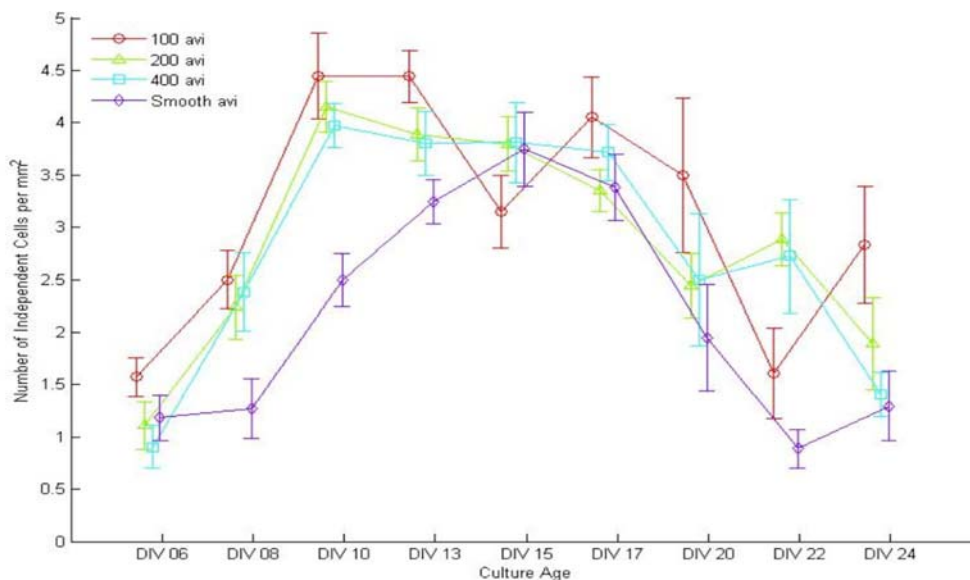


Figure 4.1-4. The number of independently active cells per unit surface area in grooved and smooth myotube cultures as a function of culture age

Spontaneous contractility is observed in many myotube culture systems. With the recent development of an algorithm for quantifying myotube association based on videos of spontaneous contractility [1], we are now able to look at the effects of topographical guidance cues on this measure of myotube function in addition to simple morphological examination. Figure 4.1-4 shows the number of independent spontaneously active myotubes identified in cultures on smooth and patterned PDMS from DIV 6 – 24. Consistent with qualitative observations in the literature, myotubes in culture underwent an early period of maturation during which spontaneous activity increased as myotubes fused and matured, followed by a gradual decrease in activity [197]. The exact time course of these events is a product of factors specific to each culture system, ranging from medium composition, cell source, cell density, and various characteristics of the

extracellular environment. In our culture system, spontaneous twitches have been observed as early as DIV 5 and can continue through 3 weeks in culture. When this spontaneous activity is quantified, we see a similar trend as is observed in the myotube alignment data. While myotube cultures on grooved substrates exhibited a greater number of spontaneously contractile cells during early time points (i.e., DIV 8 – 13), the myotube cultures on smooth substrates ultimately caught up to them and produced similar quantities of spontaneously contractile cells (i.e., DIV 15 – 17).

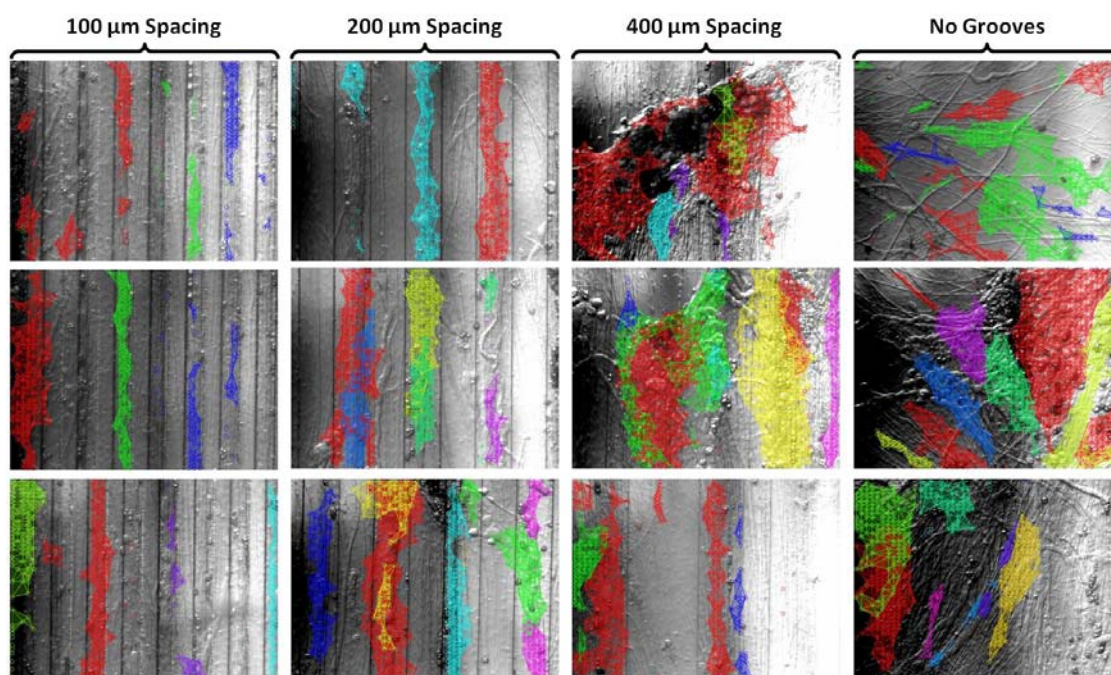


Figure 4.1-5. VTA-Identified regions of contractility on grooved PDMS substrates with 100 μm – 400 μm trench geometries and unpatterned control

The contraction identification algorithm also shows the physical location of contractile myotubes. This analysis shows trends in the spatial distribution of contractile activity that is dependent on trench geometry. Figure 4.1-5 shows example behaviors of myotubes on patterned and smooth PMDS substrates. Qualitatively, myotube

contractility appears to be directed to, aligned with, and confined largely within the trenches. The highest degree of order is achieved at 100 μm , with disorder increasing as the length of uninterrupted trench width increases. On the 100 μm trench geometry, myobutes aligned along the trench axis, and typically, there was only 1 myotube per trench. When the trenches were this close together, however, it was possible for one myotube to bridge multiple trenches. On the 200 μm trench geometry, contractility was still largely directed to the trenches, but it became possible for multiple myotubes to be active in a single trench. On 400 μm trench geometry, myotubes increasingly spilled out of the trenches, there was an increase in overlapping activity, and there was diminished alignment and elongation of contractile areas within the trenches. Finally, on smooth substrates, there was no order to the myotube activity, and myotube contractility was distributed in random locations and with random orientations.

3.1.4.3 Myotube contractility selectively guided to trenches

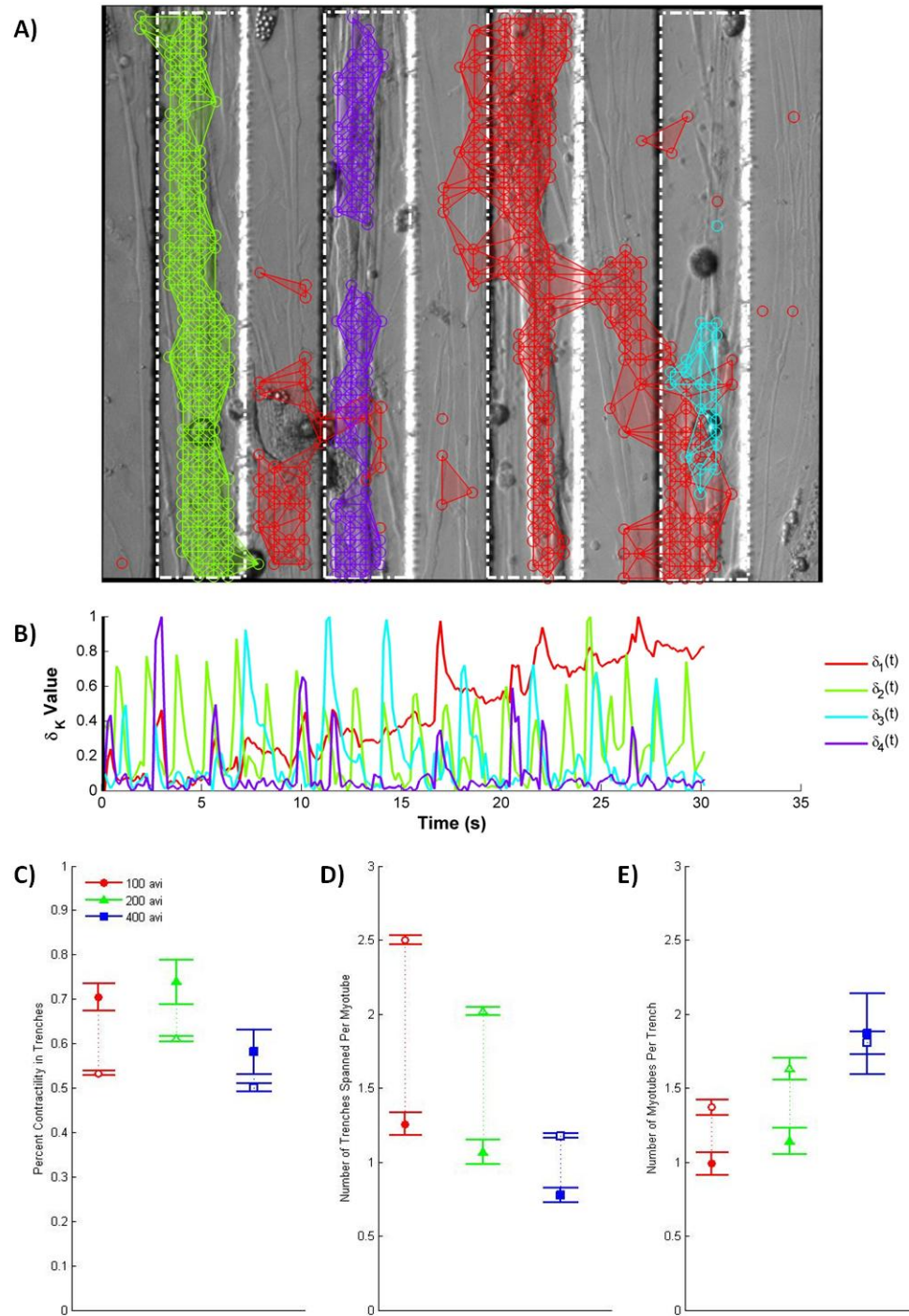


Figure 4.1-6. Myotube contractility spatial relationship with trenches

A) Example image of contractile myotubes at DIV8 on 100 μm groove spacing. **B)** Activity pattern of myotubes

indicated in A. Percentage of total contractile area located in trenches for (C), the average number of trenches spanned by each myotube (D), and the average number of myotubes found in each trench (E), is quantified for 100 μm , 200 μm , and 400 μm trench geometries (filled points) relative to unpatterned control for each case (empty points). Error bars represent the standard error of the mean.

By superimposing a map of contractile activity on the location of trenches (Fig. 4.1-6 A) for each video, it is possible to quantify the relationships between contractility distribution and trench location that are qualitatively shown in Figure 4.1-5. Because it is possible that trench distribution itself may create a sorting effect, each video of myotube behavior on patterned substrates was compared to videos of unpatterned cultures on which the trench pattern from the video being analyzed has been superimposed. For some of the metrics examined, there was a slight trend, suggesting a dependence on trench spacing. However, a much greater effect was clearly present between each patterned substrate and its unpatterned control.

Figure 4.1-6 C confirms the observation that contractile activity is directed largely to the trenches. In each of the trench geometries, substantially more of the contractile activity appeared in a trench region compared to the smooth control surfaces. Because trench spacing and width are equal in all geometries, 50% of the surface shown in each video is trench and 50% is the intertrench plateau region. This means that in the case where myotube activity is randomly distributed, we would expect to find ~50% in the trenches, which is approximately the case in our experimental system.

Not only is contractile activity directed generally to the trenches, but trench location correlated with contractile activity with some degree of specificity depending on trench geometry. For example, in the 100 μm trench geometry, a single trench typically only contained a single myotube, while many myotubes were able to span multiple trenches. By comparison, in the larger trench geometries, the wider trenches were more likely to

contain multiple myotubes while it is more difficult for single myotubes to span the larger distance between trenches. This observation is reflected in Figure 4.1-6 D and E, where the closely spaced and narrow trenches of the 100 μm case resulted in a larger number of trenches spanned per myotube, and a lower number of myotubes found in each trench, as compared to the other patterns. More important than a comparison between trench geometries, however, is the clear difference between each geometry and the unpatterned controls. Relative to these unpatterned controls, myotube formation is directed to the trenches in a selective manner that preserves functional independence of myotubes from those in neighboring trenches.

3.1.5 Conclusions:

In this study, we have investigated the effects of microscale topographical patterns in the form of parallel stripes on the development of structured myotube cultures, using myotube alignment, and for the first time, a measure of functional myotube independence as endpoints. Many different substrates have been used to drive myotube alignment [181, 193]. However, in many of these techniques, myotubes show a “dose-insensitivity” effect, in which myoblast response to a graded range of alignment cues tends to be essentially binary (i.e., cells are either highly aligned or completely random) rather than exhibiting a graded alignment response [191, 200, 204, 205]. This is consistent with our findings that there is little difference between the ultimate amount of alignment observed between trench widths over the range of trench geometries examined.

Additionally, we found that changes in myotube behavior in response to microscale trenches are largely a product of early events in myoblast spreading and alignment. Myotube alignment increases through DIV 8, but a large and substrate geometry-dependent difference in cell alignment on patterned and unpatterned substrates was

observed as early as 12 hours following seeding. This was likely because in the early stages of myoblast attachment, cell spreading was partially guided by the grooves. The effect was most notable in the narrower trench geometries because these features have spatial dimensions on the same order of magnitude as the myoblasts themselves. Because myoblasts are polarized cells, which are spindle shaped, this head start in alignment most likely reduces the amount of time they need to spend migrating under their own power to achieve the end-to-end alignment thought to be required for fusion and differentiation into myotubes.

While the effects of microscale topographical trenches on myotube alignment are relatively straightforward, their effect on myotube independence is more complicated. Based on the static images that the morphological studies are based on, it would have appeared that guidance cue geometries above or below a critical size resulted in communication between myotubes within the same feature or between features, respectively. In our own chemical and topographical patterning work, as well as that of others groups, this was visualized as branching myotubes. From these morphological studies, it follows logically that only myotubes located in separate grooves are electrically isolated from one another and would therefore twitch independently. However, based on studies of spontaneous myotube contractility, it now appears that myotubes are capable of maintaining independence from neighboring cells even when they overlap extensively. This is supported by our observation that the use of microscale topographical guidance cues resulted in earlier alignment and onset of spontaneous activity but did not increase the final number of independent cells. These observations support a conceptual model where myoblast fusion and differentiation is primarily controlled by intrinsic factors rather than the extrinsic factors delivered by the static mechanical cues found in the extracellular environment of the synthetic microscale

trenches [196, 206]. While the small boost in myoblast alignment provided by the microscale trenches is sufficient to give the fusion/maturation process a head start, it does not alter myotube cellular physiology, and therefore, the functional endpoint reached is ultimately the same.

While microscale topographical features do not have any effect on cellular independence, they can serve the useful purpose of controlling culture mechanics. Microscale grooves can be used not only to drive culture-level myotube alignment but also to direct contractile activity to specific regions and encourage contraction in specific directions. Microscale patterning techniques may be used to generate controlled anisotropy, as exists in native tissue architecture, and to direct formation of myotubes to specific locations, as would be required by microdevices incorporating an engineered skeletal muscle component.

This study depended on the spontaneous activity of rat myotubes in culture to show myotube independence. Future studies will involve the integration of this myotube guidance technique with multi-modality bio-MEMS devices with substrate embedded electrodes for the purpose of recording bioelectrical activity or selectively triggering contraction of myotubes located in specific regions. Developing such biointerfaces for tissue engineered skeletal muscle constructs may improve the performance of skeletal myotube-integrated lab-on-a-chip or biorobotic devices by increasing their degrees of freedom for actuation or detection. Additionally, such an idea may be clinically useful within the context of a microscale adaptation of the targeted muscle reinnervation (TMR) technique, which uses surface EMG to control prosthetic devices in amputees [53]. Making signal acquisition a process that occurs on the scale of single muscle fibers detected with microscale implantable electrodes, rather than course surface electrodes,

may increase the number of independent signals that can be recorded, thereby increasing the bandwidth for communication with the user.

3.2 Spatially selective detection of extracellular action potentials and neurite outgrowth in spinal cord explant culture vs. dissociated neuronal culture

3.2.1 Abstract:

Ultimately, our goal is to develop a culture system able to sustain structured co-cultures of myotubes and neural tissue. The objective of such a system is to observe the activation of myotube populations by neuronal sources that have innervated them *in vitro*, thereby creating a lab-on-a-chip tool for studying myotube-neuron interactions and the formation and maintenance of the neuromuscular junction. Meeting this objective requires that myotubes and neurons be grown in such proximity that physical contact through axonal outgrowth from the neuronal source is possible, but confined so that the extracellular action potential (EAP) from each cell type can be recorded separately. Neuronal culture is possible in a variety of ways, from highly disorganized dissociated culture to highly organized organotypic preparations. Here we examine the feasibility of using spinal cord explant cultures, similar to slice preparations, as a means of geographically confining the neuronal cell bodies while preserving the ability of neuronal cells to access distant targets through axonal outgrowth. EAP localization was determined using commercially available substrate-embedded multielectrode arrays (MEAs), and axonal outgrowth was determined using immunohistochemical staining techniques. We find that explant cultures preserve neuronal function while successfully confining cell bodies (and therefore EAPs) to a precise location and exhibit the aggressive axonal outgrowth required for our application. Additionally, guidance of

axonal outgrowth from explants is possible using either chemical or topographical guidance cues.

3.2.2 Introduction:

Neurons can be cultured using a number of techniques, each preserving different degrees of physiological relevance and enabling different degrees of control over experimental conditions. At one extreme is dissociated culture, typically produced by triturating embryonic central nervous system (CNS) tissue into a cell suspension where each cell is separated from its neighbors before being randomly recombined on a growth substrate. These cultures contain multiple cell types intermixed without regard to their relationship *in vivo*. From this starting point, it is possible to induce some degree of order through selective elimination of certain cell types, as in cytosine arabinoside (AraC) treatment to eliminate cell types other than neuros, giving some control over cellular composition of the culture [207]. Additional order can be imposed through spatial patterning of cells using topographical [208] or chemical [59] cues, thereby effecting the ability of the cells to make contact with neighboring cells. With the obvious relevance this has to studies of neural dynamics, such techniques have become increasingly popular in neuroscience and have been facilitated by the explosion in microfluidic techniques for producing structured cell culture environments [209-211]. At the other extreme is the organotypic culture of neural tissue from more mature animals. Performed as acute or chronic experiments, slices of neural tissue can be isolated to preserve the patterns of synaptic connectivity within those slices [212].

Within the scope of our project, preserving native tissue architecture is likely to be important for several reasons. Motor neurons and myotubes have been observed to interact in dissociated culture [56, 88, 213], but formation of mature NMJs is thought to be a process involving multiple cell types [187, 214-216]. In particular, synaptic pruning

at the NMJ may be dependent on the use of organotypic preparations rather than dissociated culture [217, 218]. Additionally, we are spatially constrained by the need to have myotubes and neurons close enough to make contact through axonal extension yet far enough away that their EAPs do not overlap significantly.

In this series of experiments, we examined the spatial electrophysiological characteristics of dissociated neuronal culture and spinal cord explant culture. The implications of our findings to the suitability of each culture type is discussed, and it is determined that explants provide the most advantageous behavioral characteristics.

3.2.3 Methods:

3.2.3.1 *Isolation and culture of spinal cord explants and dissociated neurons*

Spinal cord explants are prepared using procedures based on [219]. Briefly, pregnant Sprague Dawley rats were sacrificed by CO₂ inhalation at gestational day 15, and pups were removed by Cesarean section. Spinal cord was removed posteriorly and transferred to a PDMS- lined petri dish in a drop of medium. The cord is then bisected longitudinally and finely minced transversely into sections 200 – 300 µm thick. Sections were suspended in NB medium plus 1% GlutaMAX supplement and 2% B27 supplement. Explants were then plated onto chemically or topographically patterned glass substrates or MEAs, all of which had been adsorbed overnight with laminin at 40 µg/ml in 10 µL of medium. Explants can be precisely positioned on the growth substrate during this step. In this experiment, explants were positioned with the explant body over three contacts in the top row of the MEA, allowing space for axonal outgrowth over the other contacts. After 5 min, allowing for initial adhesion, enough medium was added to just cover the explant, and it was placed in an incubator at 5% CO₂ and 37 deg C. Medium was replaced every 2 days.

Because spontaneous EAP activity and culture survivability was low in dissociated spinal cord cultures, cortical neurons were used as a proxy to determine spatial distribution of EAPs in dissociated neuronal culture. Cortical neurons were isolated as previously described [139]. Briefly, pregnant Sprague Dawley rats were sacrificed by CO₂ inhalation at gestational day 18, and pups were removed by Cesarean section. Cortex was isolated, meninges were removed, and a single-cell suspension was prepared by triturating the cortex with a flame-polished glass pipette. Cortical cells were then seeded onto MEAs in MEM medium plus 1% penicillin/streptomycin, 10% horse serum, and 3% v/v of 20% glucose solution at a surface density of 225,000 cells/cm². Prior to use, the medium was glutamate depleted by 24 hr exposure to astrocytes in culture, and the MEA surface was treated overnight with 3% PEI dissolved in borate buffer.

3.2.3.2 Immunostaining

Explants were fixed and stained on DIV 13 to identify axonal and dendritic outgrowth. Explants were fixed in a PBS plus 4% PFA and 4% sucrose solution for 15 min at room temperature. After washing 3 times in PBS, explants were then permeabilized and blocked for 1 hr at room temperature in PBS plus 2% FBS, 0.2% Triton, and 0.02% sodium azide. Explants were rinsed 3 times with PBS, and incubated in primary antibody solution for 2 hr at room temperature (1:500 mouse anti-Tau and 1:200 rabbit anti-MAP2). Primary antibody solution was removed, and explants were washed 3 times with PBS before incubation in secondary antibody solution for 1 hr at room temperature (1:300 donkey Cy2-conjugated anti-mouse and 1:300 goat Cy3-conjugated anti-rabbit). Secondary antibody was removed, and explants were washed 3 times with PBS before imaging using an epifluorescent microscope. Five well-attached explants were imaged

in each condition, and their outgrowth was quantified using ImageJ software (NIH, Bethesda MD).

3.2.3.3 Chemical patterning

Laminin patterns were produced using a technique called microscale plasma-initiated patterning [220]. Briefly, PDMS stamps bearing the negative of the desired pattern were created using standard soft lithography techniques. These stamps were then brought into contact with glass coverslips. Surfaces where the PDMS makes contact with the glass were sealed with dry surface tension. The stamps were left in contact with the glass coverslips while they were exposed to 120 seconds of O₂ plasma treatment at a power of 50 W. During this time, the plasma makes contact with the glass everywhere except for the regions obscured by the PDMS stamp. The O₂ plasma alters the glass surface chemistry, making it more hydrophilic in these exposed regions. After treatment, the stamps were removed, and a solution of 40 µg/ml laminin was added to the glass coverslip. The differential surface hydrophilicity resulting from the plasma exposure is sufficient to drive laminin deposition selectively on the plasma-treated regions, generating a surface pattern of laminin adsorbed from the solution.

3.2.3.4 Topographical patterning

Topographical patterns were created on 1 mm thick glass slides in SU-8 2025 photoresist (PR) using standard photolithography processes. Briefly, glass substrates were cleaned with sequential 10 min washes in acetone, isopropanol, and DI water, and dehydrated in a convection oven for 30 min at 130 °C. PR was spin-coated onto the glass substrate to a depth of 40 µm. The chips were softbaked for 1 hr at 45 °C, at which point the temperature was cycled twice from 95 °C to 45 °C for 10 min each before being held at 95 °C for 2 hr and slowly cooled to 25 °C. Photoresist was then exposed to 5 cycles of UV light at a dosage of 45 mJ/cm² through a transparency mask bearing the

topographical pattern. Post-exposure bake consisted of a slow ramp to 95 °C for 30 min, followed by a slow cool to room temperature. The pattern was developed in SU-8 developer followed by a quick rinse in acetone, and chips were completed by hard baking them for 1 hr at 150 °C. All heating steps were performed on a programmable hot-plate unless otherwise stated. A pattern of open-ended parallel grooves was used.

3.2.3.5 MEA recording and data analysis

Recordings of spontaneous cellular activity were made on a heat-controlled stage at 37 °C in room atmosphere using a standard MCS recording array, sampling extracellular voltage from 60 contact pads at 20,000 Hz. In dissociated neuronal culture, contact pad spacing was 200 µm and diameter was 10 µm. For recording from explants, more spatial specificity was achieved by using an MEA with contact pad spacing of 100 µm and diameter of 10 µm. Recordings of dissociated cultures have been made from DIV 14 to DIV 35. Results from a 2 min section of data recorded on DIV 21, by which point spontaneous activity has fully developed, are shown. Recordings from explant culture were collected from DIV 7 to DIV 21. Data are shown from DIV 7 to emphasize how rapidly spontaneous activity appears in explant culture.

Individual EAPs were identified in the extracellular voltage trace (EVT) recorded on each electrode using a thresholding algorithm. The threshold was set by hand for each channel to account for the different levels of background noise. While the time of each EAP was recorded, PCA-based spike sorting was not performed because we are primarily interested in the location of each spike in the 8X8 electrode grid rather than in its biological origin. The relative activity recorded by each electrode contact is calculated as the total number of spikes recorded on that electrode. This information is displayed as a scaled heat map for each culture type (Fig. 4.1-1 C and F) in which each square

represents an electrode's position in the 8X8 grid, and its color encodes its activity level (hot colors indicate higher activity).

3.2.4 Results and Discussion:

3.2.4.1 Spatial localization of EAPs in dissociated cortical vs. spinal explant culture

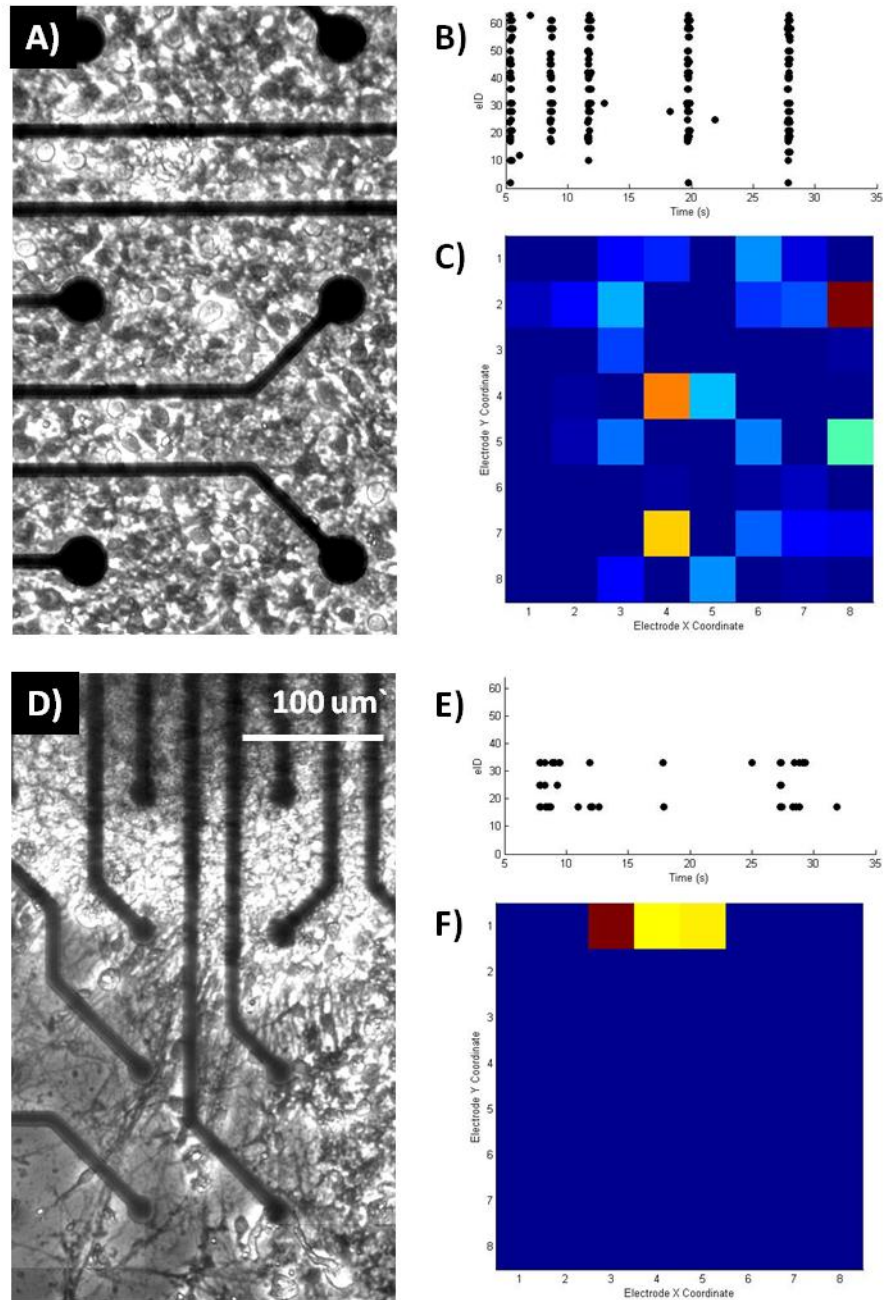


Figure 4.2-1. EAP Spatial distribution in dissociated cortical culture vs. spinal

cord explant culture

A) Dissociated cortical neurons @ 225,000 cells/cm² on an MEA (contact spacing = 200 μ m). B) Raster plot showing 30 s of activity of culture in A at DIV 21. C) Spatial distribution of activity shown in B. D) Spinal cord explant culture in which the explant has been positioned such that cell bodies overlie three electrodes in the top row of an MEA (contact spacing = 100 μ m), and axonal outgrowth extends over the rest of the contacts. E) Raster plot showing 30 s of activity of culture in D. F) Spatial distribution of activity shown in E.

There is an obvious morphological difference between dissociated cultures and explant cultures. In dissociated culture, both neuronal cell bodies and neuritic extensions are evenly and randomly distributed over entire recording surface (Fig. 4.2-1 A), while in explant culture the neuronal cell bodies and neuritic outgrowth overlie separate recording sites (Fig. 4.2-1 D). Both culture types exhibit primarily bursting activity, in which spike trains of closely spaced EAPs are generated on several electrodes simultaneously (Fig. 4.2-1 B and E). The periodicity, duration, and intensity of these spike trains are highly variable, even within the same culture, making quantitative comparisons difficult. However, spontaneous bursting activity appears noticeably sooner in explant culture (as early as DIV 7) as compared to dissociated cultures, which typically begin showing spontaneous activity around DIV 14. This difference is likely caused by the neurons in the explant body being much more closely associated with one another and their respective support cells than is the case in dissociated culture.

Within the context of structured co-cultures, the most important difference between the two culture systems is apparent in the spatial distribution of EAP activity. Dissociated culture shows activity at a variety of locations randomly spread over the recording surface (Fig. 4.2-1 C). This is because cell bodies are located near each recording site and are capable of synaptic communication with essentially any other cell

in culture. As a result, any two electrodes may be a part of a network. In comparison, explant EAP detection is limited to those electrodes directly underneath the explant body (Fig. 4.2-1 F). While the neuronal signals generated by these neurons are certainly transmitted along the axonal outgrowth, they do not produce a large enough EAP to be detected using planar electrode arrays. As a consequence, EAP detection is limited to a single, highly localized area associated with the explant body.

3.2.4.2 Axonal and dendritic outgrowth from spinal cord explants

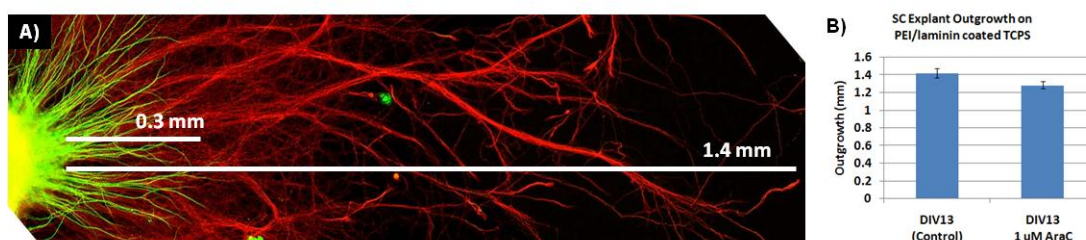


Figure 4.2-2. SC Explant Morphology and Outgrowth

A) SC explant isolated from E15 rat embryo. Explants were fixed on DIV 8, and stained with antibodies to MAP2 (green) and Tau46 (red). B) Average distance of maximum axonal extension from explant body in standard NB medium and NB containing 1 μ M Ara-C. Error bars represent standard error of the mean.

Although the neuritic outgrowth from the spinal cord explant does not generate detectable EAPs, it is important to determine their axonal or dendritic identity in order to confirm whether these processes are likely to conduct information to distant targets and to estimate how distant these targets can be while still hoping to make synaptic contact. Following staining for axonal and dendritic markers (Fig. 4.2-2 A), we observe that the vast majority of outgrowth is axonal, and these axons fasciculate in similar fashion to their behavior *in situ*. This ordered and semi-directed outgrowth is not observable in dissociated cultures, where axons from individual cells tend to grow independently. Furthermore, the extent of axonal projection was far greater than that observed for

dissociated neuronal culture with an average of 1.4 mm maximum axonal outgrowth (Fig. 4.2-2 B).

As the intended use of the explants will be in co-cultures of primary cells, it may be necessary to use Ara-C to knock down the number of contaminating fibroblasts or other proliferative cell types, thereby enriching for post-mitotic neurons and myotubes. As such, axonal outgrowth length was quantified in both the presence and absence of 1 μ M Ara-C, which was added to the medium. After 13 days in culture the presence of Ara-C in the medium did not appreciably reduce axonal outgrowth (Fig. 4.2-2 B).

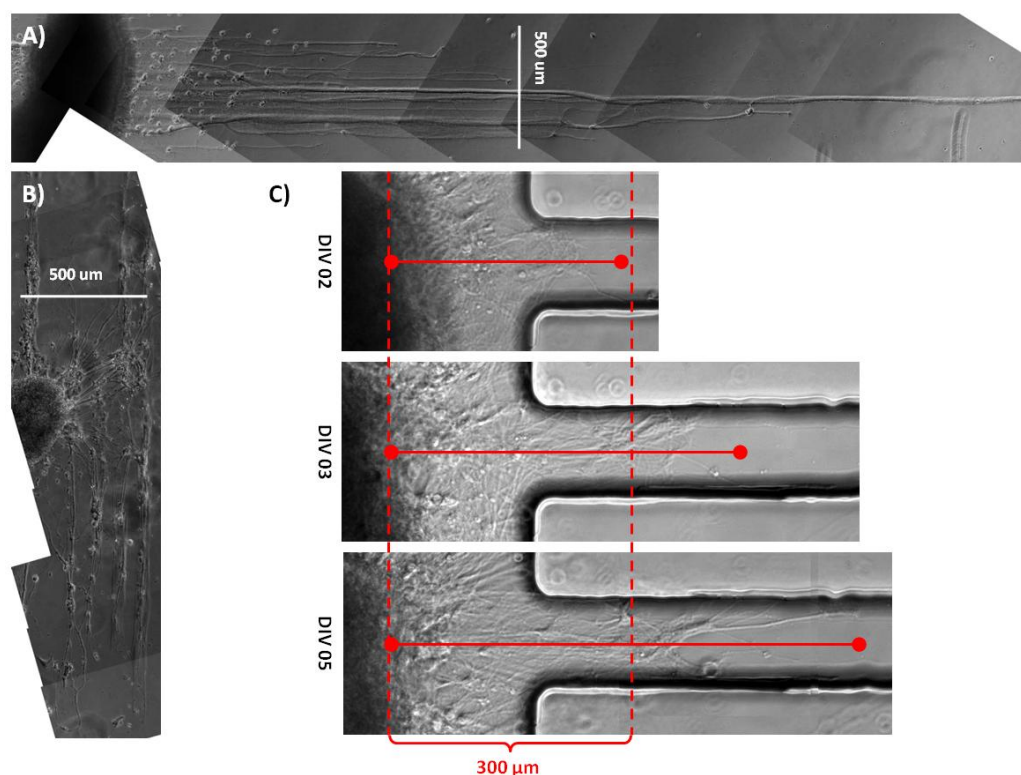


Figure 4.2-3. Topographical and chemical guidance of explant outgrowth

A) Hippocampal explant at DIV12 interacting with laminin stripes deposited on a PEI-coated glass coverslip using a microfluidics/evaporation based technique. B) Spinal cord explant culture at DIV 11 grown on laminin stripes in NB. Laminin stripes prepared using a combined microfluidic/evaporation procedure rather than the traditional u-PIP plasma-based procedure. C) Explant outgrowth on topographically patterned substrate.

Chemical or topographical cues will be required to create structured co-cultures, so the feasibility of both techniques in directing axonal extension was examined qualitatively. Chemical cues are able to guide the direction of axonal outgrowth. However, axons are able to cross the space between the patterned lines, especially in the region close to the explant (Fig. 4.2-3 A and B). Topographical cues are also able to guide neurite outgrowth and show less crossing between lanes than was present on the chemical patterns, likely because the large physical obstruction represents a greater barrier to growth (Fig. 4.2-3 C).

3.2.5 Conclusions:

Our specific aims require a culture system with the potential for physical contact between motor neuron and muscle cell pools in combination with sufficient separation to enable independent EAP recording from both. Both of these requirements are satisfied by explant cultures, which offer spatial EAP specificity and aggressive axonal outgrowth. Additionally, the earlier onset of spontaneous activity implies more rapid maturation and may shorten the amount of time required to establish functional contact between the explant and targets. Finally, the explant system preserves tissue-relevant cellular connectivity in the explant body. Because this may be important in NMJ formation, it is an important feature to preserve in culture systems in trying to recreate physiologically relevant motor neuron-myotube communication.

The information gained from these experiments has resulted in a number of important design decisions for our culture system. Both chemical and topographical patterning techniques are successful in guiding axonal outgrowth from explant cultures. However, going forward, we will employ topographical patterning in our device design. Chemical patterning involves repeated physical interaction with the surface that can damage other

features already deposited, and it only works with select agents. In comparison, topographical patterns provide a more flexible technology platform because patterns can be built permanently into the substrate and then adsorbed with pro-adhesion or pro-differentiation cues secondarily, as was the case with our topographical substrates. Finally, axonal outgrowth of up to 1.4 mm away from the explant body can be reasonably expected. This measurement provides an indicator of the physical separation possible between myotubes and neurons that can be bridged by axonal growth.

4 Myo-MEA design considerations

4.1 Skeletal myotube integration with planar microelectrode arrays *in vitro* for spatially selective recording and stimulation: A comparison of neuronal and myotube extracellular action potentials

4.1.1 Abstract:

Multielectrode array (MEA) technology holds tremendous potential in the fields of biodetection, lab-on-a-chip applications, and tissue engineering by facilitating non-invasive electrical interaction with cells *in vitro*. To date, significant efforts at integrating the cellular component with this detection technology have worked exclusively with neurons or cardiac myocytes. We investigate the feasibility of using MEAs to record from skeletal myotubes derived from primary myoblasts as a way of introducing a third electrogenic cell type and expanding the potential end-applications for MEA-based biosensors. We find that the extracellular action potentials (EAPs), frequently called “spikes,” produced by spontaneously contractile myotubes have similar amplitudes to neuronal EAPs. Similarly, it is possible to classify myotube EAPs by biological signal source using a shape-based spike sorting process similar to that used to analyze neural spike trains. While the within-unit variability is low for myotube EAPs, indicating successful spike-sorting, the among-unit variability is very high. Additionally, myotube activity can cause simultaneous activation of multiple electrodes, in a similar fashion to the activation of electrodes by networks of neurons. The existence of multiple electrode activation patterns indicates the presence of several large, independent myotubes. The ability to identify these patterns suggests that MEAs may provide an electrophysiological basis for examining the process by which myotube independence is maintained, despite rapid myoblast fusion during differentiation. Finally, it is possible to use the underlying

electrodes to selectively stimulate individual myotubes without stimulating others nearby. Potential uses of skeletal myotubes grown on MEA substrates in lab-on-a-chip applications, tissue engineering, co-cultures with motor neurons, and neural interfaces are discussed.

4.1.2 Introduction:

Future generations of biomedical devices rely increasingly on the integration of a cellular component for sensing or actuation. In such hybrid biosensors, living cells convert some stimulus into a signal that is measured by a secondary sensor, taking advantage of highly sensitive and selective sensing mechanisms and signal amplification cascades that have been honed by evolution [81]. These new hybrid sensors are increasingly used in lab-on-a-chip applications, where they allow scientists to study the behavior of individual cell types to environmental or experimental stimuli as well as the behavior of multiple cells or cell types acting in concert [81, 186, 221]. Successful operation of cell-based biosensors depends on the integration of a cell type that responds to the stimuli of interest with an appropriate secondary detection method [68, 222-224]. Having access to a wide range of cell types available for the limited number of non-invasive secondary sensing modalities will significantly expand the capabilities of hybrid biosensors [81, 222].

Substrate embedded MEAs are a particularly convenient tool for this application because they are capable of noninvasive and selective stimulation and recording. Because they detect local changes in voltage at their contact sites, however, they are most effectively used with electrogenic cell types that generate rapidly changing bioelectric potentials. Much of the work done to date interfacing MEAs with cells *in vitro* has been done with applications in two cell systems [81, 186]: 1) neurons, where the ability to identify the activity of single cells in spike trains through a process called “spike-

sorting” is used to identify patterns of population activity and network dynamics and 2) cardiac myocytes, where spatial and temporal resolution allow the measurement of transduction velocity through sheets of linked cardiomyocytes.

Here we demonstrate the feasibility of integrating a third cell type, skeletal muscle cells, with MEAs *in vitro* for recording their bioelectric activity and optically detecting their contractions. Skeletal myotubes are formed by the selective fusion of precursor myoblasts during a process which results in multiple independently active cells with complex and overlapping morphologies [188]. The process is well documented but is primarily studied using morphological, biochemical, and kinetic measurements of contractile force [1]. The temporal flexibility and spatial specificity of MEA technologies, however, are ideal for non-invasively probing cellular behavior during myoblast fusion and differentiation into mature myotubes. While myotubes have been shown to develop on an MEA surface using C2C12 cells [189], very little has been done to quantitatively examine the EAPs of myotubes that have been similarly differentiated from myoblasts *in vitro*. In this feasibility study, myotube EAPs are quantitatively compared to EAPs from cortical neurons *in vitro* in order to provide a performance benchmark.

Availability of skeletal myotubes for lab-on-a-chip applications opens another door in the development of high-throughput screening technologies, provides an improved test-bed for research into neuromuscular disorders [183], and may have implications in skeletal muscle tissue engineering, where the selective activation of fibers is required for controlled muscle construct contraction [65, 197]. Taken a step farther, it opens the door for co-culture of myotubes and additional cell types, such as motor neurons, which would allow investigators to look into the complexities of nerve-muscle interactions [225], or the formation of neural circuits like the spinal reflex arc [189, 224], with a new degree of clarity.

4.1.3 Methods:

4.1.3.1 *Myotube and neuronal isolation and culture*

Myoblasts were isolated and cultured as previously described [1]. Briefly, pregnant Sprague Dawley rats were sacrificed by CO₂ inhalation at gestational day 21 and pups were removed by Cesarean section. Hind limb muscles were removed, and tissue was finely minced and digested (20 min at 37° C) in PBS containing 1.5 U/ml collagenase (type D, Roche, Mannheim, Germany) and 2.5 U/ml dispase (type II, Roche, Mannheim, Germany). Single cells were separated from debris, pelleted by centrifugation, and resuspended in growth medium consisting of Ham's F-10 medium plus 20% fetal bovine serum, 1% Penicillin/Streptomycin, (all from Invitrogen, Carlsbad, CA) and 2.5 ng/ml human b-FGF (Promega Corporation, Madison, WI). Cells were then plated into 75 cm² flasks and incubated for 24 hrs. Adherent cells were resuspended and plated onto MEAs (Multichannel Systems) in differentiation medium consisting of Neurobasal medium including 2% B-27 Supplement, 1% Penicillin/Streptomycin, and 1% GlutaMAX (all from Invitrogen, Carlsbad, CA) at a surface density of 300,000 or 200,000 cells/cm² for recording and stimulation experiments, respectively. Prior to seeding, surfaces were coated overnight with 40 µg/ml laminin (Sigma Aldrich, St. Louis, MO).

Cortical neurons were isolated as previously described [139]. Briefly, pregnant Sprague Dawley rats were sacrificed by CO₂ inhalation at gestational day 18 and pups were removed by Cesarean section. Cortex was isolated, meninges were removed, and a single cell suspension was prepared by triturating the cortex with a flame-polished glass pipette. Cortical cells were then seeded onto MEAs in MEM medium plus 1% penicillin/streptomycin, 10% horse serum, and 3% v/v of 20% glucose solution at a surface density of 225,000 cells/cm². Prior to use, the medium was glutamate-depleted

by 24 hr exposure to astrocytes in culture, and the MEA surface was treated overnight with 3% PEI dissolved in borate buffer.

4.1.3.2 Acquisition and analysis of electrophysiological data

Recordings of spontaneous cellular activity were made on a heat-controlled stage at 37° C at room atmosphere using a standard MCS recording array, sampling extracellular voltage from 60 contact pads at 20,000 Hz. Contact pad spacing was 200 μm , and diameter was 10 μm . Recordings of myocyte cultures were made at DIV 12 and 14, a window during which spontaneous contractile activity was maximal. Recordings of cortical neurons were made on DIV 21 after neurons have had time to establish mature synapses and network dynamics.

Spike sorting was performed using custom algorithms composed in a MATLAB environment and based in part on the algorithms discussed in [172]. Briefly, potential spikes were identified using a voltage threshold of 5x the RMS noise for each channel. All spikes were aligned to their point of maximal deflection based on a window 2 ms preceding and 4 ms following the threshold break-point, and principal component analysis PCA was performed on the resulting set of vectors. Using their position in a 2D space based on the first two PCs, likely spike events were then clustered using a K-means algorithm. The clustering process was user-guided, where the experimenter identified the starting number of clusters, and was then able to split and join clusters iteratively until spikes were correctly classified based on visual investigation. Because each cell produces action potentials with a unique shape, each of the resulting clusters represents the activity of a single cell (or “unit”) as its activity is recorded in the extracellular voltage trace (EVT) from a single electrode. Metrics of spike characteristics were then calculated based on the morphology of the average spike shape for each unit. In our case, SNR is the ratio of the peak-to-valley amplitude of a spike shape to the RMS

noise recorded on that electrode, and the Unit SD is the average SD along the 6 ms window surrounding the point of maximal deflection.

4.1.3.3 Analysis of contractile activity

An unordered myotube culture was grown on a commercially available MEA. On DIV 7, stimulation at selected electrode sites was delivered using an MCS signal generator and associated software. 10 Cycles of a 2V biphasic pulse with a 40 μ s duration was delivered across sets of 2 or 4 electrodes as indicated in Fig. 5.1-3. This regime was repeated with a frequency of 1 Hz. Videos of cells were acquired using the Qcapture-pro software at a frame rate of 25 frames per second. Automated localization of contractile activity was performed as discussed in [1]. Briefly, videos were analyzed using a series of image processing steps and pattern recognition steps, which make it possible to identify regions of synchronized contractility within videos of myotube cultures, returning the location of the contractile myotubes (Fig. 5.1-3, A - top) as well as their pattern of contractions (Fig. 5.1-3, A - bottom).

4.1.4 Results & Discussion:

4.1.4.1 Myotube vs. neuronal extracellular action potentials

Consistent with prior findings [189], myoblast differentiation into myotubes occurred on MEA surfaces. The myotubes form long, overlapping tubular structures, approximately 20 μ m to 40 μ m across and up to several mm in length (Fig. 5.1-1, A). By comparison, neurons are in the range of 20 μ m in diameter, with an accompanying neuritic arbor which can reach longer lengths (Fig. 5.1-1, B). Both cell types are electrogenic, creating transmembrane currents through roughly similar processes. The unique membrane composition, morphology, and behavior of each cell type, however, results in different EAP characteristics.

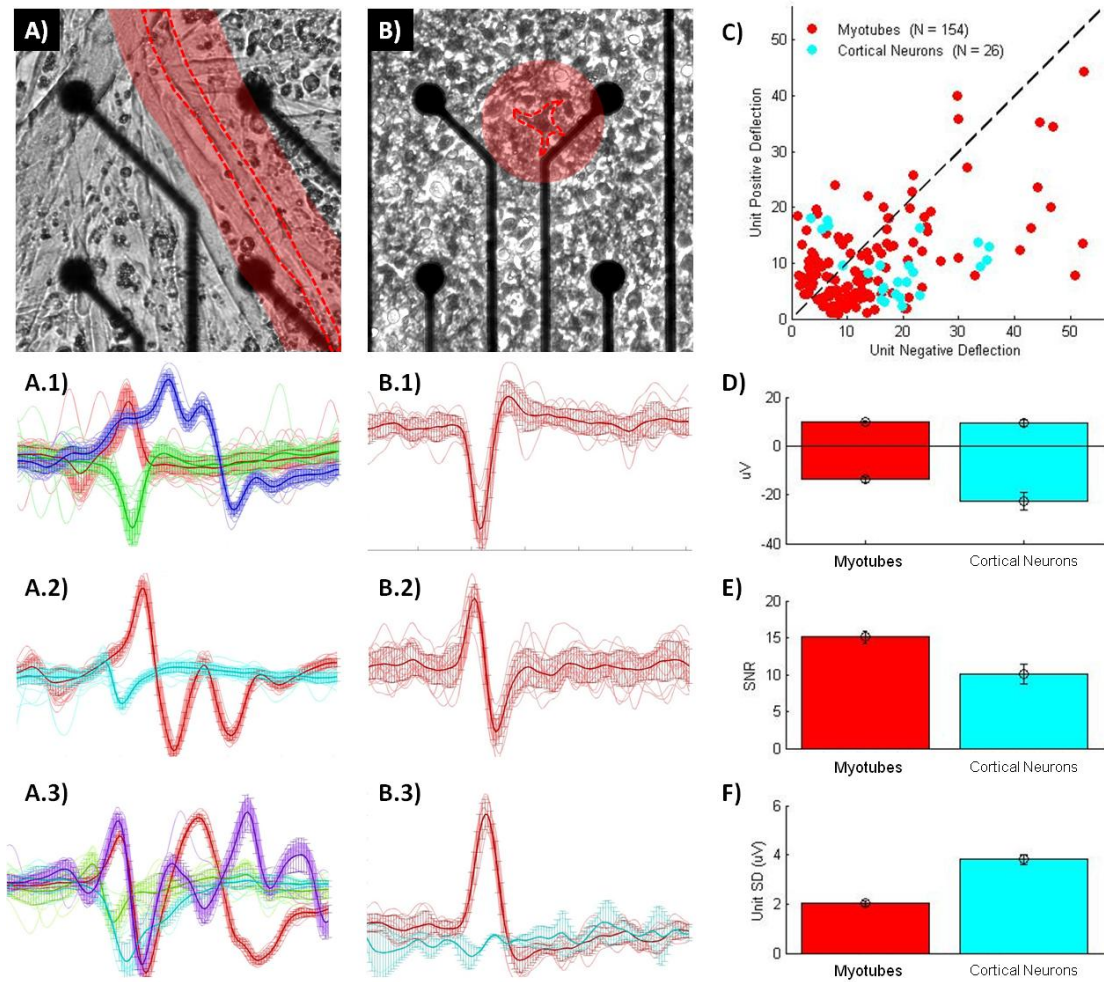


Figure 5.1-1. Characteristic myotube-electrode and neuronal-electrode interactions

A) Myotube morphology on MEA at DIV 12. A single myotube is outlined in red dashes, and the area over which its EAP is likely detectable is shaded in red. A1-A3) Representative myotube EAP shapes following spike sorting (6 ms shown, variable y-axis scale). B) Neuronal morphology on MEA at DIV 21. B1-B3) Representative neuronal EAP shapes following spike sorting (6 ms shown, variable y-axis scale). C) Scatter plot showing maximum positive deflection vs. maximum negative deflection for each unit. D) Average positive and negative deflections over all units. E) Average signal to noise ratio (SNR) over all units. F) Average unit standard deviation over all units. All error bars represent the standard error of the mean.

The shape of the EAP is primarily a result of the spatial relationship between the cell and the electrode contact [169, 226]. Neurons have static surface interactions over short periods of time, and recordable EAPs are primarily generated by the soma, which results in stereotyped EAP shapes like that pictured in Fig. 5.1-1, B.3. The predominance of EAPs that are negative and essentially unipolar is shown in Fig. 5.1-1, C by the large number of neuronal points appearing below the dashed line. Bipolar (Fig. 5.1-1, B2) and unipolar (Fig. 5.1-1, B3) EAP shapes may also be seen by recording from proximal neurites [169], but the vast majority of neurites are too small to produce a detectable signal without special modifications [227]. In comparison, the EAPs generated by myotubes are far more variable. Standard unipolar and bipolar EAPs are possible (Fig. 5.1-1, A1 – red and green), but arbitrary shapes are more frequent (Fig. 5.1-1, A1-3). This is likely due to the longer period over which the depolarization occurs, the propagation of the intracellular action potential along the myotube, and the changing shape and location of the myotube during excitation and contraction [228-230]. This variability is reflected in the greater scatter of the myotube points in Fig. 5.1-1, C. Despite the variability in spike shape, however, spikes generated by a single biological unit are remarkably reproducible, as evidenced by the small within-unit variability (Fig. 5.1-1 F).

Myotubes and neurons produce EAPs with similar amplitudes (Fig. 5.1-1, D). However, due to the variability between cultures, and even between electrodes within the same device [81], a direct comparison between myotube and neuronal EAP signal strength can only be made by normalizing the peak-to-valley amplitude of each unit by the noise associated with the electrode contact on which it is recorded. This analysis shows that myotube spikes tend to have a higher SNR than neuronal spikes. Current theories suggest that this is due to a combination of two effects stemming from the

increased size of myotubes relative to neurons [61]: 1) increased extracellular voltage change caused by the larger ionic movement accompanying depolarization and 2) improved electrode sealing and coverage due to the larger surface area contacted by myotubes.

4.1.4.2 Myotube network vs. neuronal network activity patterns

A striking feature of culture behavior for each cell type is the synchronous activation of multiple units, which appears as vertical bands of events in Fig. 5.1-2. This culture-level behavior has different root causes for myotubes and for neurons. Many myotubes are large enough to pass within recording distance of multiple electrodes (Fig. 5.1-1, A – red field). Therefore, a single myotube will frequently create EAPs that register as units on multiple electrodes. When the myotube depolarizes, each of these units registers a single event at the same time, causing the vertical banding in the raster plot of culture activity. The vertical banding therefore exists as a line of single events occurring at essentially the same time (Fig. 5.1-2, C).

In contrast, single neurons will only ever be within recording distance of a single electrode (Fig. 5.1-1, B – red field). Because of their far-reaching processes, however, it is possible for neurons to be synaptically connected with other neurons. As waves of activity travel through these multicellular networks, it produces synchronous activation of multiple electrodes as multiple neurons, each one within the recording field of a different contact, are activated. As such, the precise activation pattern of each unit in the network is unique (Fig. 5.1-2, D). Overall activity is driven by the network, so the activity of all networked units generally overlaps, but there is a much less clear cause-and-effect relationship between individual events on separate electrodes than exists with myotubes.

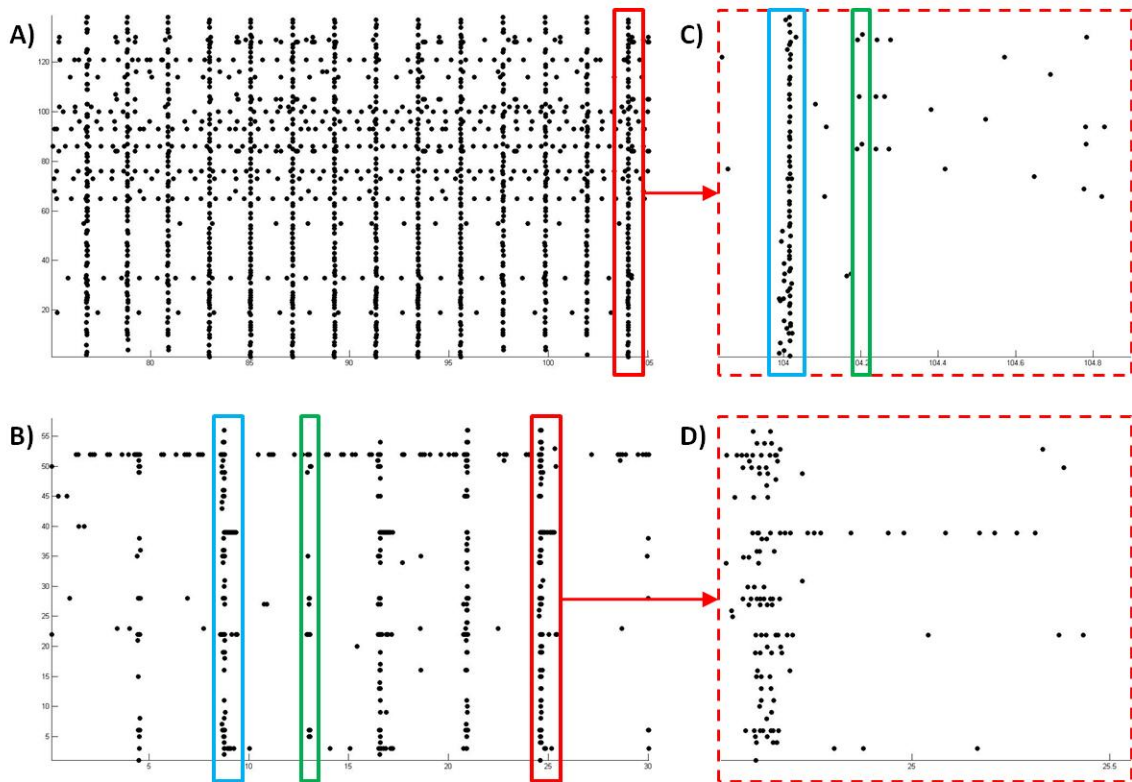


Figure 5.1-2. Synchronous multi-electrode activation in myotube cultures and neuronal cultures

Raster plot axes show the time (X-axis) and unit number (Y-axis) of each EAP as a point. The above raster plots show 30 s of data recorded from a myotube culture at DIV 12 (A), 30 s of data recorded from a neuronal culture at DIV 21 (B), and an expanded view of 1 s data segments from within A and B as indicated by the red rectangle (C and D taken from A and B, respectively). Two example networks are shown in each case (blue and green rectangles).

It is important to note that multiple networks coexist in the same culture (both in myotube cultures and neuronal cultures) as do units that are active independently from any other units. Each network's activity is observable as the synchronous activation of a different set of units (Fig. 5.1-2, B-C – blue and green rectangles). Coexisting networks in neuronal culture are expected, due to the large number of available neurons and the

structured and specific way synapses are formed and pruned. The behavior is surprising in myotubes, however, where disordered culture tends to produce multipolar or branching myotubes that contract as single entities [1] and where the precedent set by cardiac myocytes is the formation of mass syncytia. If myotubes fused with all other contacted myotubes, the result would be a single contractile entity, as in cardiac myotubes. The existence of multiple myotube networks within an unstructured culture suggests that myotube fusion is a directed process which proceeds with some specificity [188].

4.1.4.3 *Selective stimulation of myotube networks*

The discovery that multiple independent myotubes are identifiable by their pattern of spontaneous bio-electrical activity, and that their independence is conserved even when they may partially overlap, led to an investigation of whether these myotube networks can be selectively stimulated. Stimulation of a central region of the culture resulted in contraction of multiple myotubes within the culture (Fig. 5.1-3, A), paced along with the stimulus. Stimulation of more peripheral regions, however, triggered contraction only of selected cells within the culture (Fig. 5.1-3, B-D). Stimulation of an intermediate area between two of these cells resulted in simultaneous activation of both (Fig. 5.1-3, E).

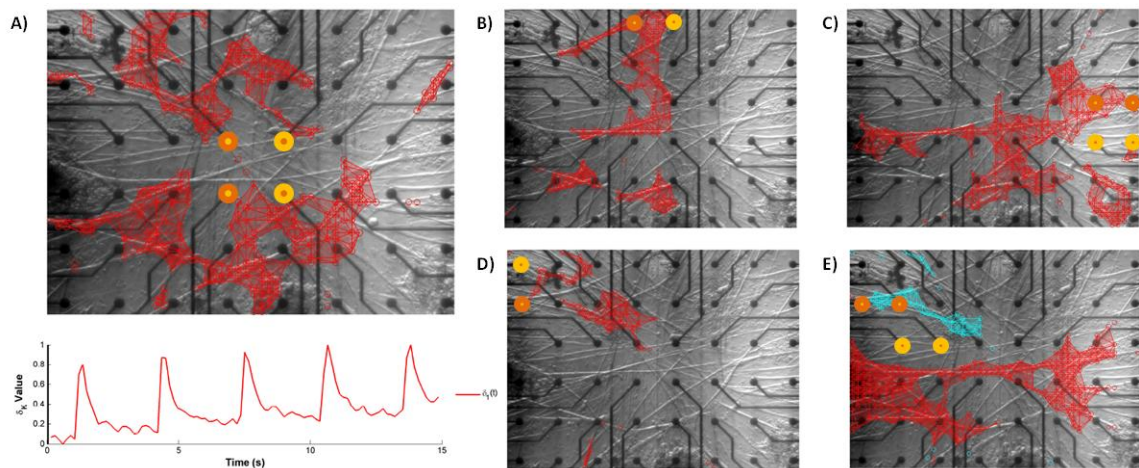


Figure 5.1-3. Stimulation of myotube networks using a substrate-embedded MEA

Active myotubes are identified based on automated analysis of video-micrographs, and indicated by the colored meshwork, and the electrodes used for stimulation are indicated by the orange and yellow dots. A) Stimulation in a central region, triggering contraction in a large area of the overlying myotube layer. B-D) Stimulation at peripheral sites, showing activation of subsets of myotubes. D) Stimulation at an intermediate site, showing activation of the myotubes from C and D in red and blue hatchwork, respectively.

Temporally selective myotube stimulation has been demonstrated [224], as has the spatially selective stimulation of neuronal preparations [208]. However, this is the first demonstration of spatially selective stimulation of myotubes and the subsequent contraction of a selected subset of cells in the culture. This finding reinforces the notion that multiple independently active myotubes can coexist in the same culture, even when they may be in direct physical contact with one another at points along their length. Additionally, it confirms the ability to use MEA technology to selectively stimulate contraction in specific myotube networks without stimulating those around them. Spatially-selective stimulation frees researchers from dependence on spontaneous contractility or bulk stimulation as a means of observing contractile activity in skeletal muscle cell preparations.

4.1.5 Conclusions:

By integrating a skeletal myotube culture with a substrate embedded MEA, we have shown that spontaneously contractile myotubes are capable of producing activity that is detectable both optically and electrically. Skeletal myotubes have EAPs with SNR similar to those recorded from neuronal somata cultured under similar conditions. However, myotube EAPs are longer in duration and can be multiphasic, while neuronal depolarizations are rapid, small, and predictably monophasic. The activity of each cell can be identified based on its unique EAP signature, and the activity of single myotubes

spanning multiple electrode contacts can be observed as linked activity between these units. Additionally, multiple independently active myotubes exist in the same culture despite physical contact with other myotubes and can be distinguished optically based on contraction or on the network-like behavior of the underlying electrodes.

Microdevices with integrated cellular components can be classified based on whether they are used to sense or induce cellular activity and on whether they have clinical or laboratory applications. The integration of skeletal myotubes with MEAs has implications in each of the categories above. The ability to monitor myotube excitation and contraction during development and over extended periods may provide new insight into development and diseases of the neuromuscular system. In the field of skeletal muscle tissue engineering, the ability to study the means by which myotubes fuse or remain independent may fuel progress in constructing skeletal tissue grafts capable of graded contraction through activation of subsets of myotubes [197]. Similarly, the ability to trigger specific myotubes in a culture provides a method of control over microscale biorobotic actuation [65]. Most interesting, however, is the potential to combine skeletal myotube cultures with neuronal cultures on MEAs [189]. Integration of motoneuron-myotube co-cultures with an MEA substrate would provide researchers with a sensitive means of observing the NMJ, unraveling the complicated trophic communication occurring between motor neurons and myotubes and observing simple neuronal circuit formation, such as the spinal reflex arc. Additionally, it may open the door to new approaches to neural interfaces. One can conceptualize a neural interface designed to restore conscious motor control of prosthetic devices based on using individual myotubes as biological signal amplifiers for motor intention carried along regenerated motor fibers [231]. Using a myotube-integrated MEA would provide regenerating motor axons with a neurotrophin-secreting target for reinnervation. Recording EAPs from

myotubes onto which PNS axons had successfully regenerated would solve the problems associated with recording from peripheral motor axons because of their small size [45, 227], inducing and maintaining neurite ingrowth into regenerative electrodes [43, 48], and isolation of a large number of motor signals from other neural activity carried in the PNS [44, 46]. Such an approach potentially increases the communication bandwidth of the targeted muscle reinnervation approach [52, 53] by reducing it to a single cell scale. Future work will include the integration of an MEA with topographical guidance cues in order to create structured myotube cultures, and ultimately, facilitate the formation of structured motor neuron-myotube co-cultures.

4.2 A topographically modified substrate-embedded MEA for directed myotube formation at electrode contact sites

4.2.1 Abstract:

Myoblast fusion into functionally distinct myotubes, and their subsequent integration with the nervous system, is a poorly understood phenomenon with important applications in basic science research, skeletal muscle tissue engineering, and cell-based biosensor development. We have previously demonstrated the ability of microelectrode arrays to record the extracellular action potentials (EAPs) of myotubes, and shown that this information reveals the presence of multiple, Electrophysiologically independent myotubes even in unstructured cultures where there is extensive physical contact between cells. Additionally, we have shown the ability if microscale topographical trenches to guide the myoblast alignment and fusion process, and shown that they are able to direct contractile activity to specific locations. In this paper, we combine substrate embedded MEA technology with topographical patterns in order to develop a novel technological platform for exploring myotube independence, with the

hopes of expanding applications of the system to also examine myoblast fusion myotube innervation.

4.2.2 Introduction:

Muscle tissue generates controllable, graded, and sustainable forces through the highly regulated activation of distinct motor units, each consisting of a unique set of muscle fibers [195]. The ability of skeletal myotubes to remain electrophysiologically distinct from their neighbors, therefore, is one of the traits required to fulfill this role. This stands in stark contrast to other electrogenic cell types such as neurons, where CNS function depends on the formation of multicellular networks, or cardiomyocytes, where cardiac output depends on the synchronicity of their contractions. Each myotubes' ability to remain independent from its neighbors is made more puzzling by the developmental origin of myotubes, which are formed by the rapid fusion of myoblasts from a seemingly homogenous pool of precursor cells. Not only does this fusion process result in highly aligned, tightly packed, yet independent myotubes within a single muscle, but also in the formation of distinct muscles with specific sites of attachment relative to the joints at which they act. Despite the clear importance of regulating the myoblast fusion process in the development of the musculoskeletal system, however, little is known about the process [196, 206]. The study of myoblast fusion and myotube independence has applications outside of basic science as well. Muscle tissue engineering is a field with multiple applications in human health and regenerative medicine. The study of how to generate and manipulate myotube formation and how these myotubes are integrated with the nervous system is an important step in muscle tissue engineering for clinical applications [181, 193].

A major roadblock to progress in this field is the lack of *in vitro* models allowing researchers to probe the means by which myotube independence is preserved over the

course of myoblast fusion. Studies of muscle cells *in vitro* have focused largely on differentiation, metabolism, morphology, or force generation, but have not focused on myotube independence [1]. While techniques for identifying single motor units *in vivo* exist, these systems suffer the limitations of all *in vivo* system. In both cases, the techniques used to interrogate the samples are frequently destructive to the cells, making time-course studies difficult.

By integrating tissue engineering techniques with novel dual-modality (optical and bioelectrical) sensing technologies, we are developing a lab-on-a-chip test bed for non-invasive examinations of myotube fusion. Because an important part of muscle tissue is its highly aligned structure, we are incorporating topographical guidance cues into our sensing array as a means of exercising control over culture morphology. It is our hope that this combination of technologies will act as a seed platform, with the potential to be adapted for use in a wide variety of applications following relatively simple redesign. For example, electrode contact spacing and shape can be modified to provide basic science researchers tool for monitoring myoblast fusion during development. For cell-based biosensor applications, topographical guidance cues can be used to direct myotubes to electrode sites in order to maximize the number of independent signal producing units available to a detection array. Finally, topographical modifications can be used to produce microenvironments capable of sustaining multiple cell types in structured cocultures. An example of this would be the coculture of myotubes with motor neurons for the examination of simple neural circuits, like the spinal reflex arc, the development of a functional neuromuscular tissue phantom for high-throughput screening and biodetection, or the development of a regenerative neural interface targeted to the peripheral nervous system.

4.2.3 Methods:

4.2.3.1 *Device fabrication*

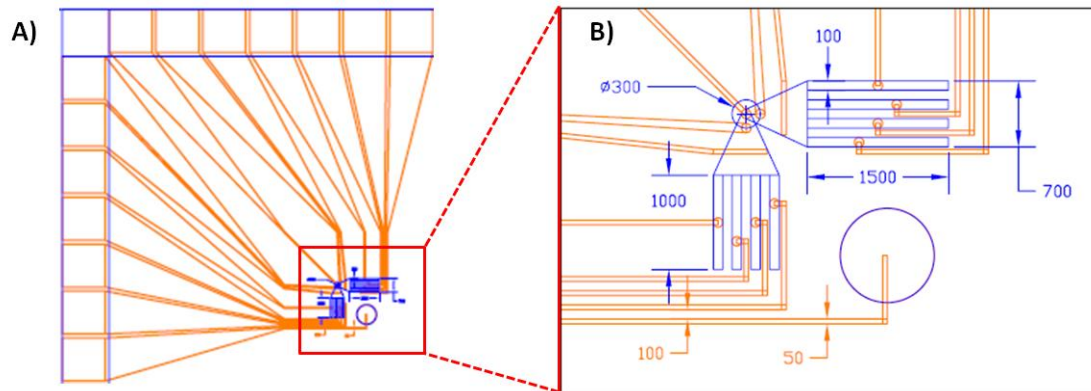


Figure 5.2-1. myo-MEA schematic

A) Upper-left quadrant of the device, showing connections between 1 of the 4 recording fields and the external contact pads. B) Detailed view of recording field from A. Gold conducting features shown in orange, SU-8 topographical features shown in blue. All units in μm .

A prototype device was designed incorporating topographical modifications that direct myotube formation and spinal cord explant (SCE) outgrowth with a substrate embedded MEA. Specifically, two regions of trenches used to direct myotube formation to specific electrode sites are connected to a central field for a spinal cord explant (SCE), which is spatially separated from the grooves to allow neuron/myotube contact only through axonal outgrowth (Fig. 5.2-1 B). The two wing regions, oriented horizontally and vertically, consist of four grooves with a single electrode contact at the bottom. The central field contains 5 recording electrodes to record from multiple points beneath the explant body and axonal outgrowth. A large pad is included as an internal reference electrode (not shown). The electrodes are patterned to interface with a Multichannel Systems MEA recording head-stage through external contact pads located around the periphery of the chip (Fig. 5.2-1 A).

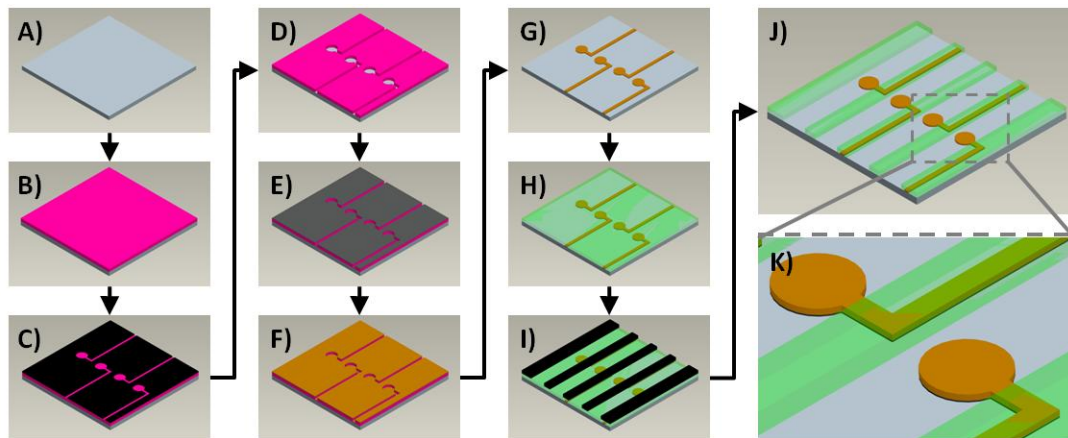


Figure 5.2-2. Schematic of microfabrication process

Steps A-K are explained in the text.

The electrode contact and lead pattern is produced using a lift-off technique [232]. Briefly, a layer of photoresist (PR) bearing the electrode pattern is produced using standard optical lithography (Fig. 5.2-2 A-D). The PR is then undercut using a short hydrofluoric acid (HF) etch followed by sputtering of a 200/700 Å thick chromium/gold (Cr/Au) conducting electrode layer (Fig. 5.2-2 E-F). The PR is dissolved in acetone, removing the conducting layer everywhere except the electrode pattern (Fig. 5.2-2 G). A layer of SU-8 PR is then spin-coated onto the electrode-patterned surface (Fig. 5.2-2 H) and exposed and developed using a topographical feature mask to generate topographical trenches (Fig. 5.2-2 I) and central confinement regions, also selectively exposing the electrode contact pads located at the bottom of both while leaving the electrode leads electrically insulated from the culture environment (Fig 5.2-2 J-K). A PDMS ring is affixed to the surface creating a culture chamber around four recording fields, enabling multiple simultaneous experiments (Fig. 5.2-3 B).

4.2.3.2 *Myoblast isolation and culture*

Myoblasts were isolated and cultured as previously described [1]. Briefly, pregnant Sprague Dawley rats were sacrificed by CO₂ inhalation at gestational day 21 and pups were removed by Cesarean section. Hind limb muscles were removed, and tissue was finely minced and digested (20 min at 37° C) in PBS containing 1.5 U/ml collagenase (type D, Roche, Mannheim, Germany) and 2.5 U/ml dispase (type II, Roche, Mannheim, Germany). Single cells were separated from debris, pelleted by centrifugation, and resuspended in growth medium consisting of Ham's F-10 medium plus 20% fetal bovine serum, 1% Penicillin/Streptomycin, (all from Invitrogen, Carlsbad, CA) and 2.5 ng/ml human b-FGF (Promega Corporation, Madison, WI). Cells were then plated into 75 cm² flasks and incubated for 24 hrs. Adherent cells were resuspended and plated onto MEAs (Multichannel Systems) in differentiation medium consisting of Neurobasal medium including 2% B-27 Supplement, 1% Penicillin/Streptomycin, and 1% GlutaMAX (all from Invitrogen, Carlsbad, CA) at a surface density of 300,000 cells/cm². Prior to seeding, surfaces were coated overnight with 40 µg/ml laminin (Sigma Aldrich, St. Louis, MO).

4.2.3.3 *Electrophysiological and optical data acquisition and analysis*

Recordings of spontaneous cellular activity were made on a heat-controlled stage at 37° C at room atmosphere using a standard MCS recording array, sampling extracellular voltage from 60 contact pads at 20,000 Hz. Contact pad spacing was 200 µm, and diameter was 10 µm. Recordings of myocyte cultures were made at DIV 14, when spontaneous contractile activity is maximal. Spike sorting was performed using custom algorithms composed in a MATLAB environment and based in part on the algorithms discussed in [172]. Briefly, potential spikes were identified using a voltage threshold of 5x the RMS noise for each channel. All spikes were aligned to their point of maximal

deflection based on a window 2 ms preceding and 4 ms following the threshold breakpoint, and principal component analysis (PCA) was performed on the resulting set of vectors. Using their position in a 2D space based on the first two PCs, likely spike events were then clustered using a K-means algorithm. The clustering process was user-guided, where the experimenter identified the starting number of clusters, and was then able to split and join clusters iteratively until spikes were correctly classified based on visual investigation. Because each cell produces action potentials with a unique shape, each of the resulting clusters represents the activity of a single cell (or “unit”) as its activity is recorded in the extracellular voltage trace (EVT) from a single electrode. Metrics of spike characteristics were then calculated based on the morphology of the average spike shape for each unit. In our case, SNR is the ratio of the peak-to-valley amplitude of a spike shape to the RMS noise recorded on that electrode, and the Unit SD is the average SD along the 6 ms window surrounding the point of maximal deflection.

To dynamically analyze contractile activity of myotubes, videos of cell behavior were acquired after the onset of spontaneous contractility and were analyzed as described in [1]. Briefly, videos were analyzed using a series of image processing and pattern recognition steps which made it possible to identify regions of synchronized contractility within videos of myotube cultures. These locations are then taken to be the location of the contractile myotubes.

4.2.4 Results and Discussion:

4.2.4.1 Device characterization

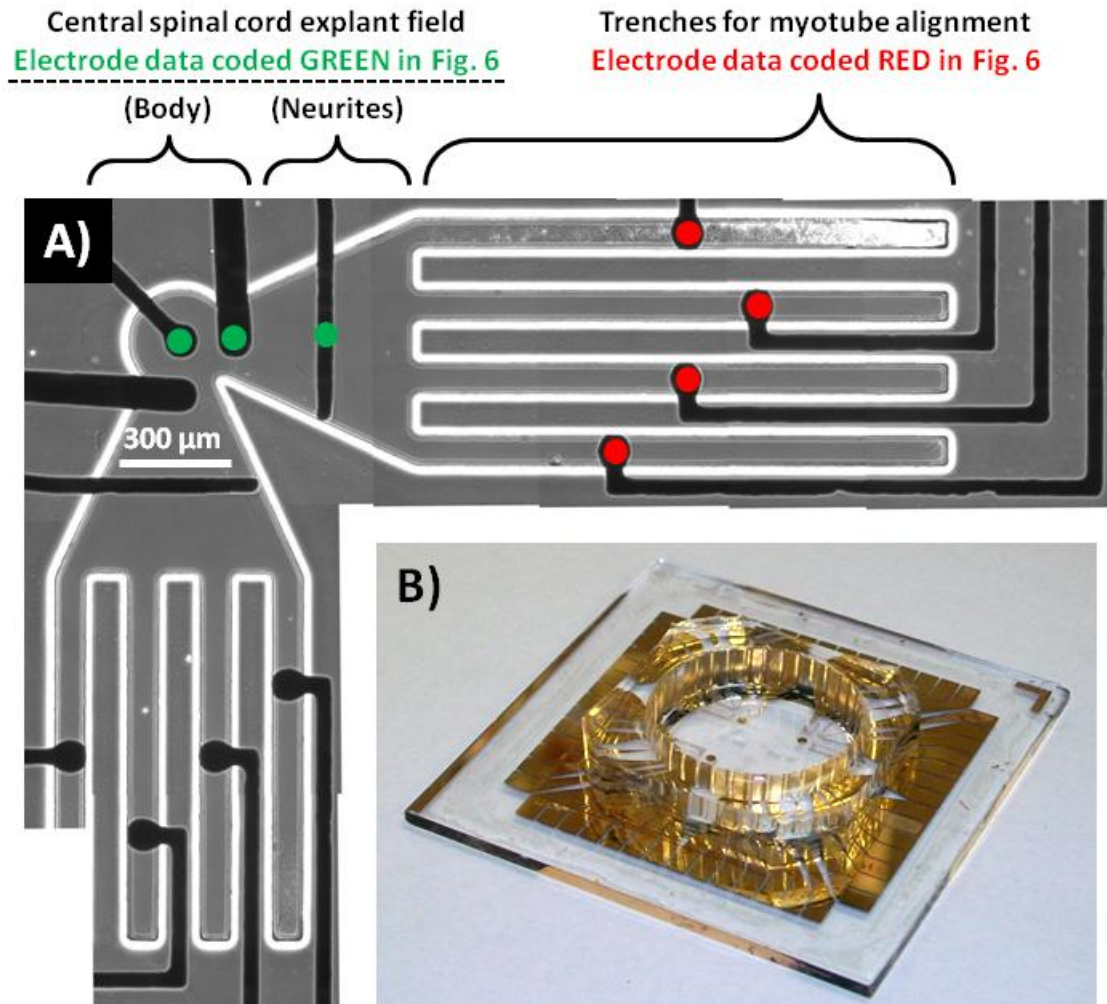


Figure 5.2-3. Myo-MEA prototype

A) Microscopic view of prototype recording field schematized in Fig. 5.2-1, B. B) Image of finished prototype, including PDMS culture chamber.

The fabrication process generates devices capable of recording myotube and explant EAPs and withstands repeated cycles through the sterilization-usage-regeneration processes involved in cell culture (Fig. 5.2-3 A-B). In examinations of the electrode noise-floors (data not shown), it was determined that the gold leads establish electrical

continuity between the recording contact sites and the external contacts which interface with the MCS head stage. Electrode noise was low ($\sim 3 \mu\text{V}$) for functional electrodes, while it was elevated to the maximum noise detectable using the MEA recording array ($\sim 40 \mu\text{V}$) where electrode continuity with the culture fluid was lost (either by scratching the lead under the SU8 insulating layer or through incomplete development of trenches). The SU8 layer has good adhesion properties, without cracking or delamination flaws (Fig. 5.2-3 A). Additionally, the SU8 layer is optically clear, facilitating the observation of culture conditions in and around the experimental fields. Final prototypes have 4 recording fields inside of the PDMS culture ring, enabling parallel experiments (Fig. 5.2-3 B).

4.2.4.1 *Myotube formation guided by trenches*

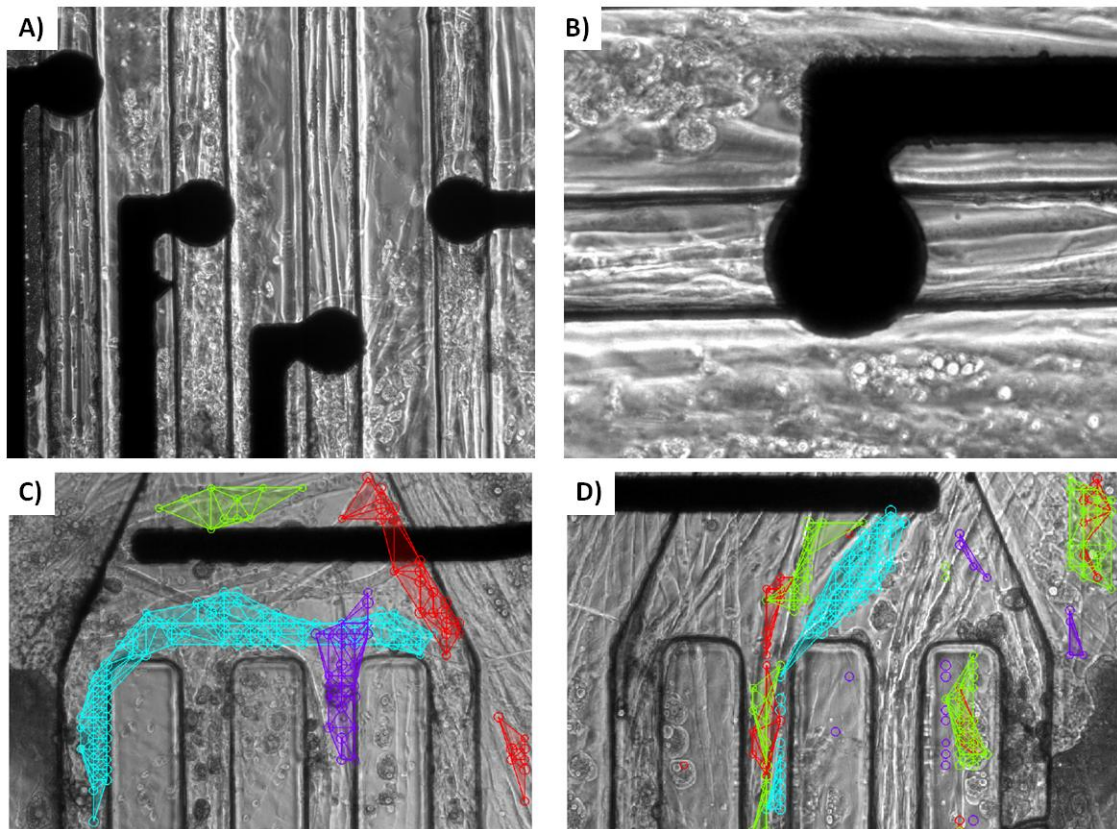


Figure 5.2-4. Myotube differentiation and guidance on myo-MEA topographical features

A-B) Myotubes lying along the bottom of trenches and on top of electrode contacts in a “wing” region. C-D) Myotube contractility funneled down trenches.

Consistent with our prior studies on the effects of microscale trenches on myotube morphology, topographical features constructed on top of the substrate embedded MEA are able to direct myotube formation and morphology. Multiple myotubes are observed to form along the bottom of the trenches, aligned in parallel with the major trench axis. Similarly, the topographical features are able to direct myotube contractility to the trenches. However, because these trenches are open ended and connect to a large open field, they have the interesting effect of funneling multiple myotubes to a single trench (Fig. 5.2-4 D), and of funneling separate “fingers” of a single myotube down multiple trenches (Fig. 5.2-4 C).

4.2.4.1 Detection of myotube EAPs

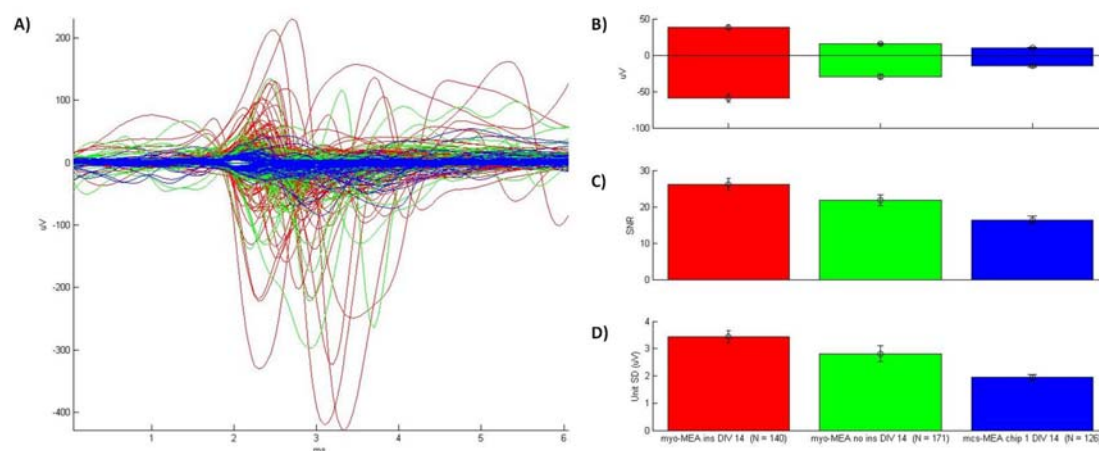


Figure 5.2-5. Myo-MEA recordings of myotube EAPs

EAPs are detected from sister cultures grown on topographically patterned myo-MEA (red), uninsulated myo-MEA (green), and commercially available MEA (blue). A) All units for each device superimposed (6 ms of data

shown). B) Average positive and negative deflection for all units measured in μV . C) Average SNR for all units.

D) Average unit SD for all units.

We are able to use the topographically modified myo-MEA prototypes to record the bioelectrical activity of spontaneously active myotubes in similar fashion to commercially available MEAs. Spike sorting of the resulting extracellular voltage traces (EVTs) is possible, yielding unit-specific EAPs with high reproducibility, and low intra-unit variance (Fig. 5.2-5 D). A comparison was made of myotube EAP qualities measured on three different types of electrode; 1) topographically modified myo-MEAs, 2) the myo-MEA electrode pattern without the insulating topographical SU8 layer, and 3) commercially available MEAs. There is similar EAP morphology recorded on all substrates, exhibiting the characteristic multiphasic and unpredictable EAP morphologies (Fig. 5.2-5 A). However, there is an amplification of EAP amplitude observed on the fully insulated prototypes (Fig. 5.2-5 B) relative to both the uninsulated and the commercially available MEAs. This contributed to the insulated myo-MEA also providing EAP recordings with a larger SNR (Fig. 5.2-5 C), however the effect is less than would be expected based on the larger amplitudes. This finding is consistent with the theory that guidance of myotube formation to electrode sites by the topographical trenches results in an increase in electrode sealing [62, 226, 233], but that the reduction in recording surface area results in a higher noise floor. The finding that the uninsulated myo-MEA electrode pattern also showed increased amplitude and SNR over the commercially available MEA is somewhat surprising, as theory would dictate that current leakage through the uninsulated leads and into solution would diminish the effective voltage recorded. However, in cultures this dense, the overlying cell layer may provide some insulation, diminishing this current shunt. When combined with the much larger surface area available for recording, this may explain the observed increase in amplitude.

4.2.4.2 Changes in myotube dynamics due to topographical modification

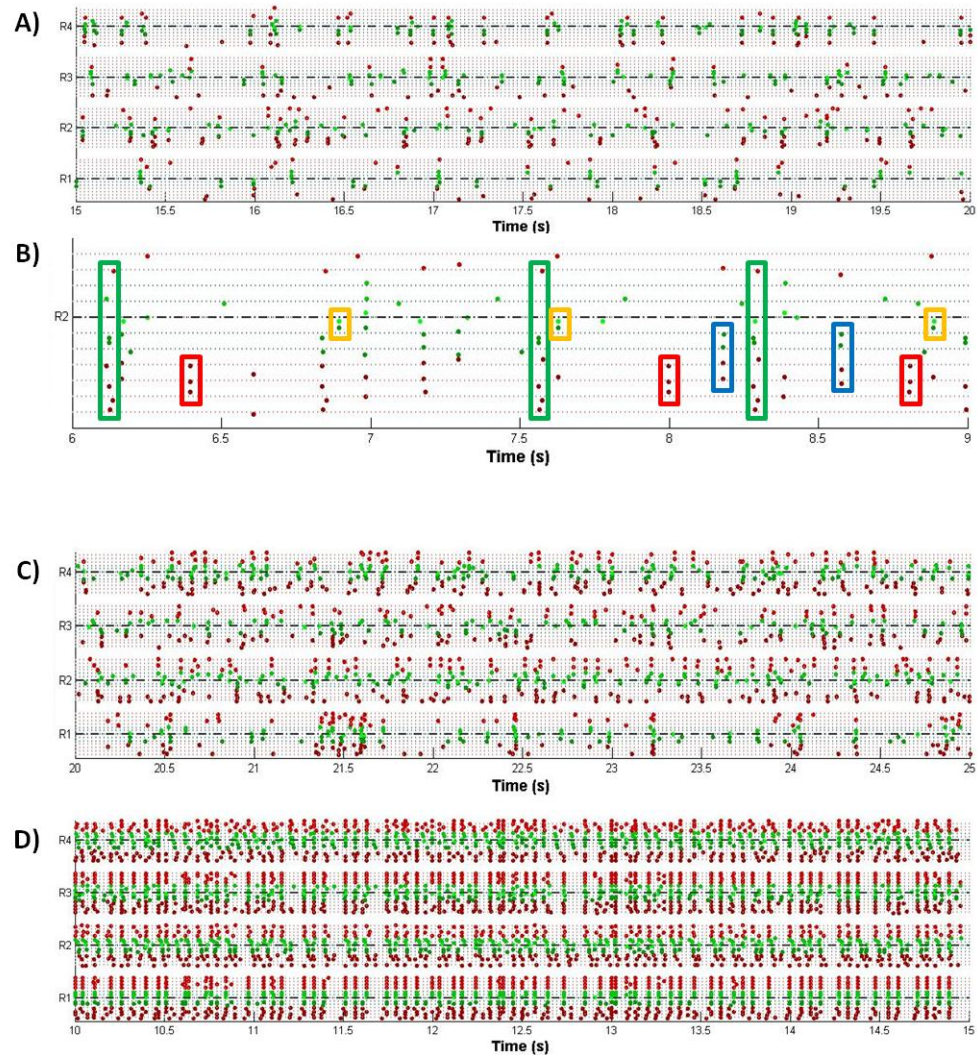


Figure 5.2-6. Patterns of myotube activation on topographically patterned vs. uninsulated myo-MEAs

A) 5 seconds of activity detected in four fields of a topographically patterned myo-MEA. B) 3 Seconds of data from a single recording field in which repeating activation motifs have been identified by hand (colored rectangles). Activity detected in four fields of an uninsulated myo-MEA during non-seizure-like (C) and seizure-like (D) activity. Recordings made at DIV 14. Each raster plot consists of four horizontal fields, representing each of the four recording fields. The electrodes in each field are color-coded according to location (central electrodes in green, wing electrodes in red).

Using the spike sorted EAP data, it is possible to identify spatial and temporal patterns in myotube activation. These patterns of activity are affected by the topographical patterning of the electrode. Figure 5.2-6 A shows 5 seconds of data recorded from the 4 fields of a myo-MEA. Total activity is the result of a combination of repeating vertical banding patterns (generated by myotubes that span multiple trenches and the central region), and units that fire in isolation (generated by myotubes confined to a single trench). Obvious repeating activation motifs occurring in 3 seconds of data from a single recording field have been identified by hand (Fig. 5.2-6 B – colored rectangles). The distribution of the synchronous bursting patterns is limited to each of the 4 recording fields (i.e., there is little activity that spans more than 1 recording field). By comparison to the insulated myo-MEA, there are two noteworthy observations about the EAP activity recorded by the the uninsulated myo-MEA electrode pattern. There are more units recorded on it (a 20% increase over the insulated myo-MEA), and these units are have a higher activation rate. This is consistent with the much larger recording field, which in the uninsulated myo-MEA includes the leads as well as the contacts. This larger electrode area records activity of all cells along its path, contributing to the larger number of units detected. Additionally, these units are active more frequently, and are capable of switching between “seizure-like” state, where every unit fires synchronously and rapidly, and more “non-seizure-like” state, where individual units and activation motifs can be identified. One possible explanation is that the culture is able to grow in an uninterrupted sheet in which every cell is mechanically coupled to every other cell. This may create a situation where contraction of a myotube mechanically triggers the contraction of neighboring cells, even though they may remain electrophysiologically distinct. The presence of the topographical cues may be enough to break up the

mechanical coupling to the point that culture-wide “epileptic” events are no longer possible.

4.2.5 Conclusions:

4.2.5.1 *Structured myotube culture on a topographically modified substrate embedded MEA*

Based on the need for an *in vitro* means of probing myoblast fusion and myotube independence for basic science applications, and the need for functional and structured myotube cultures for tissue engineering and biosensing applications, we have integrated topographical modifications which induce cell guidance with a substrate embedded MEA. To facilitate the device’s future integration with spinal cord explants for the development of structured motor neuron-myotube cocultures, we have selected topographical modifications in the form of two trench regions (for myotube formation) joined to a central region (designed for spinal cord explant adhesion and spreading). The topographical modifications are able to direct myotube formation and contractility, as detected optically, and the underlying substrate embedded MEA is able to record EAPs from the overlying myotubes, which can then be spike sorted to identify the activity of multiple individual myotubes recorded on a single electrode. Further, the topographical modifications induce a change in the quality of the EAPs observed which is consistent with current theories on cell-electrode interactions, and a change in the behavior of the myotube culture which is caused by the induced structure.

4.2.5.2 *Future Directions*

We have developed the techniques required to quantify contractile and bioelectric activity generated by neurons and myotubes. Furthermore, we have used microfabrication processes to create culture systems that modulate these behaviors. The next step in advancing the myo-MEA technology platform is leveraging our existing

analytical tools, designed to observe individual cells, to create a means of rigorously quantifying the behavior of multiple cells acting in concert. This will provide a way to fully interpret the behaviors of myotubes and neurons (both of which are able to associate with other cells of either type) in our structured cultures. This tool will take the form of automated pattern identification algorithms that isolate the repeating motifs generated by myotubes that span multiple electrodes (i.e., the vertical banding patterns in fig. 5.2-5F). Isolation of these activation motifs will allow us to identify how many independent myotubes are active on an electrode surface and their spatial distribution. Within the context of the next-generation hybrid-biosensors and neural interfaces we have discussed, this is a good indicator of the number of independent signals the interface will be able to record.

5 Future directions in co-culture

5.1 Spinal cord explant culture on a topographically modified substrate- embedded MEA guides axonal outgrowth and facilitates selective recording: Toward a neuromuscular system on a chip

5.1.1 Abstract:

Integration of a neuronal cell source is a necessary component of a motor neuron-myotube coculture system. The ability of the topographical modifications on the myo-MEA to support explant integration are, therefore, examined. We find that the central regions of the recording fields in the myo-MEA are sufficient for stabilizing explant adhesion and recording their extracellular action potential (EAP) bursting activity simultaneously from multiple electrodes underlying the explant body. Explant activity is not, however, present on electrodes located in the trenches. Furthermore, the topographical trenches are able to guide myotube formation to specific locations, facilitating the identification of independent myotube activity. The feasibility of combining these two cell types on the myo-MEA platform is discussed, along with an experimental approach for identifying the motor neuron-myotube connectivity that is expected to form.

5.1.2 Introduction:

Ultimately, the myo-MEA was developed as a co-culture system in which we can observe the transmission of action potentials from a neuronal population to a myotube population. This device is represented schematically in Figure 6.1-1, showing the necessary spatial relationships of the component cell types (Fig. 6.1-1 A), along with the modalities of data to be recorded from each location (Fig. 6.1-1 B-D).

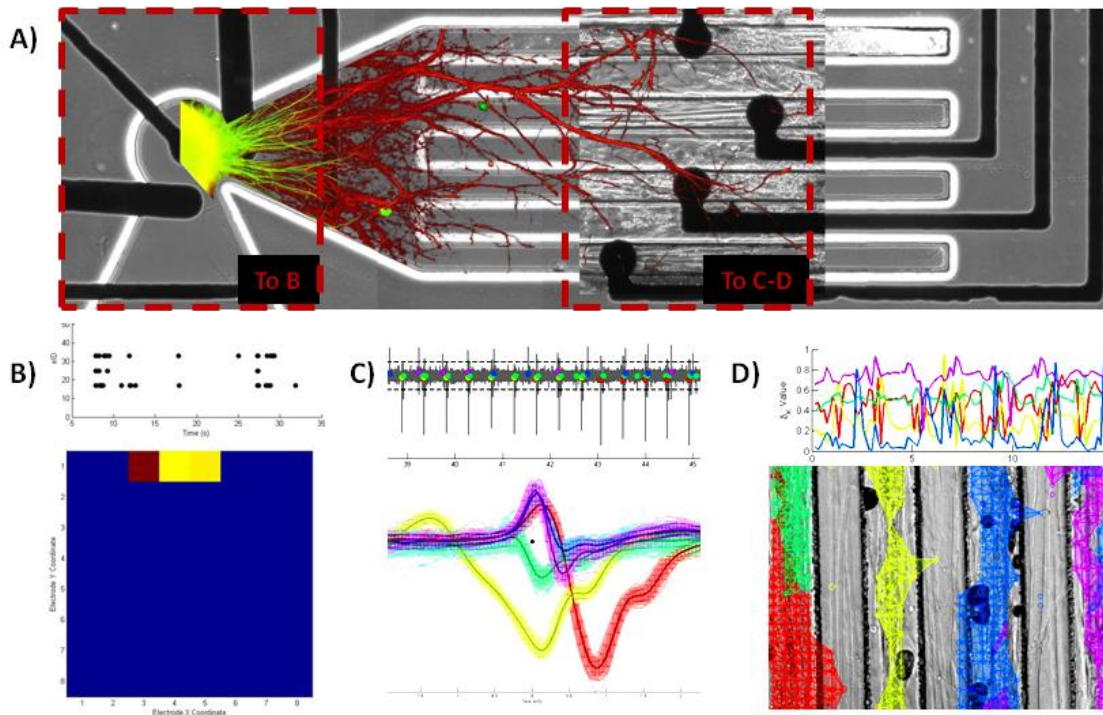


Figure 6.1-1. Conceptual coculture possible using myo-MEA design

A) Spatial relationship between explant and myotube culture zones. B) Example of MEA-based identification of spatially confined explant EAPs. C) Example identification and spike sorting of myotube EAPs. D) Identification of myotube contractility patterns in microscale topographical trenches.

In order to successfully meet this goal, a neuronal source with controllable architecture needs to be appropriately selected, and deployed in the device demonstrating localized extracellular actions. As discussed in Chapter 4 of this thesis, explants provide an ideal source of neuronal input because of the highly localized EAP activity and aggressive axonal outgrowth. As depicted in Figure 6.1-1 A, these two qualities may enable them to synaptically contact the trench-bound myotubes from the central explant region through axonal outgrowth. This would enable the selective recording of explant EAPs from the central region, and myotube EAPs and contractions from the trench region. As a test of this hypothesis, we have cultured explants on the central region of the myo-MEA recording field and monitored for axonal outgrowth, while

recording from all electrodes to determine whether EAP activity is confined to the central region while axons infiltrate the trenches.

5.1.3 Methods:

5.1.3.1 *Cell culture*

Spinal cord explants are prepared using procedures based on [219]. Briefly, pregnant Sprague Dawley rats were sacrificed by CO₂ inhalation at gestational day 15, and pups were removed by Cesarean section. Spinal cord was removed posteriorly and transferred to a PDMS- lined petri dish, bisected longitudinally, and finely minced transversely into sections 200 – 300 µm thick. Explants were then plated onto myo-MEAs, all of which had been adsorbed overnight with laminin at 40 ug/ml in 10 µL of medium, at which point they were precisely positioned in the central explant zone of each recording field. After 5 min, allowing for initial adhesion, enough medium was added to just cover the explant, and it was placed in an incubator at 5% CO₂ and 37 deg C. Medium was replaced every 2 days.

5.1.4 Results:

5.1.4.1 Spatial distribution of neuronal and myotube EAP sources

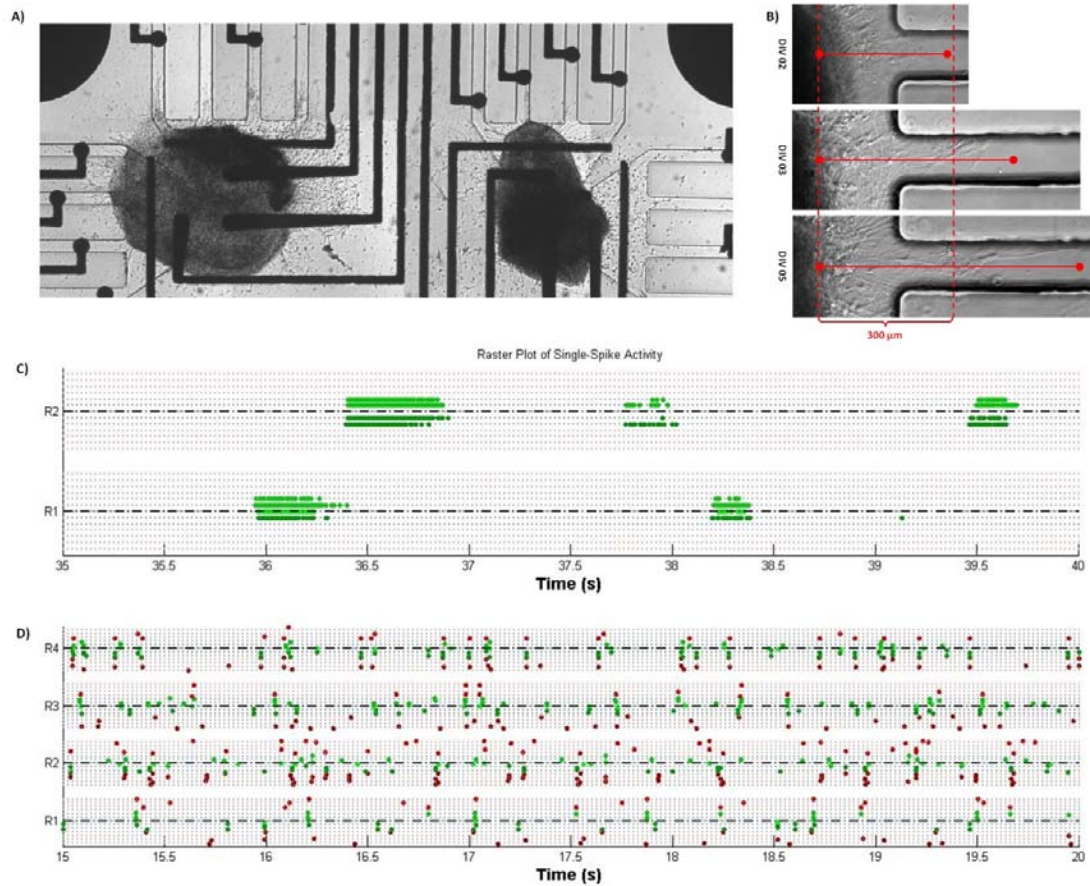


Figure 6.1-2. Explant integration with the myo-MEA

A) Spinal cord explants (SCE) cultured in central region of 2 neighboring recording fields. B) Axonal guidance down trenches from DIV 2 - 5. C) 5 Seconds of bursting EAP activity recorded from explants in (A). D) 5 Seconds of myotube EAPs recorded from all 4 of a myo-MEA. In raster plots (C) and (F), units are color-coded based on electrode location (central region = green, trench wing regions = red).

SCE adhere to the myo-MEA surface, with the explant body largely confined to the central region (Fig. 6.1-2 A). By DIV 5, aggressive axonal outgrowth extends along the glass bottom and is guided down the topographical channels (Fig. 6.1-2 B). By DIV 7 explant bodies generate spontaneous bursting activity detectable on the central region

electrodes, consisting of multiple, rapid, EAPs (Fig. 6.1-2 C). Bursting behavior can be observed from multiple explants on the same myo-MEA, however, the distance between them is sufficient that their activity is not coupled. Additionally, explant EAP activity is bound only to the central region, and even up to an age of 3 weeks in culture explant bursting activity is never detectable on the trench electrodes. By comparison, myotube EAP activity can be observed in the wing regions (red points) as well as the central regions (green points) (Fig. 6.1-2 D).

5.1.5 Discussion and Conclusions:

5.1.5.1 *Feasibility of detecting information transmission from a neuronal population to a myotube population in structured cocultures*

Though the two cell types have not been cultured together at this point, we expect the motor neurons to make contact with myotubes based on NMJ regeneration that occurs *in vivo* and on the unstructured *in vitro* systems in which physical interactions have been observed. Our proposed system addresses the unique problem of using a structured coculture system to identify transmission of information. Detecting this phenomena based on activity of each cell type will require a unique analytical approach. Multiple patterns of connectivity may exist (Fig. 6.1-3 A-C), and it is important that an experimental paradigm be developed which makes it possible to detect transmission of information in a variety of different forms, and is robust against the types of noise observed in culture.

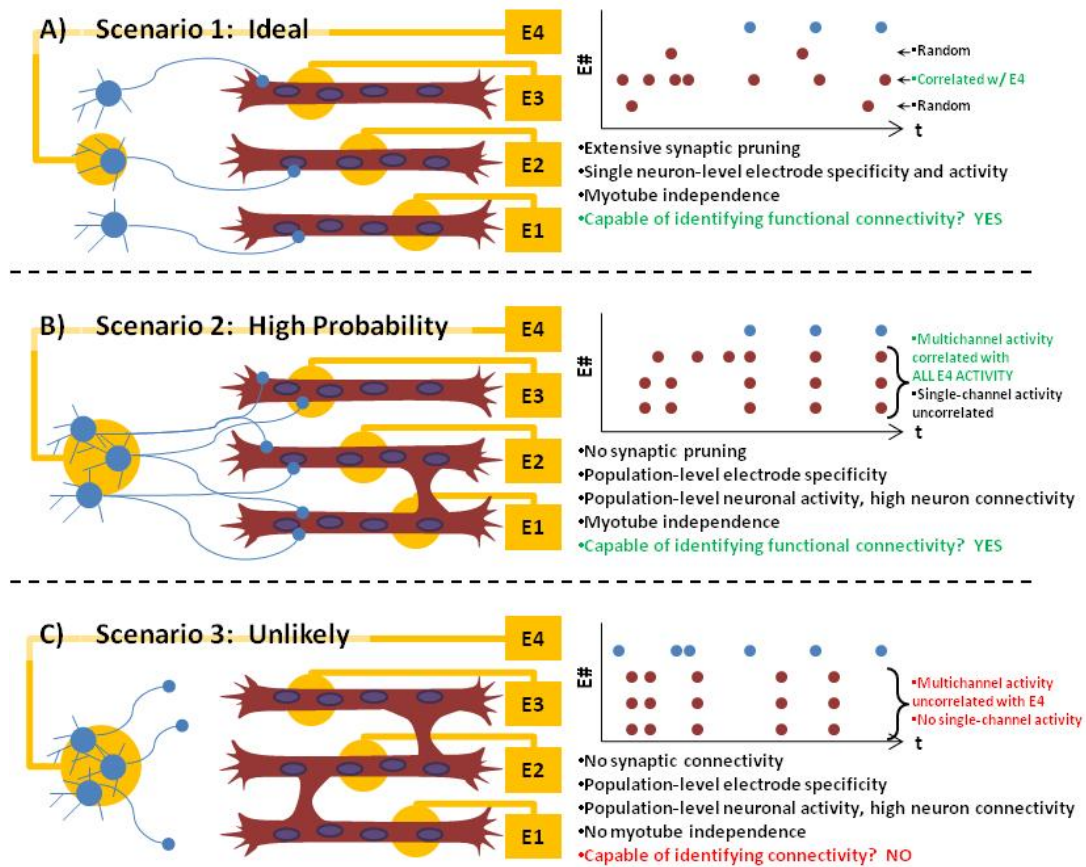


Figure 6.1-3. Myo-MEA coculture schematics demonstrating potential patterns of synaptic connectivity

Once mechanically stable cocultures have been developed, functional motor neuron-myotube association will be assessed in a two stage process in which correlated activity is analyzed before and after application of botulinum toxin or tubocurarine, selective presynaptic and postsynaptic NMJ blockers, respectively. In both stages, spontaneous bioelectric activity from the explant and myotubes will be observed, and the biological connectivity between units will be quantified using the algorithm developed in Aim 1. Because explant activity is only recorded on the central field electrodes regardless of neurite outgrowth, and because of the exclusion of myotubes from the central region

during the seeding process, we can assume that all activity in the wing regions originates from myotubes (Fig. 6.1-3 A-C – red points in raster plots) and all activity in the central region originates from the explant (Fig. 6.1-3 A-C – blue points in raster plots). In the wing regions we expect to see a mixture of single electrode activity (single myotubes located in a single trench) and multielectrode activity (myotube syncytia spanning multiple trenches) and in the central region we expect to see standard explant bursting. During periods of explant silence, spontaneous activity drives myotube activity, revealing the pattern of independent myotubes (Fig. 6.1-3 A-B – unaligned red points). However, during periods of explant bursting, additional patterns of myotube activity will emerge where multiple myotubes which had previously contracted independently will be driven synchronously by neuronal input from the explant (Fig. 6.1-3 B – vertically aligned red points). Synaptic connectivity between the explant and myotubes will therefore be detectable as a difference in myotube activation patterns during “explant-active” and “explant-silent” periods. This same analysis will be repeated following application of the NMJ blocker. Because both agents act selectively at the NMJ, spontaneous activity of both myotubes and the explant will be preserved but connectivity between them will be lost. Therefore, there will be no difference in myotube activation patterns between explant-active and explant-silent periods following the NMJ blockade. Because each culture can be tested before and after NMJ blockade, each culture is internally controlled.

These results would demonstrate that the myo-MEA can record EAPs from myotubes, and that their activity encodes a representation of information originating from a neuronal source, demonstrating that we have in essence reconstituted the neuromuscular system from its component cell types.

6 Appendices

6.1 Protocols

6.1.1 Myocyte Isolation and Culture Protocol:

Materials & Ordering Information Particular to this Procedure:

1. Concentrated Acetic Acid – (Sigma, 318590)
2. Calf Skin Collagen in 0.1 N acetic acid – (Sigma, C8919)
3. Collagenase D – (Roche, 11088858001)
4. Dispase II – (Roche, 10295825001)
5. CaCl_2 solution – (use lab stock)
6. Hams F-10 – (Gibco, 11550)
7. Fetal Calf Serum (FCS) – (use lab stock)
8. Horse Serum – (use lab stock)
9. Human bFGF – (Invitrogen, 13256-029)

Making Reagents and Solutions:

1. Make collagen adsorbed petri-dishes (only if none are already available) [234], or gelatin coated petri dishes [54]:
 - a. Make collagen solution, store at 4°C:
 - i. Add 1 ml concentrated acetic acid to 179 ml H_2O and sterile filter
(or whatever dilution takes you to 0.1 N)
 - ii. Add 20 ml 0.1% calf skin collagen in 0.1 N acetic acid
 - b. Incubate in plastic tissue culture dishes overnight at room temperature
 - c. Remove and **SAVE** collagen solution (they can be reused)
 - d. Rinse dishes in sterile H_2O and allow to air dry
 - e. Store at RT for up to 6 months

Procedure:

2. Harvest thigh muscles from E21 – P1 rat embryos:
 - a. If necessary, sack the mother rat according to standard procedures and remove embryos
 - b. Under a stereo microscope, remove the lower limb using dissecting tweezers and scissors. Place relevant muscle specimens in a drop of sterile dissociation medium (based on practical experience);
 - i. Gently grab the lower limb at the knee with one tweezer and cut the leg off as far toward the backbone as possible
 - ii. Try not to include abdominal wall or contents
 - iii. Remove the skin/fat layer by grabbing the leg with one tweezer, the skin/fat with the other and peeling off the skin
 - iv. Remove the foot at the ankle
 - v. Remove the relevant parts (intact, skinned ankle through hip) to another dish to keep moist
3. Dissociate Muscle Cells (sterile technique used from here on):
 - a. Finely mince tissue using a razor blade
 - b. Transfer to a 15 ml tube containing 2 ml collagenase/dispase solution along with 2 – 4 ml dissecting buffer
 - c. Add 60 μ L of CaCl_2 solution
 - d. Triturate with a 1000 μ L pipette
 - i. Note: cut off tip of pipette to make titrating easier
 - e. Shake cells and digestion solution in incubator for 20 min
 - f. Dilute digestion products (supernatant) in 25 ml PBS

- g. Centrifuge cells @ 300 RCF for 5 min, aspirate supernatant, and resuspend pellet in growth medium

4. Enrich for Myoblasts:

- a. Dilute cell suspension into 45 ml of growth medium and plate into T-75 flasks (pre-coated w/ collagen) – each dissection should require ~3 flasks
- b. Incubate @ 37°C, 5% CO₂ overnight
- c. Rinse 3X in sterile PBS to remove unattached debris (RBCs and mature muscle cells not capable of attaching)
- d. Incubate in sterile PBS for 20 min
- e. Shake cells off the bottom of the flask by tightening the cap and striking it sideways against your palm
- f. Centrifuge the cell suspension @ 300 RCF for 5 min and resuspend in appropriate medium
- g. Freeze cells according to freezing protocol, or plate immediately for use

5. Confirm ability to Differentiate in Culture:

- a. Myoblasts can be identified by staining for desmin. Otherwise observing their differentiation into myotubes also confirms their ability to differentiate. Multinucleated myotubes should form starting within a few days, and should continue forming for up to a week. Spontaneous twitching should begin around 1 week into differentiation.
- b. Replace growth medium with fusion medium
- c. Replace fusion medium every day

6. Growth for experiments:

- a. Experiments with muscles cells in co-culture should be performed on laminin adsorbed glass coverslips

- b. Laminin adsorbed at 20 ug/ml for 1 hr @ 37°C.
- c. Rinse w/ sterile H₂O
- d. Plate myoblasts at a density from 70,000 – 100,000 cells/cm² to maximize fusion [54] (200,000 on MEAs)
 - i. When plating, use Neurobasal for cell differentiation or Growth Medium otherwise

Other topics and additional techniques to improve the myoblast yield from isolation steps, including the use of Ara-C to eliminate fibroblastic contamination, can be found in Daniels, et. Al, 2000 [88].

6.1.2 Freezing Myotubes for “Long-Term” Storage and Thawing for Use:

Materials & Ordering Information:

1. Myotubes
2. DMSO (Use Lab Stock)
3. Myocyte growth medium (GM)

General Info:

1. Cell suspensions should be frozen @ ~2e6 cells/ml
2. Freezing medium is myocyte GM + 7% DMSO v/v
3. There are no transitional temperature steps, simply place cells directly in -80°C

Freezing Procedure (performed the day after cells are isolated, and have been growing overnight on a culture vessel):

1. Detach cells from surface of culture vessel according to the standard practices and pellet:
 - a. The following should be performed on non-confluent cultures only (otherwise just do this with all the cells, not the selectively detached ones)

- b. Remove GM and rinse 2x with sterile PBS to remove non-adherent debris (blood cells, myocyte debris, etc.)
 - c. Cover with 2/3 culture vessel volume of sterile PBS, tighten cap and place on the shaking incubator @ 60 rpm for 5 min @ 37°C
 - d. Check periodically for detachment of ~70% of cells (myocytes adhere less strongly to the substrate and therefore detach first)
 - e. Alternatively, instead of steps (c) and (d), cover bottom of culture vessel with sterile PBS and place in 37°C incubator for 20 min
 - f. Remove the PBS with these cells (myocytes) to a 15 ml conical and centrifuge @ 300 RCF for 5 min
4. Resuspend myocytes in GM to appropriate volume such that final cell concentration is ~2e6 cells/ml:
- a. Resuspend pellet in 2 or 3 ml GM
 - b. Dilute 50 ul of this in 450 ul of GM, and add 500 ul Trypan blue (1:20 total dilution)
 - c. Wait 3 min and count live cells (unstained ones) in the hemacytometer
 - d. Add appropriate amount of medium to bring suspension to ~2e6 cells/ml
5. Add DMSO, mix, partition into cryovials, and transfer to -80°C
- a. Final concentration of DMSO should be 7% v/v
 - b. Mix gently by inverting several times (DMSO destabilized cell membranes)
 - c. Most cryovials contain up to 1.8 ml fluid, do not overfill

Thawing Procedure (performed the day before cells are needed):

1. Remove myocyte vials from freezer and thaw in 37°C H₂O bath:

- a. Stand there while this happens, leaving them in the freezing medium in the bath significantly reduces cell viability and function (DMSO is so bad for the cells)
2. Remove residual freezing medium by centrifugation:
 - a. Dilute contents of vials in ~20 ml sterile PBS, and mix gently
 - b. Centrifuge @ 300 RCF for 5 min, and aspirate medium
3. Plate onto culture vessel for intermediate culture prior to plating for actual culture
 - a. Resuspend pellet in GM and plate at 75,000 – 100,000 cells/cm²
 - b. Incubate overnight
 - c. Prior to re-plating under experimental conditions, rinse surface 2X with sterile PBS to remove dead cells and extraneous debris
 - i. When plating, use Neurobasal for cell differentiation or Growth Medium otherwise

Notes:

1. It is unclear how long the cells last at -80°C, so do not count on storing more than you will likely use in the next couple of weeks

6.1.3 F-10 Based Myocyte Growth Medium:

Materials & Ordering Information:

1. Ham's F-10 Medium – (Gibco/Invitrogen - 11550-043 (500 mL @ \$18.50))
4. B-FGF – (PeproTech, Catalog#: 100-18B, Lot#: 1207CY08-1)
5. Fetal Calf Serum (FCS) – (Use Lab Stock)
6. Pen/Strep – (Use Lab Stock)

Procedure:

1. Recipe [234]:
 - d. 80% Ham's F-10

- e. 20% FCS
- f. 1% Pen/Strep
- g. 2.5 ng/ml b-FGF

6. Protocol:

- a. Mix F-10 from powder according to their directions
- b. Remove 100 ml of F-10 from the 500 ml container to a separate sterile container. Save for later use
- c. Add 100 ml of FCS
- d. Add 5 ml of pen/strep
- e. Add 50 ul of B-FGF stock (usually at 25 ug/ml)
- f. Sterile filter to a new container (required because a portion of this procedure takes place outside the hood)

7. Store at 4°C. Stable for at least 1 month

6.1.4 Neurobasal (NB) Medium:

Materials & Ordering Information:

- 1. NB base (Use Lab Stock)
- 2. B27 Supplement (Use Lab Stock)
- 3. L-glutamine (Sigma, G3126)
- 4. Pen/Strep (Use Lab Stock)
- 5. Beta-mercaptoethanol (Aldrich, M6250)
- 6. Glutamax [Invitrogen – 35050-061 (\$25.20)]

Recipe-1:

- 1. 97% Neurobasal Base Medium
- 2. 2% B27 Supplement (or NS21 supplement)
- 3. 1% Pen/Strep

4. 69 ug/ml L-Glutamine (0.4 mM)
5. 1.84 nl/ml beta-mercaptoethanol

Recipe-2:

1. 96% Neurobasal Base Medium
2. 2% B27 Supplement (or NS21 supplement)
3. 1% Pen/Strep
4. 1% Glutamax

Procedure-1:

1. Add 10 ml of B27 supplement to 500 ml of NB base medium
2. Add 5 ml of Pen/Strep
3. Add 34.5 mg of L-glutamine
4. Remove 10 ml of mixture to a secondary container
 - a. Add 7.3 ul of beta-mercaptoethanol to this secondary container and mix well
5. Take 1.24 ml of the diluted beta-mercaptoethanol and add it back to the NB
6. Mix well, and sterile filter to a new container
7. Store @ 4°C, PROTECT FROM THE LIGHT (wrap in foil)

Procedure-2:

1. Remove 20 ml of unmixed NB
2. Add 10 ml of B27 supplement (or NS21 supplement)
3. Add 5 ml of Pen/Strep
4. Add 5 ml of Glutamax
5. Mix well, and sterile filter to a new container (does not need to be sterile filtered if everything is done in the hood)
6. Aliquot into 50 mL tubes and...

7. Store @ 4°C, PROTECT FROM THE LIGHT (wrap in foil)

Notes:

1. Other recipes call for Glutamax instead of L-glutamine to avoid toxic breakdown products. If this is the case you can exclude the beta-mercaptoethanol from the recipe. Invitrogen also recommends supplementing with glutamic acid for initial seeding steps, but our lab tried this and said it didn't make any difference.

6.1.5 Collagenase – Dispase Preparation Protocol:

Materials & Ordering Information:

1. Collagenase D – (Roche, 11088858)
2. Dispase II – (Roche, 91011622)
3. PBS – (Use Lab Stock)
4. CaCl₂ – (Use Lab Stock)

Procedure:

1. Recipe [234]:
 - a. 1.5 U/ml collagenase D
 - b. 2.4 U/ml dispase II
 - c. 2.5 mM CaCl₂
2. Prepare solution at 2X final concentrations and store at -20°C
 - a. Prepare CaCl₂ solution in PBS to a final concentration of .25 M
 - i. Add 1.83 grams of CaCl₂ dehydrate (FW 147) to 50 ml dH₂O
 - ii. Shake until dissolved
 - iii. Sterile filter to a new conical tube
 - b. Reconstitute collagenase D (stock usually ~.25 U/mg)
 - i. Reconstitute to 2X desired working concentration (~3.0 U/ml)
 - ii. Add 1 ml of PBS to container of 100 mg collagenase

- iii. Remove to a sterile conical tube and add 8 more ml of PBS
 - iv. Sterile filter, aliquot into 1 ml portions and freeze at -20°C
 - c. Reconstitute dispase (stock usually at 0.5 U/mg)
 - i. Reconstitute to 2X concentration (~5.0 U/ml)
 - ii. Reconstitute 200 mg of dispase II in 20 ml PBS w/o Ca⁺⁺/Mg⁺⁺
 - iii. Sterile filter, aliquot into 1 ml portions and freeze at -20°C
- 3. Prepare immediately before use from 2X frozen stock.
 - a. Mix 1 aliquot dispase solution with 1 aliquot collagenase solution with 2 ml of dissecting buffer containing the tissue slurry
 - b. Add 60 ul of the CaCl₂ solution to activate the enzymes

Notes:

Protocol modified and updated based on personal experience and experimentation

6.1.6 Immunofluorescence Staining Protocol:

Materials:

- 1. Cells to be stained
- 2. Primary Antibodies
- 3. Secondary Antibodies
- 4. Rhodamine Phalloidin [Fischer, NC9817931]
- 5. Triton X-100 [Sigma, T9284]
- 6. Bovine Serum Albumin – (BSA) [Sigma, BP1605100]
- 7. Syringe Filter [Use Lab Stock]

Protocol:

If you don't already have blocking and fixing solutions

- 1. Make Blocking Solution (“neuro-block”)

- a. 2.0% Normal Goat Serum (or FBS, or BSA depending on the needs of the particular Abs to be used and experimental set-up)
- b. 2.0% Triton solution (normally at 10% concentration)
- c. 1.0% Sodium Azide solution (normally at 2.0% itself)
- d. All mixed up in PBS
- e. For 25 ml:
 - i. 23.75 ml PBS
 - ii. 250 ul sodium azide solution
 - iii. 0.5 ml Triton solution
 - iv. 0.5 ml Normal Goat Serum

2. Obtain Fixing Solution (methanol) from -20°C refrigerator

Else:

1. Remove cell medium
2. Wash 3x with 1X DPBS (w/ Ca⁺⁺ & Mg⁺⁺) [PBS, can be nonsterile]
3. Fix cells:
 - a. Cover cells in methanol.
 - b. Incubate for 15 min at -20°C
 - c. Remove methanol by aspiration (by dumping if you are fixing fragile structures)
4. Wash 3x with 1X DPBS (w/ Ca⁺⁺ & Mg⁺⁺) [PBS, can be nonsterile]
5. Make antibody solutions by diluting according to instructions.
 - d. Make in neuro-block without Triton X-100 (or w/ Triton X-100, this shouldn't effect anything), 1:200 dilution
 - e. Make enough to fill appropriate number of wells
6. Add Primary antibody solutions:

- f. Cover cells with Primary antibody solution (see step 7),
- g. Incubate for 3 hr @ RT
- h. Remove and **SAVE** your primary Ab
- 7. Wash 3x with 1X DPBS (w/ Ca++ & Mg++) [PBS, can be nonsterile]
 - i. Wait 5 min between each wash, agitate as little as possible
- 8. Make Secondary antibody solutions – (protect them from light using foil to avoid photobleaching):
 - j. Make in neuro-block with or without Triton X-100, 1:200 dilution
 - k. Make enough to fill appropriate number of wells
- 9. Add Secondary antibody solution – (protect them from light using foil to avoid photobleaching):
 - l. Cover cells with Secondary antibody solution (see step 10) for 1 hr @ RT
(ensure cell plates are covered in foil to avoid photobleaching)
 - m. Remove and **SAVE** your secondary Ab
- 10. Wash 3x with 1X DPBS (w/ Ca++ & Mg++) [PBS, can be nonsterile]
- 11. Store appropriately depending on conditions:
 - n. Store at 4°C hydrated in 1X DPBS w/Ca++ & Mg++ – (protect them from light to avoid photobleaching)
 - o. Or if the sample has been prepared on a glass slide, use an antifading agent to mount the coverslips to a glass slide

6.1.7 Hoechst Staining Protocol:

Materials & Ordering Information:

1. Hoechst Nuclear Stain (Sigma, Fisher, pretty much anyone)

Procedure:

1. Prepare stock Hoechst solution:

- a. Stock solution made at ~2 mM (~1 mg/ml) in dH₂O [235]
 - b. Most Hoechst stains will precipitate in PBS at this concentration
 - c. Even in dH₂O it may be difficult to get stain into solution, stirring and heat may be necessary, or addition of DMSO
2. Dilute stock solution to make working solution:
 - a. Working solution at ~2 μ M (~1 μ g/ml)
 - b. Dilute stock solution 1:1000 in the desired solution (PBS for fixed cells, medium for live cells)
 - c. Protect from light
3. Incubate cells:
 - a. 30 min @ RT for fixed and permeabilized cells
 - b. 1 hr @ 37°C in incubator for live cells
 - c. Protect from light
 - d. Remove and SAVE Hoechst solution
4. Wash (in PBS):
5. Store (at 4°C)

6.1.8 Alpha-Bungarotoxin Labeling Protocol:

Materials & Ordering Information:

1. Alpha-Bungarotoxin (Invitrogen, B13422)
2. PBS (Use Lab Stock)
3. Growth Medium/Treatment medium
4. Sodium Azide (Use Lab Stock)

Procedure:

1. Reconstitute and store aB toxin [236]:

- a. Reconstitute 500 ug of fluorescently labeled aB toxin in 0.5 ml sterile dH₂O
 - b. Add sodium azide to a final concentration of 2mM:
 - i. Stock sodium azide is typically at 2% (or .3M)
 - ii. Add 3 ul of sodium azide solution to reconstituted aB toxin
 - c. Aliquot at 25 ul and 10 ul per tube and store at -20°C – protect from light
 - i. The reconstituted stock can be stored at 2-6°C if it is going to be used in the short-term
 - ii. Avoid repeated freeze-thaw cycles, can store short time @4°C
2. Make aB working solution:
- a. aB toxin stock normally at 1 mg/ml, while working stock is at 5 ug/ml [237] (other papers use an even lower concentration [56, 88, 238])
 - b. Remove an aliquot of aB toxin from the -20°C freezer where they are stored
 - c. Dilute aB toxin 1:200 in desired medium (whatever you are going to incubate the cells in, probably the same as the medium they were just in)
 - d. 25 ul will make 5 ml of working solution
 - e. 10 ul will make 2 ml of working solution
3. Treat cells:
- a. Incubate cells in working solution for 1 h [88, 213, 237, 238] (Other procedures incubate for longer, or have more involved washout steps [56], but this should work)
 - b. Rise 3X in medium (same type as whatever you were using)
 - c. Replace cells in medium and either return to incubator or proceed to fixation [238]

4. Fix Cells:

- a. Rinse cells in PBS
- b. Place cells in 4% paraformaldehyde for 30 min @ RT [88, 238] (other groups use more complex fixation procedures [56], but this should work)
- c. Rinse cells 3X in PBS, careful not to wash the cells off the surface
- d. Store in PBS until you stain for other proteins (see IF staining protocol)

6.1.9 Substrate Regeneration (Electrode & Topographical):

Materials & Ordering Information:

1. Trypsin (Invitrogen, 15090-046)
2. Tergazyme (Use Lab Stock)

Substrate Cleaning Procedure:

1. Biologically remove adherent cells from surface:
 - a. Incubate for 1 hr (or longer as needed) in 2.5% trypsin solution @ 37°C
 - b. Aspirate trypsin, and rinse surface with PBS repeatedly using 1000 µL pipette
 - c. Inspect under a microscope for remaining cells, and repeat above steps as necessary until all or the desired amount of cells and debris have been removed
2. Chemically clean surface:
 - a. Rinse the surface with Tergazyme solution using a squirt-bottle
 - b. Tergazyme solution may be left on the surface for short incubation periods, but not overnight
 - c. Inspect under a microscope for remaining cells, and repeat above steps as necessary until all or the desired amount of cells and debris have been removed

3. If necessary, physically clean surface:
 - a. Remove cells and debris that won't detach chemical by gently scrubbing the surface with a cotton swab
4. Sterilize surface (NOTE: Do not perform this step until cells and biological material have been removed from the surface as incubation in alcohol will fix these materials to the electrode/topographical substrates):
 - a. Soak in EtOH for 1 Hr
 - b. Remove to a sterile container and allow to air dry (preferably in the hood)
 - c. Use soon after to avoid recontamination

PDMS Stamp Cleaning Procedure:

1. Wipe any debris that may be present on the bottom of the PDMS mold.
2. Sterilize surface:
 - a. Soak in EtOH for 1 Hr
 - b. Remove to a sterile container and allow to air dry (preferably in the hood), making sure the contact surface is clean and dry
 - c. Use soon after to avoid recontamination

6.1.10 Plasma Generator Protocol:

Materials:

1. Plasma generator
2. Substrate to be modified
3. Others

Protocol:

1. Turn on and warm up the machinery if necessary (requires a 20 min warm-up from a cold-start):
 - a. Turn both gas tanks on (valves turned several turns to the left)

- b. Turn on the vacuum pump
 - c. Turn on the generator
- 2. Sign-in on the usage roster
- 3. Select a program to run, or create a new program if necessary (Note: Always check the program parameters before you run any samples!):
 - a. Programs are not assigned to people or labs – you must check you program before each time you run it
 - b. Programs 1 & 9 are used for maintenance – DON'T CHANGE THESE
- 4. Plasma treat the sample:
 - a. Place sample on the center tray (Note: Altering tray configuration can be used to change surface treatment (ie, ion deposition vs plasma treatment))
 - b. Press “Start” to run treatment cycle
 - c. Monitor BP/RP during the treatment. This value should stay below 5. If it increases over 5, stop the treatment
 - d. Wait for cycle to run and chamber to depressurize before removing sample. Chamber is depressurized when a slight change in depressurizing noise is heard. If the chamber does not depressurize fully and the door can not be opened, bleed the remainder of pressure using the <Bleed> button
- 5. Close down the machinery:
 - a. Record the “Gas #” and “Press” readings at the end of the cycle - (should be in the range of the others on the sign-in sheet)
 - b. Turn off gas valves
 - c. If you are the last user of the day, turn off generator and pump

Notes on Machine Use:

1. Left dial:
 - a. Use <L Disp> button to select feature to read
 - b. Having the <Set> button depressed causes you to read what the feature is currently set to
 - c. Change settings while the <Set> button is depressed by using the <Incr.> and <Decr.> keys
 - d. If the <Set> button is not depressed the dial reads the current level of whatever feature is selected
2. There are effectively only 4 variables which can be altered:
3. Time (Left dial, option 4)
 - a. Set directly using cycle button (L Display) and <Set> buttons to select setting, and <Incr/Decr> buttons to change
4. Power (Left dial, option 2)
 - a. Set directly using cycle button (L Display) and <Set> buttons to select setting, and <Incr/Decr> buttons to change
5. Pressure (Right dial, set value by controlling valve opening %)
 - a. Pressure is changes using the gauge on the right
 - b. The gauge reads valve % open, not pressure. This number drives the chamber pressure. Actual pressure readings are obtained at the end and recorded
 - c. CO₂ (Gas 1) should be set to 40% when used
 - d. O₂ (Gas 2) should be set to 60% when used
6. Gas selection
 - a. Gas 1 – CO₂
 - b. Gas 2 – O₂

- c. Right gauge reads how much valves are open. The combination of gasses will result in final pressure (read at end)
7. Set the variables required for your experiment using the <R/L Display> buttons and <Set> button to select setting, and <Incr/Decr> buttons to change
- a. Endpt – doesn't change (100)
 - b. DC Bias – doesn't change (0)
 - c. BP/RP – doesn't change (80)
 - d. Time – as per experiment
 - e. Power – as per experiment
 - f. Pressure – (changed on right display as described above)
 - g. Gas selection – (changed on right display as described above)
 - h. See below for example programs/settings

Example Settings:

Power – 50 (Watts)

Endpt – 100

Time – 120 (seconds)

DC Bias – 0

BP/RP – 80

Gas 2 – 60

6.1.11 SU-8 Photolithography Protocol:

Materials & Ordering Information:

1. Substrate
2. Acetone
3. Isopropanol
4. DI water

5. SU-8 Photoresist
6. Photoresist Developer

CRITICAL STEP: Work in small batch sizes (2 substrates at a time) to prevent the duration of processing steps from effecting the treatment each substrate receives.

Substrate Pretreatment:

1. Set oven temp to 130.
2. Wipe substrate of any residue or dust using acetone and dust-free cloth.
3. Clean in acetone.
 - a. Soak substrate in acetone for ten minutes, rinse in isopropanol.
4. Clean in isopropanol.
 - a. Soak substrate in isopropanol for ten minutes, rinse the substrate with DI water.
5. Clean in DI water.
 - a. Soak substrate in DI water for ten minutes, rinse with DI water.
 - b. Using filtered air, blow dry the substrate until it is dry.
6. Clean up when done pre-treating the substrate.
 - a. Place used chemicals in appropriate bins.
 - b. Return containers to appropriate location.
 - c. Ensure all surfaces are dry and clear of chemicals.

PAUSE POINT: Cleaned samples can be left overnight, when appropriately stored, and used the next morning starting from this point.

7. Dehydrate sample.
 - a. Place the substrate in the oven at $\sim 130^{\circ}\text{C}$ for 30 minutes.
 - b. Cool to RT after baking by opening the oven door.

- c. Do not allow sample to sit in atmosphere for long periods of time at RT, they will collect moisture.

Coat with SU-8:

8. Start the soft-bake program on the programmable hot plate (currently program # ____)
9. Set up spinner (run recipe # 1 to give ~40 μm thick layer).
 - a. Turn on spinner controller if necessary and press recipe on the keypad. When prompted with a screen that reads "Recipe: _", enter the recipe for the corresponding thickness of the SU-8. The following chart shows the appropriate spinner recipe for each thickness;

Photoresist	Thickness (μm)	Recipe	Spin Speed
SU-8			
2025	25	0	3000
SU-8			
2025	41	1	2000
SU-8			
2025	75	2	1000

- b. Remove chuck from spinner and line the spinner bucket with aluminum foil (the chuck is easily removed by pulling up).
- c. Get a piece of aluminum foil large enough to cover the bucket and its sides. Make a small hole in the middle of the foil and lay it inside the bucket.

- d. Form the aluminum foil around the edge of the bucket so that SU-8 will not splatter on the walls. Make sure there is no foil going into the vacuum hole in the center.
- e. Place appropriate chuck on the spinner (make sure the substrate covers the entire chuck to prevent SU-8 splatter).

CRITICAL STEP: Use fresh SU-8, from a clean container, that has had time to equilibrate to room temperature. I suggest aliquoting the SU-8 you are going to use the evening prior to coating.

10. Coat the substrate with SU-8.

- f. Place the substrate on the center of the chuck and turn on the vacuum so that the substrate does not move.
- g. Apply 1 mL SU-8 per inch substrate (for 2 in glass squares this will be ~2-3 full droppers full.
 - i. Apply in the center of substrate, distributing in an even circle centered on the center of the spinner chuck.
 - ii. “Suck” bubbles back into the dropper until no bubbles exist, or “pop” them using a needle and or blade.
- h. Approximately 2-3 droppers full of SU-8.

11. Spin off excess SU-8.

- i. Press the “start” button, and make sure the vacuum is toggled off before removing the substrate after spinning.

12. Move chip IMMEDIATELY to warming programmable hotplate.

- j. By this time the hotplate should be several degrees above RT at least, and on its way to a stable temp in the range of 45-65 deg C.

13. Clean up after using the spinner.

- a. Remove foil from spinner bucket and discard.
- b. Clean any residue on spinner.
- c. Make sure the vacuum switch is turned off.

Soft Bake:

- 14. Allow soft-bake program on the programmable hotplate to run to completion.
 - a. See last page for a description of programmed heating/cooling steps (currently program 4)
- 15. Remove substrate from hot-plate to next processing step or appropriate storage after completion of soft-baking program.

PAUSE POINT: SU-8 coated substrates may be left for 2 or 3 days at RT before the next processing step.

Exposure:

- 16. Turn EVG 620 on.
 - b. Turn on the main switch (red) on EVG 620, key must be in “off” position.
 - c. Turn on the lamp power, located under the bench. Then press “start” to fire lamp.
 - * The lamp must be heated ten minutes prior to usage.
 - d. Turn on the key switch.
 - e. Turn on the PC power, located under the bench in the cabinet.
 - f. Run EVG 620 Software
 - i. Log in.
 - ii. Use File-Open to find the appropriate recipe, located in “C:\Program Files\EVG\EVG6XX\Recipes\SU8\Glass”.
- 17. Run the appropriate recipe (currently “40um_SU8_Glass_CL_V04.rcp”)
 - g. Exposure should be $\sim 250 \text{ mJ/cm}^2$.

- h. Press “Run,” then follow the instructions on the screen.
 - i. Some substrates may require alignment.
 - j. Use black background when exposing to prevent back scattering.
18. Store substrates on counter while processing, and move substrates to programmable hotplate all at once before running the post exposure bake program.
19. Shut down EVG 620.
- a. Turn off PC.
 - i. Close EVG Software and shutdown Windows.
 - b. Turn off the key switch.
 - c. Cool lamp (**CRITICAL STEP**)
 - i. Switch off the lamp power, then turn it back on.
 - ii. Wait 10 minutes, then switch off the power again.
 - k. Turn off the main switch.

Post Exposure Bake:

20. Move all substrates to programmable hotplate surface.
21. Run post exposure bake program (currently program # 2)
- a. See final page for a description of heating/cooling programs

PAUSE POINT: Following PEB, appropriately stored substrates may be left at RT for 1 day waiting to be developed.

Develop:

22. Immerse substrate in SU-8 Developer.
- a. Agitate so that the developer removes exposed SU-8.
 - b. Ideal developing time is found in the chart below.

Photoresist	Thickness (μm)	Develop	Time
<hr/>			

(min)		
SU-8 2025	25	4
SU-8 2025	41	5
SU-8 2025	75	7

23. Remove the substrate and rinse with isopropanol.

- c. If large amounts of cloudy white fluid are apparent, return to developer for another minute

24. Examine under the microscope.

- d. Inspect to see if unexposed material has been successfully removed from features.
- e. Return to developer if significant material is left.

25. Blow dry with filtered air or allow to dry on a counter-top

Hard Bake (Annealing):

26. Place substrates on programmable hotplate surface.

27. Run annealing program (currently program # 3).

Recommended Treatment (as of 2010-03-05):**Soft Bake:**

Ramp:	Temp:	Time:	Exposure:
450	45	1 hr	5 X 45 mJ/cm ²
120	95	10 min	
120	45	10 min	
120	95	10 min	
120	45	10 min	
120	95	2 hr	
60	25	1 hr	

Post Exposure Bake:

Ramp:	Temp:	Time:
120	30	1 hr
120	50	10 min
120	65	10 min
120	95	30 min
60	25	1 hr

Hard Bake:

Ramp:	Temp:	Time:
120	150	1 hr
60	25	1 hr

6.2 Visual Twitch Analysis Online Supporting Material**6.2.1 Description of Success and Failure Metrics**

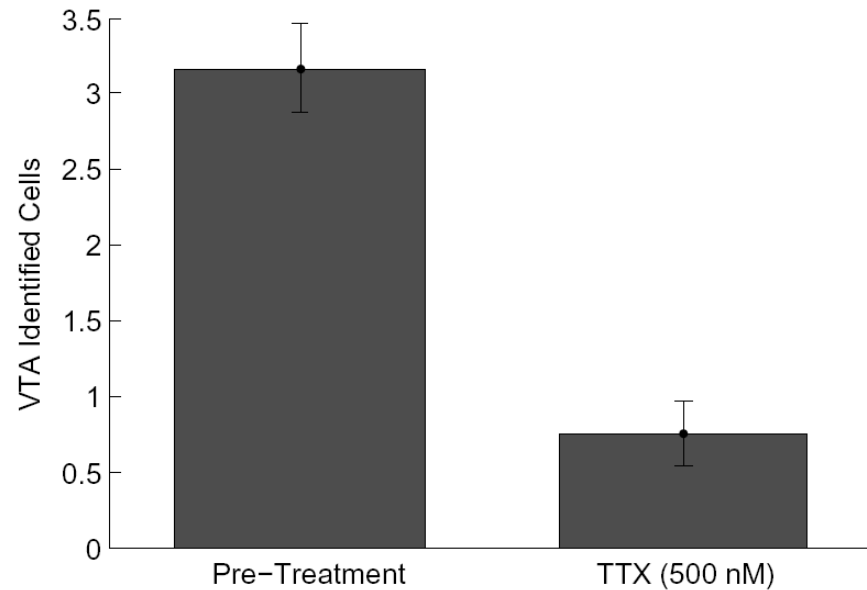
Success Metric:	Rationale:	Description:
Success Spread	An ideal W_{XY} cluster contains nodes where the	A measure of how obviously the W_{XY} can be identified

(S1)	<p>correlation between $\delta_{XY}(t)$ and the cluster's $\delta_K(t)$ function is very high relative to the other $\delta_K(t)$ functions. This is indicative that the $\delta_{XY}(t)$ functions for the W_{XY} in the cluster match the appropriate $\delta_K(t)$ function very closely and are much less similar to the other $\delta_K(t)$ functions.</p>	<p>as belonging to one particular cluster. It is calculated as the extent to which the correlation coefficient for each $\delta_{XY}(t)$ function and the $\delta_K(t)$ function to which it has been matched is greater than the average correlation coefficient between that $\delta_{XY}(t)$ function and the other $\delta_K(t)$ functions, averaged over the whole viewing field.</p>
Area Coverage	<p>Encourage the algorithm to select for $\delta_K(t)$ functions that explain a broader area, rather than a very small area that is more highly correlated, and is meant to reduce the frequency of multiple sections of the same myotube being labeled as separate clusters.</p>	<p>The percentage of the interrogation windows that are finally assigned to clusters. This number increases with the number of W_{XY} windows included in all clusters.</p>
Cell Number	<p>Encourages the VTA algorithm to find all cells and not simply settle for identifying only the obvious ones.</p>	<p>The number of cells that the algorithm identifies divided by the total number of possible cells (i.e., the maximum value of K).</p>
(S3)		

Failure Metric:	Rationale:	Description:
-----------------	------------	--------------

Correlation Difference (F1)	A measure of the difference in the correlation coefficient between all $\delta_{XY}(t)$ functions in a cluster and the cluster's corresponding $\delta_K(t)$ function and the average correlation coefficient of the same $\delta_{XY}(t)$ functions with the other $\delta_K(t)$ functions.	Rather than being averaged for every W_{XY} over the whole image, as in "Success Spread," it is instead averaged for each cluster. Because this would be a measure of success similar to the success metric "Success Spread," F_2 is calculated as 1 minus this amount.
Scatter (F2)	Myotube contractions tend to cause changes in pixel intensity in a highly localized fashion. Therefore, a high density of nodes in a cluster is more likely caused by myotube contraction than nodes spread over a larger area with little activity in the space between nodes of the same cluster.	The average edge length between linked nodes in the identified cells.
Missed Twitch (F3)	Reduce the overall fitness of cluster sets that fail to take into account all the observed contractions.	The average of the $E_{XY}(t)$ functions of all W_{XY} windows that are observed to twitch but are not eventually assigned to clusters. The more contractile activity excluded, the greater this handicap.

6.2.2 VTA Program Analysis of TTX Treatment on Spontaneous Contractility in Skeletal Myotubes



Supplemental Figure 1 Spontaneous contractile activity in myotubes before and during treatment with tetrodotoxin (TTX) at 500 nM. N = 12

Skeletal myotubes were isolated and cultured as described in the manuscript section titled “Methods: Cell Culture.” Twelve videos of myotube behavior were acquired at DIV 14 by selecting random locations in the culture and recording videos as described in the manuscript section titled “Methods: *In Vitro* Video Capture and Synthetic Data Generation.” The medium in these cultures was then exchanged for medium containing 500 nM tetrodotoxin (TTX), and the video acquisition procedure was repeated. Data were analyzed using the VTA algorithm as described in the manuscript.

TTX is a reversible sodium channel blocker known to block impulse propagation in excitable membranes, and therefore, blocks contractile activity in myotubes.

Consistent with the results shown in Figure 4A, there is a slight bias in analysis, resulting in the identification of 0.75 cells per video in the TTX-treated case. Review of these videos revealed that this activity is a misclassification of lighting artifacts and other sources of

culture noise and that all contractile activity is, in fact, silenced by the exposure to TTX. However, despite the slight off-set, the VTA algorithm is able to robustly identify a change in contractile activity between the treated and untreated cases.

6.3 VTA MATLAB CODE

```
function VTA

% Clear the working area.

clc;

clear all;

close all;

% Open up the psuedo-GUI to walk you through program use

save_path = [];

answer1 = [];

answer2 = [];

answer3 = [];

button1 = questdlg('Run VTA step-by-step or all-at-once','', 'step-by-step', 'all-at-once', 'step-by-step');

if strcmp(button1, 'step-by-step');

    button2 = questdlg('Select VTA Process to Run','', 'Step 1', 'Step 2', 'Step 3', 'Step 1');

    if strcmp(button2, 'Step 1');

        VTA_step1(button1, answer1);

    elseif strcmp(button2, 'Step 2');

        VTA_step2(button1, answer2, save_path);
```

```

elseif strcmp(button2,'Step 3');
    VTA_step3(button1,answer3,save_path);
end
elseif strcmp(button1,'all-at-once');

prompt={'Number of trials (J):',...
        'Number of horizontal and vertical divisions (N):',...
        'Black/white conversion threshold (Tb)'};
name='Image Processing Parameters';
numlines=1;
defaultanswer={'3','40','auto'};
options.Resize='on';
options.WindowStyle='normal';
options.Interpreter='tex';
answer1=inputdlg(prompt,name,numlines,defaultanswer,options);

prompt={'Spike threshold:',...
        'Enter the minimum # of ICs to look for (K_m_i_n):',...
        'Enter the maximum # of ICs to look for (K_m_a_x):'};
name='Signal Processing Parameters';
numlines=1;
defaultanswer={'1.96','1','10'};
options.Resize='on';

```

```

options.WindowStyle='normal';
options.Interpreter='tex';
answer2=inputdlg(prompt,name,numlines,defaultanswer,options);

prompt={'Correlation threshold:',...
        'Length threshold',...
        'Area threshold',...
        'Triangle threshold',...
        'Node threshold'};
name='Cost-benefit Parameters';
numlines=1;
defaultanswer={''.6','50','.2','15','10'};
options.Resize='on';
options.WindowStyle='normal';
options.Interpreter='tex';
answer3=inputdlg(prompt,name,numlines,defaultanswer,options);

[save_path] = VTA_step1(button1,answer1);
disp(save_path);
VTA_step2(button1,answer2,save_path);
VTA_step3(button1,answer3,save_path);
end

```

```

clc;

clear all;

close all;

%=====
%=====

function [save_path] = VTA_step1(button1,answer1)

% Create the _ImageInfo output, saved for future analysis.

if strcmp(button1,'step-by-step');

    prompt={'Number of trials (J):',...

        'Number of horizontal and vertical divisions (N):',...

        'Black/white conversion threshold (Tb)'};

    name='Image Processing Parameters';

    numlines=1;

    defaultanswer={'1','25','auto'};

    options.Resize='on';

    options.WindowStyle='normal';

    options.Interpreter='tex';

    answer=inputdlg(prompt,name,numlines,defaultanswer,options);

elseif strcmp(button1,'all-at-once');

    answer = answer1;

```

```

end

J_max = str2num(answer{1});
N_0 = str2num(answer{2});
if isempty(str2num(answer{3}));
    Tb_0 = answer{3};
else
    Tb_0 = str2num(answer{3});
end

%Calls sub-routine that identifies and locates videos to be analyzed. The
%program then steps through this list analyzing each video.
[pathname filename save_path] = build_filelist_imageprocess;
waitbar_vid = waitbar(0,['Currently Analyzing ' num2str(0) ' of ' num2str(size(filename,2)) ' Videos'],'Position',[480 390 270 60]);
for kkk = 1:size(filename,2);

    waitbar(kkk/size(filename,2),waitbar_vid,['Currently Analyzing ' num2str(kkk) ' of ' num2str(size(filename,2)) ' Videos']);
    waitbar_trial = waitbar(0,['Trial Number ' num2str(0) ' of ' num2str(J_max) ' Trials'],'Position',[480 300 270 60]);

    %Clear data from old movie and use a sub-routine to load a new movie
    %for analysis. To conserve memory, only one movie is loaded at a time.
    clear mov m n;
    [mov n] = raw_data_gen(filename,pathname,kkk);

```

```

for J = 1:J_max;

    waitbar(J/J_max,waitbar_trial,['Trial Number ' num2str(J) ' of ' num2str(J_max) ' Trials']);

    [N Tb] = step1_parameter_gen(N_0,Tb_0);

    [I_0_temp del_XY_temp E_XY_temp] = del_XY_gen(mov,n,N,Tb);

    I_0 = I_0_temp;

    del_XY{J} = del_XY_temp;

    E_XY{J} = E_XY_temp;

    N_out{J} = N;

    Tb_out{J} = Tb;

end

% IF YOU WANT TO RUN VTA, AND DON'T NEED TO PRODUCE AN OUTPUT MOVIE -
% RECOMMENDED!

ImageInfo = struct('I_0',I_0,'N_out',N_out,'Tb_out',Tb,'del_XY',del_XY,'E_XY',E_XY,'J_max',J_max);

save([save_path{kkk},'\'','Vid_',filename{kkk}(1:max(find(filename{kkk} == '.')-1),'_ProcessedImage'],'ImageInfo');

% IF YOU NEED TO RUN VTA, AND PRODUCE AN OUTPUT MOVIE -
% THIS IS REALLY FOR DEMONSTRATION PURPOSES ONLY!

%   save([save_path{kkk},'\'','Vid_',filename{kkk}(1:max(find(filename{kkk} == '.')-1),'_ProcessedImage'],'ImageInfo','mov');

% IF YOU ONLY WANT THE IMAGE (FOR ALIGNMENT PURPOSES ONLY)

%   ImageInfo = struct('I_0',I_0);

%   save([save_path{kkk},'\'','Vid_',filename{kkk}(1:max(find(filename{kkk} == '.')-1),'DUPLICATE_ProcessedImage'],'ImageInfo');

```



```

        close(waitbar_trial);
    end

    close(waitbar_vid);

    dir_indexes = find(save_path{1} == '\');
    dir_level = 4;
    save_path = save_path{1}(1:dir_indexes(dir_level)-1);

    %=====
    %=====

    function VTA_step2(button1,answer2,save_path)

    % Create the _SignalInfo output, saved for future analysis.

    if strcmp(button1,'step-by-step');

        prompt={'Spike threshold:',...

            'Enter the minimum # of ICs to look for (K_m_i_n):',...

            'Enter the maximum # of ICs to look for (K_m_a_x):'};

        name='Signal Processing Parameters';

        numlines=1;

        defaultanswer={'1.96','1','3'};

        options.Resize='on';

```

```

options.WindowStyle='normal';
options.Interpreter='tex';
answer=inputdlg(prompt,name,numlines,defaultanswer,options);
uiwait(warndlg('Please select a folder containing data analysis files from VTA Step 1'));
[pathname filename] = build_filelist_signalprocess(save_path);
elseif strcmp(button1,'all-at-once');
    answer = answer2;
    [pathname filename] = build_filelist_signalprocess(save_path);
end

Ts_0 = str2num(answer{1});
K_min = str2num(answer{2});
K_max = str2num(answer{3});

K = K_max - K_min + 1;

waitbar_vid = waitbar(0,['Currently Analyzing ' num2str(0) ' of ' num2str(size(filename,2)) ' Videos'],'Position',[480 390 270 60]);
for kkk = 1:size(filename,2);

    load([pathname{kkk},'\',filename{kkk}]);
    J_max = ImageInfo(1).J_max;
    waitbar(kkk/size(filename,2),waitbar_vid,['Currently Analyzing ' num2str(kkk) ' of ' num2str(size(filename,2)) ' Videos']);
    waitbar_trial = waitbar(0,['Trial Number ' num2str(0) ' of ' num2str(J_max) ' Trials'],'Position',[480 300 270 60]);

```

```

%VTA algorithm begins here. Runs on each video identified by the
%function <build_filelist>.

del_K_raw_out = [];

params = [];

for J = 1:J_max;

    %clear variables from prior use and update waitbar
    clear E_XY del_XY Ts amp_mean threshold inds U S pc eigen IC_try ;

    E_XY = ImageInfo(J).E_XY;
    del_XY = ImageInfo(J).del_XY;

    waitbar(J/J_max,waitbar_trial,['Trial Number ' num2str(J) ' of ' num2str(J_max) ' Trials']);

    waitbar_IC = waitbar(0,['Currently Analyzing ' num2str(0) ' ICs - (Range = ' num2str(K_min) ' - ' num2str(K_max) ')'],'Position',[480 210 270 60]);

    %Zero out del_XY function from W_XYs that do not contain
    %contractile activity.

    [Ts] = step2_parameter_gen(Ts_0);

    [amp_mean threshold] = find_activity(E_XY,Ts);

    inds = find(amp_mean == 0);

    for ii = 1:length(inds);

        del_XY(:,inds(ii)) = zeros(size(del_XY,1),1);

    end
end

```

```

%BEGIN ICA LOOP

[U,S,pc]= svd(del_XY',0);
eigen = diag(S).^2;
IC_try = K_min:K_max;

for K = 1:(K_max - K_min + 1);

    waitbar((K-K_min+1)/(K_max-K_min+1),waitbar_IC,['Currently Analyzing ' num2str(K) ' ICs - (Range = ' num2str(K_min) ' - ' num2str(K_max) ')']);
    clear W del_K_raw;

    %Execute ICA to generate the del_K functions (suggested
    %myotube activity patterns) from the larger number of
    %del_XY functions generated previously, and normalize them.
    W = jade(del_XY',IC_try(K));
    del_K_raw = abs((W * del_XY')');
    for ii = 1:size(del_K_raw,2);
        del_K_raw(:,ii) = (del_K_raw(:,ii)-min(del_K_raw(:,ii)))/max(del_K_raw(:,ii)-min(del_K_raw(:,ii)));
    end
    del_K_raw_out{J,K} = del_K_raw;
    Ts_out(J) = Ts;

end

close(waitbar_IC);

```

```

end

SignalInfo = struct('del_K_raw',del_K_raw_out,'Ts_out',Ts_out);

save([pathname{kkk},'\',filename{kkk}{1:max(find(filename{kkk} == '_')-1),'_ProcessedSignal'],'SignalInfo');

close(waitbar_trial);

end

close(waitbar_vid);

%=====
%=====

function VTA_step3(button1,answer3,save_path)

% Create the _Output output, saved for future analysis.

if strcmp(button1,'step-by-step');

    prompt={'Correlation threshold:',...

        'Length threshold',...

        'Area threshold',...

        'Triangle threshold',...

        'Node threshold'};

    name='Cost-Benefit Parameters';

    numlines=1;

    defaultanswer={'.6','50','.4','15','10'};

    options.Resize='on';

```

```

options.WindowStyle='normal';
options.Interpreter='tex';
answer=inputdlg(prompt,name,numlines,defaultanswer,options);
uiwait(warndlg('Please select a folder containing data analysis files from VTA Step 1 and Step 2'));
else
    answer = answer3;
end

Tr_0 = str2num(answer{1});
Tl_0 = str2num(answer{2});
Ta_0 = str2num(answer{3});
Tt_0 = str2num(answer{4});
Tn_0 = str2num(answer{5});

[pathname filename1 filename2] = build_filelist_CB(save_path);
waitbar_vid = waitbar(0,['Currently Analyzing ' num2str(0) ' of ' num2str(size(filename1,2)) ' Videos'],'Position',[480 390 270 60]);
for kkk = 1:size(filename1,2);

    load([pathname{kkk},'\',filename1{kkk}]);
    load([pathname{kkk},'\',filename2{kkk}]);

    J_max = ImageInfo(1).J_max;
    waitbar(kkk/size(filename1,2),waitbar_vid,['Currently Analyzing ' num2str(kkk) ' of ' num2str(size(filename1,2)) ' Videos']);

```

```
waitbar_trial = waitbar(0,['Trial Number ' num2str(0) ' of ' num2str(J_max) ' Trials'],'Position',[480 300 270 60]);
```

```
%VTA algorithm begins here. Runs on each video identified by the
```

```
%function <build_filelist>.
```

```
clear IC_guess area_info monte_carlo_parameters S_F_metrics;
```

```
clear IC_guess area_info params S_F_metrics;
```

```
X_clusters_out = [];
```

```
Y_clusters_out = [];
```

```
R_clusters_out = [];
```

```
R_raw_out = [];
```

```
del_K_raw_out = [];
```

```
R_out = [];
```

```
del_K_out = [];
```

```
amp_mean_out = [];
```

```
params = [];
```

```
K_min = size(SignalInfo(1,1).del_K_raw,2);
```

```
K_max = size(SignalInfo(1,(size(SignalInfo,2))).del_K_raw,2);
```

```
IC_try = K_min:K_max;
```

```
for J = 1:J_max;
```

```
clear ind_end footprint N Ts Tr Tb I_0 Y_raw X_raw y x del_XY amp_mean X Y amp_mean_lin inds;
```

```

Ts = SignalInfo(J).Ts_out(J);
Tb = ImageInfo(J).Tb_out;
[Tr TI Ta Tt Tn] = step3_parameter_gen(Tr_0,TI_0,Ta_0,Tt_0,Tn_0);
I_0 = ImageInfo(J).I_0;
N = ImageInfo(J).N_out;
E_XY = ImageInfo(J).E_XY;
del_XY = ImageInfo(J).del_XY;

S1 = zeros(1,size(IC_try,2));
S2 = zeros(1,size(IC_try,2));
S3 = zeros(1,size(IC_try,2));
cell_num = zeros(1,size(IC_try,2));
F1 = zeros(1,size(IC_try,2));
F2 = zeros(1,size(IC_try,2));
F3 = zeros(1,size(IC_try,2));

[amp_mean threshold] = find_activity(E_XY,Ts);

if sum(amp_mean > threshold) > Tn;

    y = size(I_0,1)/N;
    x = size(I_0,2)/N;
    Y_raw = floor((1/2*y):y:size(I_0,1));

```



```

X_raw = floor((1/2*x):x:size(I_0,2));
[X_grid,Y_grid] = meshgrid(X_raw,Y_raw);
X = reshape(X_grid,1,(size(X_grid,1)*size(X_grid,2)));
Y = reshape(Y_grid,1,(size(Y_grid,1)*size(Y_grid,2)));
y = floor(y);
x = floor(x);

%clear variables from prior use and update waitbar
waitbar(J/J_max,waitbar_trial,['Trial Number ' num2str(J) ' of ' num2str(J_max) ' Trials']);
waitbar_IC = waitbar(0,['Currently Analyzing ' num2str(0) ' ICs - (Range = ' num2str(K_min) ' - ' num2str(K_max) ')'],'Position',[480 210 270 60]);

for K = 1:(K_max - K_min + 1);

    clear W X_clusters Y_clusters del_K_raw del_K R_raw R R_clusters;

    del_K_raw = SignalInfo(J,K).del_K_raw;

    waitbar((K-K_min+1)/(K_max-K_min+1),waitbar_IC,['Currently Analyzing ' num2str(K) ' ICs - (Range = ' num2str(K_min) ' - ' num2str(K_max) ')']);

    %Calculate the correlation of each del_XY W/ EACH del_K and
    %discard del_K functions that correlate with spatially
    %nonsensical clusters of del_XY functions.

    [R_raw] = raw_R_calc(del_K_raw,del_XY);
    [R del_K] = del_K_test(R_raw,del_K_raw,Tr,Tl,Ta,Tt,X,Y);

```

```

cell_num(K) = size(R,1);
S3(K) = cell_num(K);

if isempty(R);
    X_clusters_out{J,K} = [];
    Y_clusters_out{J,K} = [];
    R_clusters_out{J,K} = [];
    R_out{J,K} = [];
    del_K_out{J,K} = [];

else
    del_K_plot(del_K,R,amp_mean,K);
    [X_clusters Y_clusters R_clusters] = XY_cluster_gen(R,Tr,X,Y);
    mesh_gen(K,l_0,X_clusters,Y_clusters,R_clusters,x,y,IC_try,Tl);

    %Group W_XYs into clusters based on correlation of
    %del_XY function with each del_K function, plot, and
    %calculate S/F metrics.
    [S1(K) F1(K)] = S1_F1_metric_gen(R,Tr);
    [S2(K)] = S2_metric_gen(R);
    [F2(K) footprint{K}] = F2_metric_gen(K,l_0,X_clusters,Y_clusters,R_clusters,x,y,IC_try,Tl);
    [F3(K)] = F3_metric_gen(R,Tr,amp_mean);

```

```

    X_clusters_out{J,K} = X_clusters;
    Y_clusters_out{J,K} = Y_clusters;
    R_clusters_out{J,K} = R_clusters;
    R_out{J,K} = R;
    del_K_out{J,K} = del_K;
end
end
close(waitbar_IC);

[ind_end] = summary_plot(S1,S2,S3,F1,F2,F3,Tb,Ts,Tn,Tr,Tl,Ta,Tt,N,filename1{kkk},IC_try,K_max,K_min,J);
pause(1);

monte_carlo_parameters(J,:) = [N Ts Tr Tn 0 Tl Ta Tt];
S_F_metrics(:,J) = [S1 ; S2 ; S3 ; F1 ; F2 ; F3];
IC_guess(J) = cell_num(ind_end);

try
    area_info{J} = footprint(ind_end);
catch ME;
    area_info{J} = 0;
end

close all;

```

```

else
    X_clusters_out{J,K} = [];
    Y_clusters_out{J,K} = [];
    R_clusters_out{J,K} = [];
    R_out{J,K} = [];
    del_K_out{J,K} = [];
end
end
close(waitbar_trial);

save([pathname{kkk}, '\', filename1{kkk}{1:max(find(filename1{kkk} == '_')-1), '_Output'}, 'monte_carlo_parameters', 'IC_guess', 'area_info', 'S_F_metrics');

end
close(waitbar_vid);

%=====
%=====

function [pathname filename save_path] = build_filelist_imageprocess

uiwait(warndlg('Please select a folder containing subfolders of video data. After, please select a folder where you would like analysis files to be saved.'));

dir_list = [];
sub_dir_list = [];
pathname = [];

```

```

filename = [];
save_path = [];
qq = 0;
mm = 0;
nn = 0;

directory_root = uigetdir([], 'SELECT FOLDER CONTAINING DATA');
save_dir = uigetdir([], 'CHOOSE LOCATION TO SAVE ANALYZED DATA');
curr_time = datestr(now);
curr_time(find(curr_time == ':') = '_');
A = dir(directory_root);
for ii = 3:size(A,1);

    if getfield(A,{ii,1}, 'isdir') == 1;

        qq = qq + 1;
        if ischar(getfield(A,{ii,1}, 'name'));
            dir_list{qq} = getfield(A,{ii,1}, 'name');
        else
            dir_list{qq} = num2str(getfield(A,{ii,1}, 'name'));
        end

        B = dir([directory_root, '\', dir_list{qq}]);
        for jj = 3:size(B,1);

```

```

if getfield(B,{jj},1,'isdir') == 1;
    mm = mm + 1;
    if ischar(getfield(B,{jj},1,'name'));
        sub_dir_list{mm} = getfield(B,{jj},1,'name');
    else
        sub_dir_list{mm} = num2str(getfield(B,{jj},1,'name'));
    end

    mkdir([save_dir '\ ' curr_time ' Data Analysis' '\ ' dir_list{qq} '\ ' sub_dir_list{mm}]);

    C = dir([directory_root '\ ' dir_list{qq} '\ ' sub_dir_list{mm}]);
    vid_names = {C.name};
    for kk = 1:size(vid_names,2);
        if strcmp(vid_names{kk}(max(find(vid_names{kk} == '.'):end),'.avi');
            nn = nn + 1;
            pathname{nn} = [directory_root '\ ' dir_list{qq} '\ ' sub_dir_list{mm}];
            filename{nn} = [vid_names{kk}];
            save_path{nn} = [save_dir '\ ' curr_time ' Data Analysis' '\ ' dir_list{qq} '\ ' sub_dir_list{mm}];
        else
            end
        end
    end
end
end
end

```

```
end
```

```
end
```

```
%=====
```

```
%=====
```

```
function [mov n] = raw_data_gen(filename,pathname,kkk)
```

```
mov = aviread([pathname{kkk} '/' filename{kkk}]);
```

```
[m n] = size(mov);
```

```
%=====
```

```
%=====
```

```
function [N Tb] = step1_parameter_gen(N_0,Tb_0)
```

```
%Number of horizontal and vertical divisions used in segmenting image into
```

```
%interrogation windows (W_XYs)
```

```
N = N_0 + round((rand - .5)*20);
```

```
% N = N_0;
```

```
%Imaging threshold used to convert original image to black & white
```

```
if strcmp(Tb_0,'auto');
```

```
Tb = ['auto'];
```

```
else
```

```
Tb = Tb_0 + ((rand - .5)*.15);
```

```
end
```

```
%=====
```

```
%=====
```

```
function [Ts] = step2_parameter_gen(Ts_0)
```

```
%Spike threshold used for detecting regions of contractile activity
```

```
Ts = Ts_0 + ((rand - .5)*1.9);
```

```
%=====
```

```
%=====
```

```
function [Tr Tl Ta Tt Tn] = step3_parameter_gen(Tr_0,Tl_0,Ta_0,Tt_0,Tn_0)
```

```
%Correlation threshold applied to the correlation coefficient between each
```

```
%W_XY's del_XY function to determine which image regions are correlated
```

```
%with del_K function
```

```
Tr = Tr_0 + ((rand - .5)*.15);
```


%Length threshold - i.e., the maximim allowable length of an edge

%connecting two nodes in the W_XY clusters. Edges above this length are

%removed from the clusters.

Tl = Tl_0;

%Area threshold - the maximum proportions of the image that can be covered

%by a single cell. Clusters covering more than this percentage of the

%screen are excluded.

Ta = Ta_0;

%Triangle threshold - the minimum number of triangles contained by a

%cluster to be included in analysis. Clusters containing fewer than this

%number of triangles are excluded

Tt = Tt_0;

%Node threshold - the mimimum number of W_XYs containing contractile

%activity needed by a del_K to be included in analysis

Tn = Tn_0;

%=====

%=====

```

function [I_0 del_XY E_XY] = del_XY_gen(mov,n,N,Tb)

[I_0,map] = frame2im(mov(1));
y = size(I_0,1)/N;
x = size(I_0,2)/N;
vert_edges = floor(1:y:size(I_0,1));
horz_edges = floor(1:x:size(I_0,2));
Y_raw = floor((1/2*y):y:size(I_0,1));
X_raw = floor((1/2*x):x:size(I_0,2));
y = floor(y);
x = floor(x);

[X_grid,Y_grid] = meshgrid(X_raw,Y_raw);
X = reshape(X_grid,1,(size(X_grid,1)*size(X_grid,2)));
Y = reshape(Y_grid,1,(size(Y_grid,1)*size(Y_grid,2)));

% Automatically choose optimal Tb for each interrogation window if Tb =
% 'auto', otherwise, threshold according to Tb
if strcmp(Tb,'auto');
    for jj = 1:N;
        for kk = 1:N;
            I = I_0(vert_edges(jj):vert_edges(jj) + y-1,horz_edges(kk):horz_edges(kk) + x-1);
            [dummy T] = histeq(I,2);

```

```

        Tb_grid(jj, kk) = find(T, 1, 'first')/256;
    end
end
else
    Tb_grid = Tb*ones(N,N);
end

%Create the error signal for each image section (E_XY_3D), and reshape it
%into E_XY

waitbar_IC = waitbar(0, ['Abandon all hope...'], 'Position', [480 210 270 60]);
E_XY_3D = [];
for ii = 1:n-1;
    I_t = frame2im(mov(ii+1));
    waitbar(ii/(n-1), waitbar_IC, ['Abandon all hope...']);
    for jj = 1:N;
        for kk = 1:N;
            I_orig = I_0(ver_edges(jj):ver_edges(jj) + y-1, horz_edges(kk):horz_edges(kk) + x-1);
            I_orig = im2bw(I_orig, Tb_grid(jj, kk));
            I = I_t(ver_edges(jj):ver_edges(jj) + y-1, horz_edges(kk):horz_edges(kk) + x-1);
            I = im2bw(I, Tb_grid(jj, kk));
            E_XY_3D(ii, jj, kk) = sum(sum(abs(I - I_orig)))/(y*x);
        end
    end
end

```

```

    end
end
close(waitbar_IC);

%Reshape the error signal generated above into a (n-1) by N^2 array (E_XY)
%to correspond with other matrices used in the algorithm.
E_XY = reshape(E_XY_3D,n-1,N^2);

%Generates del_XY by normalizing each E_XY to itself, and eliminates NaNs.
del_XY = [];
for ii = 1:size(E_XY,2)
    del_XY(:,ii) = (E_XY(:,ii)-min(E_XY(:,ii)))/max(E_XY(:,ii)-min(E_XY(:,ii)));
end
del_XY(isnan(del_XY)) = 0;

%=====
%=====

function [pathname filename] = build_filelist_signalprocess(save_path)

if isempty(save_path);
    directory_root = uigetdir;
else

```

```

    directory_root = save_path;
end

dir_list = [];
sub_dir_list = [];
pathname = [];
filename = [];
qq = 0;
mm = 0;
nn = 0;

A = dir(directory_root);
for ii = 3:size(A,1);

    if getfield(A,{ii,1},'isdir') == 1;
        qq = qq + 1;
        if ischar(getfield(A,{ii,1},'name'));
            dir_list{qq} = getfield(A,{ii,1},'name');
        else
            dir_list{qq} = num2str(getfield(A,{ii,1},'name'));
        end
    end

    B = dir([directory_root,'\',dir_list{qq}]);

```

```

for jj = 3:size(B,1);
    if getfield(B,{jj},1,'isdir') == 1;
        mm = mm + 1;
        if ischar(getfield(B,{jj},1,'name'));
            sub_dir_list{mm} = getfield(B,{jj},1,'name');
        else
            sub_dir_list{mm} = num2str(getfield(B,{jj},1,'name'));
        end

        C = dir([directory_root,'\',dir_list{qq},'\',sub_dir_list{mm}]);
        vid_names = {C.name};
        for kk = 1:size(vid_names,2);
            if strcmp(vid_names{kk}(max(find(vid_names{kk} == '_'):end),'_ProcessedImage.mat');
                nn = nn + 1;

                pathname{nn} = [directory_root '\',dir_list{qq}, '\', sub_dir_list{mm}];
                filename{nn} = [vid_names{kk}];

            else
                end
            end
        end
    end
end
end
end
end

```

```

%=====
%=====

function [amp_mean threshold] = find_activity(E_XY,Ts)

%Spike detection by comparison with the quantity Ts multiplied by the STD
threshold = mean(mean(E_XY)) + Ts * mean(std(E_XY,0,1));
for ii = 1:size(E_XY,2);
    [peak_value{ii}] = spikes_detect(E_XY(:,ii),threshold);

    if isempty(peak_value{ii});
        amp_mean(ii) = 0;
    else
        amp_mean(ii) = mean(peak_value{ii});
    end
end

%=====
%=====

function [peak_values] = spikes_detect(E_XY,threshold)

```

```
record_toggle = 0;

kk = 0;

peak_values = [];

for ii = 2:length(E_XY);
    if E_XY(ii) > threshold && E_XY(ii-1) <= threshold;
        record_toggle = 1;

        kk = kk + 1;

        jj = 1;

        spike_trace = [];
    elseif record_toggle == 1 && E_XY(ii) <= threshold && E_XY(ii-1) > threshold;
        record_toggle = 0;

        [peak_values(kk)] = max(spike_trace);
    end

    if record_toggle == 1;
        spike_trace(jj) = E_XY(ii);

        jj = jj + 1;
    else
        end
    end

end

peak_values = peak_values';
```



```
%=====
```

```
%=====
```

```
function [R_raw] = raw_R_calc(del_K,del_XY)
```

```
for ii = 1:size(del_K,2);
```

```
    for jj = 1:size(del_XY,2);
```

```
        corrs = corrcoef(del_K(:,ii),del_XY(:,jj));
```

```
        R_raw(ii,jj) = corrs(1,2);
```

```
        if isnan(R_raw(ii,jj));
```

```
            R_raw(ii,jj) = 0;
```

```
        else
```

```
        end
```

```
    end
```

```
end
```

```
%=====
```

```
%=====
```

```
function [R del_K] = del_K_test(R_raw,del_K_raw,Tr,Tl,Ta,Tt,X,Y)
```

```
%Initialize outputs and counters
```

```

num_points = [];
footprint_test = [];
zz = 1;
R = [];
del_K = [];
footprint_thresh = Ta*512*640;

%Test clusters for geometric feasibility
for ii = 1:size(R_raw,1);
    X_clusters{ii} = X(find(R_raw(ii,:) >= Tr));
    Y_clusters{ii} = Y(find(R_raw(ii,:) >= Tr));
    if isempty(X_clusters{ii}) || length(X_clusters{ii}) < 3;
        num_tri(ii) = 0;
        footprint_test(ii) = 0;
    else
        tri = delaunay(X_clusters{ii},Y_clusters{ii},{'QJ'});
        [tri_mod dummy] = tri_prune(tri,X_clusters{ii},Y_clusters{ii},Tl);
        num_tri(ii) = size(tri_mod,1);
        if isempty(tri_mod);
            footprint_test(ii) = 0;
        else
            footprint_test(ii) = tri_area(tri_mod,X_clusters{ii},Y_clusters{ii});
        end
    end
end

```

```

end

if ((num_tri(ii) >= Tt) & (footprint_test(ii) < footprint_thresh));

    R(zz,:) = R_raw(ii,:);

    del_K(:,zz) = del_K_raw(:,zz);

    zz = zz + 1;

else

end

end

end

%=====
%=====

function [tri_mod av_lengths] = tri_prune(tri,x,y,Tl)

qq = 1;

max_length = [];

for ii = 1:size(tri,1);

    tri_int = tri(ii,:);

    for jj = 1:3;

        x0 = x(tri_int(1));

        y0 = y(tri_int(1));

        x1 = x(tri_int(2));

        y1 = y(tri_int(2));

```

```

leg_length(jj) = sqrt( (x1-x0)^2 + (y1-y0)^2 );
tri_int_old = tri_int;
tri_int(1) = tri_int_old(2);
tri_int(2) = tri_int_old(3);
tri_int(3) = tri_int_old(1);
qq = qq + 1;
end
max_length(ii) = max(leg_length);
end

```

```

tri_mod = tri(find(max_length < Tl),:);

```

```

legss = [];
if isempty(tri_mod);
    legss = 0;
else
    kk = 1;
    for ii = 1:size(tri_mod,1);
        tri_int = tri_mod(ii,:);
        for jj = 1:3;
            x0 = x(tri_int(1));
            y0 = y(tri_int(1));
            x1 = x(tri_int(2));

```

```

    y1 = y(tri_int(2));
    leg_length(jj) = sqrt( (x1-x0)^2 + (y1-y0)^2 );
    legss(kk) = leg_length(jj);
    tri_int_old = tri_int;
    tri_int(1) = tri_int_old(2);
    tri_int(2) = tri_int_old(3);
    tri_int(3) = tri_int_old(1);
    kk = kk + 1;
end
end
end

av_lengths = mean(legss);

%=====
%=====

function [A] = tri_area(tri,X,Y)

for ii = 1:size(tri,1);
    P = [X(tri(ii,1)) Y(tri(ii,1)) ; X(tri(ii,2)) Y(tri(ii,2)) ; X(tri(ii,3)) Y(tri(ii,3))];
    [q,r] = qr((P(2:3,:) - repmat(P(1,:),2,1))');
    A(ii) = abs(prod(diag(r)))/2;
end

```

end

A = sum(A);

%=====

%=====

function del_K_plot(del_K,R,amp_mean_lin,K)

N = sqrt(size(R,2));

IC_window_size = [1200 750];

IC_window_start = [1 150];

figure(10+K); clf; hold on;

set(figure(10+K),'Position',[IC_window_start(1)+20*K IC_window_start(2)-20*K IC_window_size]);

subplot(3,1,1); hold on;

xlabel('Time (s)','FontSize',12);

ylabel('\delta_K Value','FontSize',12);

title('\delta_K(t) Functions vs. Time','FontWeight','Bold','FontSize',14);

cluster_color_ind = hsv(size(R,1));

legend_strings = [];

for ii = 1:size(R,1);

plot((.15 * [1:size(del_K,1)]),del_K(:,ii),'Color',cluster_color_ind(ii,:),'LineWidth',1.5);

```

    legend_strings_new = (['\delta_' num2str(ii) '(t)']);
    legend_strings = strvcat(legend_strings,legend_strings_new);
end
legend(legend_strings,'Location','EastOutside'); legend boxoff;
set(gca,'FontSize',12)

for ii = 1:size(R,1);
    subplot(3,size(R,1),size(R,1) + ii); hold on; title(['\delta_' num2str(ii)],'FontSize',12,'FontWeight','Bold');
    I = reshape(R(ii,:),N,N);
    imagesc(I,[0 1]); axis equal; axis tight; axis off;
end
subplot(3,2,5); hold on; axis off; title('Amplitude');
imagesc(reshape(amp_mean_lin-1,N,N)); axis equal; axis off; colorbar; axis tight;
subplot(3,2,6); hold on; axis off; title('Cell Coverage');
imagesc(reshape(max(R,[],1),N,N),[0 1]); axis equal; axis off; colorbar; axis tight;

%=====
%=====

function [X_clusters Y_clusters R_clusters] = XY_cluster_gen(R,Tr,X,Y)

for ii = 1:size(R,1);
    X_clusters{ii} = X(find(R(ii,:) >= Tr));

```

```

Y_clusters{ii} = Y(find(R(ii,:) >= Tr));

if isempty(R(ii,find(R(ii,:) >= Tr)));
    R_clusters{ii} = 0;
else
    R_clusters{ii} = R(ii,find(R(ii,:) >= Tr)); %
end
end

%=====
%=====

function [footprint] = mesh_gen(K,I_0,X_clusters,Y_clusters,R_clusters,x,y,IC_try,tl)

overlay_window_size = [800 600];
overlay_window_start = [700 300];
figure(K); clf; hold on;
set(figure(K),'Position',[overlay_window_start(1)+20*K overlay_window_start(2)-20*K overlay_window_size]);

imagesc(I_0); colormap('gray'); axis('equal'); axis('tight');
cluster_color_ind = hsv(size(X_clusters,2));
for ii = 1:size(X_clusters,2);
    if isempty(X_clusters{ii}) || length(X_clusters{ii}) < 3;

```



```

else

    tri = delaunay(X_clusters{ii},Y_clusters{ii},{'QJ'});

    [tri_mod av_lengths(ii)] = tri_prune(tri,X_clusters{ii},Y_clusters{ii},Tl);

    footprint(ii) = 0;

    footprint(ii) = tri_area(tri_mod,X_clusters{ii},Y_clusters{ii});

    if isempty(tri_mod);

    else

        for jj = 1:1:size(tri_mod,1);

            patch(X_clusters{ii}(tri_mod(jj,:)),Y_clusters{ii}(tri_mod(jj,:)),cluster_color_ind(ii,:), 'FaceAlpha',.2,'EdgeColor',cluster_color_ind(ii,:), 'LineWidth',.75);

        end

        scatter(X_clusters{ii},Y_clusters{ii},R_clusters{ii}*(y*x)*.5,cluster_color_ind(ii,:), 'LineWidth',.75);

        triplot(tri_mod,X_clusters{ii},Y_clusters{ii}, 'Color',cluster_color_ind(ii,:), 'LineWidth',.75);

    end

end

end

axis off;

axis tight;

title(['W_X_Y Clusters Based on Correlation of \delta_X_Y and \delta_K - ' num2str(size(X_clusters,2)) ' Clusters (Search For ' num2str(IC_try(K)) ' ICs)']);

%=====
%=====

function [pathname filename1 filename2] = build_filelist_CB(save_path)

```

```
if isempty(save_path);
    directory_root = uigetdir;
else
    directory_root = save_path;
end

dir_list = [];
sub_dir_list = [];
pathname = [];
filename = [];
save_path = [];

qq = 0;
mm = 0;
nn = 0;
nnn = 0;

A = dir(directory_root);
for ii = 3:size(A,1);

    if getfield(A,{ii,1},'isdir') == 1;
        qq = qq + 1;
        if ischar(getfield(A,{ii,1},'name'));

```

```

    dir_list{qq} = getfield(A,{ii,1},'name');
else
    dir_list{qq} = num2str(getfield(A,{ii,1},'name'));
end

B = dir([directory_root,'\dir_list{qq}']);
for jj = 3:size(B,1);
    if getfield(B,{jj,1},'isdir') == 1;
        mm = mm + 1;
        if ischar(getfield(B,{jj,1},'name'));
            sub_dir_list{mm} = getfield(B,{jj,1},'name');
        else
            sub_dir_list{mm} = num2str(getfield(B,{jj,1},'name'));
        end
    end

    C = dir([directory_root,'\dir_list{qq}','\sub_dir_list{mm}']);
    vid_names = {C.name};
    for kk = 1:size(vid_names,2);
        if strcmp(vid_names{kk})(max(find(vid_names{kk} == '_')):end),'_ProcessedSignal.mat');
            nn = nn + 1;
            pathname{nn} = [directory_root '\ dir_list{qq} '\ sub_dir_list{mm}];
            filename1{nn} = [vid_names{kk}];
        else

```

```

end

if strcmp(vid_names{kk}(max(find(vid_names{kk} == '_'):end), '_ProcessedImage.mat');
    nnn = nnn + 1;
    pathname{nnn} = [directory_root '\' dir_list{qq} '\' sub_dir_list{mm}];
    filename2{nnn} = [vid_names{kk}];
else
end
end
end
end
end
end

%=====
%=====

function [S1 F1] = S1_F1_metric_gen(R,Tr)

for ii = 1:size(R,1);
    if isempty(R(ii,find(R(ii,:) >= Tr)));
        R_clusters{ii} = 0;
    else

```

```

    R_clusters{ii} = R(ii,find(R(ii,:) >= Tr)); %
end

R_clusters_inverse_temp = R(ii,find(R(ii,:) < Tr));
R_clusters_inverse{ii} = R_clusters_inverse_temp(find(R_clusters_inverse_temp));

R_good(ii) = mean(R_clusters{ii});
R_bad(ii) = mean(R_clusters_inverse{ii});

area_success_function(ii) = length(R_clusters{ii})(find(isnan(R_clusters{ii}) == 0))/size(R,2); %
end

S1 = sum(area_success_function);
F1 = 1 - (mean(R_good) - mean(R_bad));

%=====
%=====

function [S2] = S2_metric_gen(R)

R_sort = sort(R,1,'descend');
if isempty(R_sort(2:end,:));
    mean_wrong_del_K = zeros(1,size(R_sort,2));
else

```

```

    mean_wrong_del_K = mean(R_sort(2:end,:),1);
end

success_spread = R_sort(1,:) - mean_wrong_del_K;
S2 = mean(success_spread(find(isnan(success_spread) == 0)));

%=====

%=====

function [F2 footprint] = F2_metric_gen(K,l_0,X_clusters,Y_clusters,R_clusters,x,y,IC_try,Tl)

for ii = 1:size(X_clusters,2);
    if isempty(X_clusters{ii}) || length(X_clusters{ii}) < 3;
    else
        tri = delaunay(X_clusters{ii},Y_clusters{ii},{'QJ'});
        [tri_mod av_lengths(ii)] = tri_prune(tri,X_clusters{ii},Y_clusters{ii},Tl);
        footprint(ii) = 0;
        footprint(ii) = tri_area(tri_mod,X_clusters{ii},Y_clusters{ii});
    end
end

F2 = mean(av_lengths);

%=====

```

```
%=====
```

```
function [F3] = F3_metric_gen(R,Tr,amp_mean_lin)
```

```
total_fit_R = max(R,[],1);
```

```
missed_twitch = amp_mean_lin(find(total_fit_R < Tr));
```

```
F3 = sum(missed_twitch);
```

```
%=====
```

```
%=====
```

```
function [ind_end] = summary_plot(S1,S2,S3,F1,F2,F3,Tb,Ts,Tn,Tr,Tl,Ta,Tt,N,filename,IC_try,K_max,K_min,J)
```

```
%COMBINATION OF SUCCESS METRICS
```

```
S1_norm = S1/max(S1);
```

```
S2_norm = S2/max(S2);
```

```
S3_norm = S3/K_max;
```

```
total_success = sqrt( (S2_norm).^2 + (S1_norm).^2 + (S3_norm).^2 );
```

```
[value ind] = max(total_success);
```

```
%COMBINATION OF COST METRICS
```

```
F1_norm = F1/max(F1);
```

```
F2_norm = F2/max(F2);
```

```
F3_norm = F3/max(F3);
```

```
total_failure = sqrt( (F2_norm).^2 + (F1_norm).^2 +(F3_norm).^2 );
```

```
[value min_failure_ind] = min(total_failure(find(total_failure)));
```

```
failure_ind_list = find(total_failure);
```

```
ind_f = failure_ind_list(min_failure_ind);
```

```
%CALCULATING THE NET SUCCESS LEVEL
```

```
net_success = total_success - total_failure;
```

```
if isempty(find(net_success))
```

```
    val_end = 0;
```

```
    ind_end = 1;
```

```
else
```

```
    [val_end temp_ind] = max(net_success(find(net_success)));
```

```
    ind_list = find(net_success);
```

```
    ind_end = ind_list(temp_ind);
```

```
end
```

```
IC_final_choice = zeros(1,length(net_success));
```

```
IC_final_choice(ind_end) = val_end;
```

```
figure(99+J); clf; hold on;
```

```
set(figure(99+J),'Position',[1 60 1600 900]);
```



```

subplot(2,2,2); hold on;
for ii = 1:(K_max - K_min + 1);
    if ii == ind_f;
    else
        plot3(F1_norm(ii),F2_norm(ii),0,'bo','MarkerSize',10,'LineWidth',1);
        text(F1_norm(ii),F2_norm(ii),0,num2str(IC_try(ii)),'HorizontalAlignment','Center','FontWeight','Light','FontSize',10,'Color','b');

        plot3(F1_norm(ii),1,F3_norm(ii),'bo','MarkerSize',10,'LineWidth',1);
        text(F1_norm(ii),1,F3_norm(ii),num2str(IC_try(ii)),'HorizontalAlignment','Center','FontWeight','Light','FontSize',10,'Color','b');

        plot3(1,F2_norm(ii),F3_norm(ii),'bo','MarkerSize',10,'LineWidth',1);
        text(1,F2_norm(ii),F3_norm(ii),num2str(IC_try(ii)),'HorizontalAlignment','Center','FontWeight','Light','FontSize',10,'Color','b');

        plot3([0 F1_norm(ii)], [0 F2_norm(ii)], [0 F3_norm(ii)], 'k-', 'MarkerSize', 15, 'LineWidth', 1);
        scatter3(F1_norm(ii),F2_norm(ii),F3_norm(ii),total_failure(ii)*100,[.7 .7 .7],'filled');
        text(F1_norm(ii),F2_norm(ii),F3_norm(ii),num2str(IC_try(ii)),'HorizontalAlignment','Right','VerticalAlignment','Bottom','FontWeight','Bold','FontSize',12,'Margin',15);
    end
end
plot3(F1_norm(ind_f),F2_norm(ind_f),0,'ro','MarkerSize',10,'LineWidth',2);
text(F1_norm(ind_f),F2_norm(ind_f),0,num2str(IC_try(ind_f)),'HorizontalAlignment','Center','FontWeight','Bold','FontSize',10,'Color','r');

plot3(F1_norm(ind_f),1,F3_norm(ind_f),'ro','MarkerSize',10,'LineWidth',2);

```

```

text(F1_norm(ind_f),1,F3_norm(ind_f),num2str(IC_try(ind_f)),'HorizontalAlignment','Center','FontWeight','Bold','FontSize',10,'Color','r');

plot3(1,F2_norm(ind_f),F3_norm(ind_f),'ro','MarkerSize',10,'LineWidth',2);
text(1,F2_norm(ind_f),F3_norm(ind_f),num2str(IC_try(ind_f)),'HorizontalAlignment','Center','FontWeight','Bold','FontSize',10,'Color','r');

plot3([0 F1_norm(ind_f)],[0 F2_norm(ind_f)],[0 F3_norm(ind_f)],'r-','MarkerSize',15,'LineWidth',2);
scatter3(F1_norm(ind_f),F2_norm(ind_f),F3_norm(ind_f),total_failure(ind_f)*100,'r','filled');
text(F1_norm(ind_f),F2_norm(ind_f),F3_norm(ind_f),num2str(IC_try(ind_f)),'HorizontalAlignment','Right','VerticalAlignment','Bottom','FontWeight','Bold','FontSize',12,'Margin',15);
view(3); grid on; axis([0 1 0 1 0 1]);
xlabel('Correlation Difference (F_1)','FontSize',12); ylabel('Scatter (F_2)','FontSize',12); zlabel('Missed-Twitch (F_3)','FontSize',12); title('Failure
Vector','FontWeight','Bold','FontSize',14);
set(gca,'FontSize',12);

subplot(2,2,1); hold on;
for ii = 1:(K_max - K_min + 1);
    if ii == ind;
    else
        plot3(S2_norm(ii),S1_norm(ii),0,'bo','MarkerSize',10,'LineWidth',1);
        text(S2_norm(ii),S1_norm(ii),0,num2str(IC_try(ii)),'HorizontalAlignment','Center','FontWeight','Light','FontSize',10,'Color','b');

        plot3(S2_norm(ii),1,S3_norm(ii),'bo','MarkerSize',10,'LineWidth',1);
        text(S2_norm(ii),1,S3_norm(ii),num2str(IC_try(ii)),'HorizontalAlignment','Center','FontWeight','Light','FontSize',10,'Color','b');

```

```

plot3(1,S1_norm(ii),S3_norm(ii),'bo','MarkerSize',10,'LineWidth',1);
text(1,S1_norm(ii),S3_norm(ii),num2str(IC_try(ii)),'HorizontalAlignment','Center','FontWeight','Light','FontSize',10,'Color','b');

plot3([0 S2_norm(ii)],[0 S1_norm(ii)],[0 S3_norm(ii)],'k-','MarkerSize',15,'LineWidth',1);
scatter3(S2_norm(ii),S1_norm(ii),S3_norm(ii),total_success(ii)*100,[.7 .7 .7],'filled');
text(S2_norm(ii),S1_norm(ii),S3_norm(ii),num2str(IC_try(ii)),'HorizontalAlignment','Right','VerticalAlignment','Bottom','FontWeight','Bold','FontSize',12,'Margin',15);
end
end
plot3(S2_norm(ind),S1_norm(ind),0,'ro','MarkerSize',10,'LineWidth',2);
text(S2_norm(ind),S1_norm(ind),0,num2str(IC_try(ind)),'HorizontalAlignment','Center','FontWeight','Bold','FontSize',10,'Color','r');

plot3(S2_norm(ind),1,S3_norm(ind),'ro','MarkerSize',10,'LineWidth',2);
text(S2_norm(ind),1,S3_norm(ind),num2str(IC_try(ind)),'HorizontalAlignment','Center','FontWeight','Bold','FontSize',10,'Color','r');

plot3(1,S1_norm(ind),S3_norm(ind),'ro','MarkerSize',10,'LineWidth',2);
text(1,S1_norm(ind),S3_norm(ind),num2str(IC_try(ind)),'HorizontalAlignment','Center','FontWeight','Bold','FontSize',10,'Color','r');

plot3([0 S2_norm(ind)],[0 S1_norm(ind)],[0 S3_norm(ind)],'r-','MarkerSize',15,'LineWidth',2);
scatter3(S2_norm(ind),S1_norm(ind),S3_norm(ind),total_success(ind)*100,'r','filled');
text(S2_norm(ind),S1_norm(ind),S3_norm(ind),num2str(IC_try(ind)),'HorizontalAlignment','Right','VerticalAlignment','Bottom','FontWeight','Bold','FontSize',12,'Margin',15);
view(3); grid on; axis([0 1 0 1 0 1]);
xlabel('Success Spread (S_1)','FontSize',12); ylabel('Area Coverage (S_2)','FontSize',12); zlabel('Cell Number (S_3)','FontSize',12); title('Success Vector','FontWeight','Bold','FontSize',14);

```

```

set(gca,'FontSize',12);

subplot(2,1,2); hold on;
bar([net_success(1:(K_max - K_min + 1))' total_failure(1:(K_max - K_min + 1))'],'stacked'); colormap([.7 .7 .7 ; .6 0 0]);
bar(IC_final_choice(1:(K_max - K_min + 1)),'FaceColor',[0 0 .6]);
set(gca,'XTick',1:(K_max - K_min + 1),'FontSize',12);
tick_labels = [];
for ii = 1:(K_max - K_min + 1);
    tick_labels_new = [num2str(IC_try(ii)) '(' num2str(S3(ii)) ')'];
    tick_labels = strvcat(tick_labels,tick_labels_new);
end
set(gca,'XTickLabel',tick_labels);
monte_carlo_info = strvcat(['Tb = ' num2str(Tb)],['N = ' num2str(N)],['Ts = ' num2str(Ts)],['Tn = ' num2str(Tn)],['Tr = ' num2str(Tr)],['TI = ' num2str(TI)],['Ta = ' num2str(Ta)],['Tt = '
num2str(Tt)]);
text(K_max - K_min + 1.5,max(net_success + total_failure),monte_carlo_info,'FontWeight','Bold','FontSize',12,'HorizontalAlignment','Left','VerticalAlignment','Top');
title('Net Success Score','FontWeight','Bold','FontSize',14); ylabel('Net Success Value','FontSize',12); xlabel('K (# of Clusters Identified)','FontSize',12);
legend('Net Success','Failure','Winner','Location','SouthEastOutside'); legend boxoff;

```

7 Bibliography

1. Langhammer, C.G., J.D. Zahn, and B.L. Firestein, *Identification and Quantification of Skeletal Myotube Contraction and Association In Vitro by Video Microscopy*. Cytoskeleton, 2010.
2. Langhammer, C.G., et al., *Multi-scale Sholl analysis of digitized neurons*. Cytometry: Part A, 2010.
3. Navarro, X., et al., *A critical review of interfaces with the peripheral nervous system for the control of neuroprostheses and hybrid bionic systems*. Journal of the Peripheral Nervous System, 2005. **10**(3): p. 229-258.
4. Leuthardt, E.C., et al., *The emerging world of motor neuroprosthetics: A neurosurgical perspective*. Neurosurgery, 2006. **59**(1): p. 1-13.
5. Micera, S., et al., *Hybrid bionic systems for the replacement of hand function*. Proceedings of the IEEE, 2006. **94**(9): p. 1752-1762.
6. Schwartz, A.B., et al., *Brain-controlled interfaces: Movement restoration with neural prosthetics*. Neuron, 2006. **52**(1): p. 205-220.
7. Prochazka, A. and V.K. Mushahwar, *Spinal cord function and rehabilitation - an overview*. Journal of Physiology-London, 2001. **533**(1): p. 3-4.
8. Prochazka, A., V.K. Mushahwar, and D.B. McCreery, *Neural prostheses*. Journal of Physiology-London, 2001. **533**(1): p. 99-109.
9. Schwartz, A.B., *Cortical neural prosthetics*. Annual Review of Neuroscience, 2004. **27**: p. 487-507.
10. Hochberg, L.R., et al., *Neuronal ensemble control of prosthetic devices by a human with tetraplegia*. Nature, 2006. **442**(7099): p. 164-171.
11. Rutten, W., et al., *Neuroelectronic interfacing with cultured multielectrode arrays toward a cultured probe*. Proceedings of the IEEE, 2001. **89**(7): p. 1013-1029.
12. Rutten, W.L.C., *Selective electrical interfaces with the nervous system*. Annual Review of Biomedical Engineering, 2002. **4**: p. 407-452.
13. Pfister, B.J., et al., *Neural engineering to produce in vitro nerve constructs and neurointerface*. Neurosurgery, 2007. **60**(1): p. 137-141.
14. NINDS. *Neural Interfaces Program: National Institute of Neurological Disorders and Stroke (NINDS)*.: Wednesday, January 13, 2010 4:55:09 PM [cited; Available from: <http://www.ninds.nih.gov/research/npp/index.htm>].
15. Grill, W.M., *Neural Interfaces*. American scientist, 2010. **98**(1): p. 48.
16. NINDS. *NIH Fact Sheet: Cochlear Implants*. [cited 01-13-2010]; Available from: <http://www.nih.gov/about/researchresultsforthepublic/CochlearImplants.pdf>.
17. NIDCD. *NIDCD - Cochlear Implants*.: [cited 2010 Wednesday, January 13, 2010 5:12:36 PM]; Available from: <http://www.nidcd.nih.gov/health/hearing/coch.asp>.
18. Craelius, W., *The bionic man: Restoring mobility*. Science, 2002. **295**(5557): p. 1018-+.
19. Wang, S. and A. Regalado, *Harnessing Thought to Help the Injured*, in *The Wall Street Journal*. 2006.
20. Fischman, J., *bi-on-ics; Etymology: from bi (as in "life") + onics (as in "electronics"); the study of mechanical systems that function like living organisms or parts of living organisms*, in *National Geographic Magazine*. 2010.
21. Pelley, S., *The Pentagon's Bionic Arm: Pentagon Is Working To Develop A Life-Changing, High Tech Prosthetic Arm*, in *60 Minutes*.: 2009.

22. DARPA, *REVOLUTIONIZING PROSTHETICS PROGRAM*. Fact Sheet - Defense Advanced Research Projects Agency: , 2008.
23. Lebedev, M.A. and M.A.L. Nicolelis, *Brain-machine interfaces: past, present and future*. Trends in Neurosciences, 2006. **29**(9): p. 536-546.
24. Fagg, A.H., et al., *Biomimetic brain machine interfaces for the control of movement*. Journal of Neuroscience, 2007. **27**(44): p. 11842-11846.
25. Mussa-Ivaldi, F.A. and L.E. Miller, *Brain-machine interfaces: computational demands and clinical needs meet basic neuroscience*. Trends in Neurosciences, 2003. **26**(6): p. 329-334.
26. Dhillon, G.S., et al., *Residual function in peripheral nerve stumps of amputees: Implications for neural control of artificial limbs*. Journal of Hand Surgery-American Volume, 2004. **29A**(4): p. 605-615.
27. Scharf, A.B., *Useful signals from motor cortex*. The Journal of Physiology, 2007(579): p. 581-601.
28. Brower, V., *When mind meets machine*. Embo Reports, 2005. **6**(2): p. 108-110.
29. Di Pino, G., E. Guglielmelli, and P.M. Rossini, *Neuroplasticity in amputees: Main implications on bidirectional interfacing of cybernetic hand prostheses*. Progress in Neurobiology, 2009. **88**(2): p. 114-126.
30. Micera, S., et al., *On the Use of Longitudinal Intrafascicular Peripheral Interfaces for the Control of Cybernetic Hand Prostheses in Amputees*. Ieee Transactions on Neural Systems and Rehabilitation Engineering, 2008. **16**(5): p. 453-472.
31. Hatsopoulos, N.G. and J.P. Donoghue, *The Science of Neural Interface Systems*. Annual Review of Neuroscience, 2009. **32**: p. 249-266.
32. Schwartz, A.B., *Useful signals from motor cortex*. Journal of Physiology-London, 2007. **579**(3): p. 581-601.
33. Polikov, V.S., P.A. Tresco, and W.M. Reichert, *Response of brain tissue to chronically implanted neural electrodes*. Journal of Neuroscience Methods, 2005. **148**(1): p. 1-18.
34. Szarowski, D.H., et al., *Brain responses to micro-machined silicon devices*. Brain Research, 2003. **983**(1-2): p. 23-35.
35. Ludwig, K.A., et al., *Chronic neural recordings using silicon microelectrode arrays electrochemically deposited with a poly(3,4-ethylenedioxythiophene) (PEDOT) film*. Journal of Neural Engineering, 2006. **3**(1): p. 59-70.
36. Seymour, J.P. and D.R. Kipke, *Neural probe design for reduced tissue encapsulation in CNS*. Biomaterials, 2007. **28**(25): p. 3594-3607.
37. Wells, M.R., et al., *A neuromuscular platform to extract electrophysiological signals from lesioned nerves: A technical note*. Journal of Rehabilitation Research and Development, 2001. **38**(4): p. 385-390.
38. Sergi, P.N., et al., *Biomechanical characterization of needle piercing into peripheral nervous tissue*. Ieee Transactions on Biomedical Engineering, 2006. **53**(11): p. 2373-2386.
39. Lertmanorat, Z., F.W. Montague, and D.M. Durand, *A Flat Interface Nerve Electrode With Integrated Multiplexer*. Ieee Transactions on Neural Systems and Rehabilitation Engineering, 2009. **17**(2): p. 176-182.
40. Wodlinger, B. and D.M. Durand, *Localization and Recovery of Peripheral Neural Sources With Beamforming Algorithms*. Ieee Transactions on Neural Systems and Rehabilitation Engineering, 2009. **17**(5): p. 461-468.
41. Branner, A., R.B. Stein, and R.A. Normann, *Selective stimulation of cat sciatic nerve using an array of varying-length microelectrodes*. Journal of Neurophysiology, 2001. **85**(4): p. 1585-1594.

42. Lago, N., et al., *Neurobiological assessment of regenerative electrodes for bidirectional interfacing injured peripheral nerves*. Ieee Transactions on Biomedical Engineering, 2007. **54**(6): p. 1129-1137.
43. Lacour, S.P., et al., *Long Micro-Channel Electrode Arrays: A Novel Type of Regenerative Peripheral Nerve Interface*. Ieee Transactions on Neural Systems and Rehabilitation Engineering, 2009. **17**(5): p. 454-460.
44. FitzGerald, J.J., et al., *Microchannels as axonal amplifiers*. Ieee Transactions on Biomedical Engineering, 2008. **55**(3): p. 1136-1146.
45. FitzGerald, J.J., et al., *Microchannel Electrodes for Recording and Stimulation: In Vitro Evaluation*. Ieee Transactions on Biomedical Engineering, 2009. **56**(5): p. 1524-1534.
46. Wieringa, P.A.W., R.W.F.; le Feber, J.; Rutten, W.L.C., *Neural growth into a microchannel network: Towards A regenerative neural interface*, in *Neural Engineering, 2009. NER '09. 4th International IEEE/EMBS Conference on*. 2009. p. 51-55.
47. Lacour, S.P., et al., *Polyimide micro-channel arrays for peripheral nerve regenerative implants*. Sensors and Actuators a-Physical, 2008. **147**(2): p. 456-463.
48. Suzuki, T., et al., *Regeneration-Type Nerve Electrode Using Bundled Microfluidic Channels*. Electronics and Communications in Japan, 2009. **92**(4): p. 29-34.
49. Parker, P., K. Englehart, and B. Hudgins, *Myoelectric signal processing for control of powered limb prostheses*. Journal of Electromyography and Kinesiology, 2006. **16**(6): p. 541-548.
50. Oskoei, M.A. and H.S. Hu, *Myoelectric control systems-A survey*. Biomedical Signal Processing and Control, 2007. **2**(4): p. 275-294.
51. Light, C.M., et al., *Intelligent multifunction myoelectric control of hand prostheses*. Journal of Medical Engineering & Technology, 2002. **26**(4): p. 139-146.
52. Kuiken, T.A., *Consideration of nerve-muscle grafts to improve the control of artificial arms*. Journal of Technology and Disability, 2003. **15**(2): p. 105-111.
53. Kuiken, T.A., et al., *Targeted Muscle Reinnervation for Real-time Myoelectric Control of Multifunction Artificial Arms*. Jama-Journal of the American Medical Association, 2009. **301**(6): p. 619-628.
54. Das, M., et al., *A defined system to allow skeletal muscle differentiation and subsequent integration with silicon microstructures*. Biomaterials, 2006. **27**(24): p. 4374-4380.
55. Das, M., et al., *Electrophysiological and morphological characterization of rat embryonic motoneurons in a defined system*. Biotechnology Progress, 2003. **19**(6): p. 1756-1761.
56. Das, M., et al., *Embryonic motoneuron-skeletal muscle co-culture in a defined system*. Neuroscience, 2007. **146**(2): p. 481-488.
57. Maher, M.P., et al., *The neurochip: a new multielectrode device for stimulating and recording from cultured neurons*. Journal of Neuroscience Methods, 1999. **87**(1): p. 45-56.
58. Zeck, G. and P. Fromherz, *Noninvasive neuroelectronic interfacing with synaptically connected snail neurons immobilized on a semiconductor chip*. Proceedings of the National Academy of Sciences of the United States of America, 2001. **98**(18): p. 10457-10462.
59. James, C.D., et al., *Extracellular recordings from patterned neuronal networks using planar microelectrode arrays*. Ieee Transactions on Biomedical Engineering, 2004. **51**(9): p. 1640-1648.

60. Fromherz, P., *Sheet conductor model of brain slices for stimulation and recording with planar electronic contacts*. European Biophysics Journal with Biophysics Letters, 2002. **31**(3): p. 228-231.
61. Buitenweg, J., W. Rutten, and E. Marani, *Geometry-Based Finite-Element Modeling of the Electrical Contact Between a Cultured Neuron and a Microelectrode*. Ieee Transactions on Biomedical Engineering, 2003. **50**(4): p. 501-509.
62. Buitenweg, J., et al., *Measurement of Sealing Resistance of Cell-Electrode Interfaces in Neuronal Cultures Using Impedance Spectroscopy*. Medical & Biological Engineering & Computing, 1998. **36**: p. 630-637.
63. Ott, H.C., et al., *Perfusion-decellularized matrix: using nature's platform to engineer a bioartificial heart*. Nature Medicine, 2008. **14**(2): p. 213-221.
64. Larkin, L.M., et al., *Functional evaluation of nerve-skeletal muscle constructs engineered in vitro*. In Vitro Cellular & Developmental Biology-Animal, 2006. **42**(3-4): p. 75-82.
65. Xi, J.Z., J.J. Schmidt, and C.D. Montemagno, *Self-assembled microdevices driven by muscle*. Nature Materials, 2005. **4**(2): p. 180-U67.
66. Rando, T.A. and H.M. Blau, *Primary Mouse Myoblast Purification, Characterization, and Transplantation for Cell-Mediated Gene-Therapy*. Journal of Cell Biology, 1994. **125**(6): p. 1275-1287.
67. Au, H.T.H., et al., *Cell culture chips for simultaneous application of topographical and electrical cues enhance phenotype of cardiomyocytes*. Lab on a Chip, 2009. **9**(4): p. 564-575.
68. Werdich, A.A., et al., *A microfluidic device to confine a single cardiac myocyte in a sub-nanoliter volume on planar microelectrodes for extracellular potential recordings*. Lab on a Chip, 2004. **4**(4): p. 357-362.
69. Reppel, M., et al., *Effect of cardioactive drugs on action potential generation and propagation in embryonic stem cell-derived cardiomyocytes*. Cellular Physiology and Biochemistry, 2007. **19**(5-6): p. 213-224.
70. Wang, Z.L., et al., *Spatial characterization of contracting cardiac myocytes by computer-assisted, video-based image processing*. American Journal of Physiology-Heart and Circulatory Physiology, 1996. **39**(2): p. H769-H779.
71. Delbridge, L.M.D. and K.P. Roos, *Optical methods to evaluate the contractile function of unloaded isolated cardiac myocytes*. Journal of Molecular and Cellular Cardiology, 1997. **29**(1): p. 11-25.
72. Lin, G., et al., *Miniature heart cell force transducer system implemented in MEMS technology*. Ieee Transactions on Biomedical Engineering, 2001. **48**(9): p. 996-1006.
73. Ravenscroft, G., et al., *Dissociated flexor digitorum brevis myofiber culture system - A more mature muscle culture system*. Cell Motility and the Cytoskeleton, 2007. **64**(10): p. 727-738.
74. Lawson, M.A. and P.P. Purslow, *Differentiation of myoblasts in serum-free media: Effects of modified media are cell line-specific*. Cells Tissues Organs, 2000. **167**(2-3): p. 130-137.
75. Peckham, M., *Engineering a multi-nucleated myotube, the role of the actin cytoskeleton*. Journal of Microscopy-Oxford, 2008. **231**(3): p. 486-493.
76. McDevitt, T.C., et al., *In vitro generation of differentiated cardiac myofibers on micropatterned laminin surfaces*. Journal of Biomedical Materials Research, 2002. **60**(3): p. 472-479.

77. Dennis, R.G., et al., *Excitability and contractility of skeletal muscle engineered from primary cultures and cell lines*. American Journal of Physiology-Cell Physiology, 2001. **280**(2): p. C288-C295.
78. Kong, C.H.T., C. Soeller, and M.B. Cannell, *Increasing Sensitivity of Ca²⁺ Spark Detection in Noisy Images by Application of a Matched-Filter Object Detection Algorithm*. Biophysical Journal, 2008. **95**(12): p. 6016-6024.
79. Rohr, S. and B.M. Salzberg, *Multiple-Site Optical-Recording of Transmembrane Voltage (Msortv) in Patterned Growth Heart Cell-Cultures - Assessing Electrical Behavior, with Microsecond Resolution, on a Cellular and Subcellular Scale*. Biophysical Journal, 1994. **67**(3): p. 1301-1315.
80. Bu, G.X., et al., *Uniform Action Potential Repolarization within the Sarcolemma of In Situ Ventricular Cardiomyocytes*. Biophysical Journal, 2009. **96**(6): p. 2532-2546.
81. Kovacs, G.T.A., *Electronic sensors with living cellular components*. Proceedings of the Ieee, 2003. **91**(6): p. 915-929.
82. Khademhosseini, A., et al., *Microfluidic patterning for fabrication of contractile cardiac organoids*. Biomedical Microdevices, 2007. **9**(2): p. 149-157.
83. Itabashi, Y., et al., *Analysis of the electrophysiological properties and arrhythmias in directly contacted skeletal and cardiac muscle cell sheets*. Cardiovascular Research, 2005. **67**(3): p. 561-570.
84. Streit, J., *Mechanisms of pattern generation in co-cultures of embryonic spinal cord and skeletal muscle*. International Journal of Developmental Neuroscience, 1996. **14**(2): p. 137-148.
85. Tschertter, A., et al., *Spatiotemporal characterization of rhythmic activity in rat spinal cord slice cultures*. European Journal of Neuroscience, 2001. **14**(2): p. 179-190.
86. Roos, K.P. and S.R. Taylor, *High-Speed Video Imaging and Digital Analysis of Microscopic Features in Contracting Striated-Muscle Cells*. Optical Engineering, 1993. **32**(2): p. 306-313.
87. Sanderson, M.J., *High-speed digital microscopy*. Methods-a Companion to Methods in Enzymology, 2000. **21**(4): p. 325-334.
88. Daniels, M.P., et al., *Rodent nerve-muscle cell culture system for studies of neuromuscular junction development: Refinements and applications*. Microscopy Research and Technique, 2000. **49**(1): p. 26-37.
89. Springer, M.L., T.A. Rando, and H.M. Blau, *Gene Delivery to Muscle*, in *Current Protocols in Human Genetics*. 2001, John Wiley and Sons, Inc: Hoboken, NJ 07030.
90. Cardoso, J.F. and A. Soudoumiac, *Blind Beamforming for Non-Gaussian Signals*. Ieee Proceedings-F Radar and Signal Processing, 1993. **140**(6): p. 362-370.
91. Hyvärinen, A. and E. Oja, *Independent component analysis: algorithms and applications*. Neural Networks, 2000. **13**(4-5): p. 411-430.
92. Shen, H., S. Jegelka, and A. Gretton, *Fast Kernel-Based Independent Component Analysis*. Ieee Transactions on Signal Processing, 2009. **57**(9): p. 3498-3511.
93. Shi, Z.W. and C.S. Zhang, *Fast nonlinear autocorrelation algorithm for source separation*. Pattern Recognition, 2009. **42**(9): p. 1732-1741.
94. Thomas, J., Y. Deville, and S. Hosseini, *Fast Blind Separation of Long Mixture Recordings Using Multivariate Polynomial Identification*. Ieee Transactions on Signal Processing, 2008. **56**(11): p. 5704-5709.

95. Nackman, L.R. and V. Srinivasan, *POINT PLACEMENT ALGORITHMS FOR DELAUNAY TRIANGULATION OF POLYGONAL DOMAINS*. Algorithmica, 1994. **12**(1): p. 1-17.
96. Tan, J.L., et al., *Cells lying on a bed of microneedles: An approach to isolate mechanical force*. Proceedings of the National Academy of Sciences of the United States of America, 2003. **100**(4): p. 1484-1489.
97. Eilers, J. and A. Konnerth, *Dendritic signal integration*. Curr Opin Neurobiol, 1997. **7**(3): p. 385-90.
98. Hausser, M., N. Spruston, and G.J. Stuart, *Diversity and dynamics of dendritic signaling*. Science, 2000. **290**(5492): p. 739-44.
99. Schaefer, A.T., et al., *Coincidence detection in pyramidal neurons is tuned by their dendritic branching pattern*. J Neurophysiol, 2003. **89**(6): p. 3143-54.
100. Vetter, P., A. Roth, and M. Hausser, *Propagation of action potentials in dendrites depends on dendritic morphology*. J Neurophysiol, 2001. **85**(2): p. 926-37.
101. Elston, G.N., *Pyramidal cells of the frontal lobe: all the more spinous to think with*. J Neurosci, 2000. **20**(18): p. RC95.
102. Koch, C. and I. Segev, *The role of single neurons in information processing*. Nat Neurosci, 2000. **3 Suppl**: p. 1171-7.
103. Poirazi, P. and B.W. Mel, *Impact of active dendrites and structural plasticity on the memory capacity of neural tissue*. Neuron, 2001. **29**(3): p. 779-96.
104. Stuart, G., N. Spruston, and M. Häusser, *Dendrites*. 1999, New York ; Oxford: Oxford University Press. xxi, 376 p.
105. Vetter, P., A. Roth, and M. Hausser, *Propagation of action potentials in dendrites depends on dendritic morphology*. Journal of Neurophysiology, 2001. **85**(2): p. 926-937.
106. Schaefer, A.T., et al., *Coincidence detection in pyramidal neurons is tuned by their dendritic branching pattern*. Journal of Neurophysiology, 2003. **89**(6): p. 3143-3154.
107. Brette, R., et al., *Simulation of networks of spiking neurons: A review of tools and strategies*. Journal of Computational Neuroscience, 2007. **23**(3): p. 349-398.
108. Arendt, T., H.G. Zvegintseva, and T.A. Leontovich, *Dendritic Changes in the Basal Nucleus of Meynert and in the Diagonal Band Nucleus in Alzheimers-Disease - a Quantitative Golgi Investigation*. Neuroscience, 1986. **19**(4): p. 1265-1278.
109. Harrison, P.J., *The neuropathology of schizophrenia - A critical review of the data and their interpretation*. Brain, 1999. **122**: p. 593-624.
110. Kaufmann, W.E. and H.W. Moser, *Dendritic anomalies in disorders associated with mental retardation*. Cerebral Cortex, 2000. **10**(10): p. 981-991.
111. Lewis, D.A., et al., *Altered cortical glutamate neurotransmission in schizophrenia - Evidence from morphological studies of pyramidal neurons*. Glutamate and Disorders of Cognition and Motivation, 2003. **1003**: p. 102-112.
112. Dragunow, M., *Opinion - High-content analysis in neuroscience*. Nature Reviews Neuroscience, 2008. **9**(10): p. 779-788.
113. Uylings, H.B.M. and J. van Pelt, *Measures for quantifying dendritic arborizations*. Network-Computation in Neural Systems, 2002. **13**(3): p. 397-414.
114. Meijering, E., et al., *Design and validation of a tool for neurite tracing and analysis in fluorescence microscopy images*. Cytometry Part A, 2004. **58A**(2): p. 167-176.

115. Pool, M., et al., *NeuriteTracer: A novel ImageJ plugin for automated quantification of neurite outgrowth*. Journal of Neuroscience Methods, 2008. **168**(1): p. 134-139.
116. Popko, J., et al., *Automated analysis of NeuronJ tracing data*. Cytometry A, 2009. **75**(4): p. 371-6.
117. Vallotton, P., et al., *Automated analysis of neurite branching in cultured cortical neurons using HCA-Vision*. Cytometry Part A, 2007. **71A**(10): p. 889-895.
118. Wearne, S.L., et al., *New techniques for imaging, digitization and analysis of three-dimensional neural morphology on multiple scales*. Neuroscience, 2005. **136**(3): p. 661-680.
119. Sholl, D.A., *Dendritic organization in the neurons of the visual and motor cortices of the cat*. J Anat, 1953. **87**(4): p. 387-406.
120. Georges, P.C., et al., *The Yin-Yang of Dendrite Morphology: Unity of Actin and Microtubules*. Molecular Neurobiology, 2008. **38**(3): p. 270-284.
121. Rodriguez, A., et al., *Rayburst sampling, an algorithm for automated three-dimensional shape analysis from laser scanning microscopy images*. Nature Protocols, 2006. **1**(4): p. 2152-2161.
122. Lykissas, M.G., et al., *The role of neurotrophins in axonal growth, guidance, and regeneration*. Current Neurovascular Research, 2007. **4**(2): p. 143-151.
123. McAllister, A.K., *Neurotrophins and neuronal differentiation in the central nervous system*. Cellular and Molecular Life Sciences, 2001. **58**(8): p. 1054-1060.
124. Whitford, K.L., et al., *Molecular control of cortical dendrite development*. Annual Review of Neuroscience, 2002. **25**: p. 127-149.
125. Gorski, J.A., et al., *Brain-derived neurotrophic factor is required for the maintenance of cortical dendrites*. Journal of Neuroscience, 2003. **23**(17): p. 6856-6865.
126. Tolwani, R.J., et al., *BDNF overexpression increases dendrite complexity in hippocampal dentate gyrus*. Neuroscience, 2002. **114**(3): p. 795-805.
127. Danzer, S.C., et al., *Increased expression of brain-derived neurotrophic factor induces formation of basal dendrites and axonal branching in dentate granule cells in hippocampal explant cultures*. Journal of Neuroscience, 2002. **22**(22): p. 9754-9763.
128. Lom, B., et al., *Local and target-derived brain-derived neurotrophic factor exert opposing effects on the dendritic arborization of retinal ganglion cells in vivo*. Journal of Neuroscience, 2002. **22**(17): p. 7639-7649.
129. Patel, M.N. and J.O. McNamara, *SELECTIVE ENHANCEMENT OF AXONAL BRANCHING OF CULTURED DENTATE GYRUS NEURONS BY NEUROTROPHIC FACTORS*. Neuroscience, 1995. **69**(3): p. 763-770.
130. Baker, R.E., et al., *Growth of pyramidal, but not non-pyramidal, dendrites in long-term organotypic explants of neonatal rat neocortex chronically exposed to neurotrophin-3*. Eur J Neurosci, 1998. **10**(3): p. 1037-44.
131. McAllister, A.K., D.C. Lo, and L.C. Katz, *Neurotrophins regulate dendritic growth in developing visual cortex*. Neuron, 1995. **15**(4): p. 791-803.
132. Horch, H.W., et al., *Destabilization of cortical dendrites and spines by BDNF*. Neuron, 1999. **23**(2): p. 353-64.
133. Dijkhuizen, P.A. and A. Ghosh, *BDNF regulates primary dendrite formation in cortical neurons via the PI3-kinase and MAP kinase signaling pathways*. J Neurobiol, 2005. **62**(2): p. 278-88.

134. Jaworski, J., et al., *Control of dendritic arborization by the phosphoinositide-3'-kinase-Akt-mammalian target of rapamycin pathway*. J Neurosci, 2005. **25**(49): p. 11300-12.
135. Kumar, V., et al., *Regulation of dendritic morphogenesis by Ras-PI3K-Akt-mTOR and Ras-MAPK signaling pathways*. J Neurosci, 2005. **25**(49): p. 11288-99.
136. Schrott, G.M., et al., *BDNF regulates the translation of a select group of mRNAs by a mammalian target of rapamycin-phosphatidylinositol 3-kinase-dependent pathway during neuronal development*. J Neurosci, 2004. **24**(33): p. 7366-77.
137. Firestein, B.L., et al., *Cypin: A cytosolic regulator of PSD-95 postsynaptic targeting*. Neuron, 1999. **24**(3): p. 659-672.
138. Akum, B.F., et al., *Cypin regulates dendrite patterning in hippocampal neurons by promoting microtubule assembly*. Nat Neurosci, 2004. **7**(2): p. 145-52.
139. Charych, E.I., et al., *Activity-independent regulation of dendrite patterning by postsynaptic density protein PSD-95*. Journal of Neuroscience, 2006. **26**(40): p. 10164-10176.
140. Carrel, D., et al., *NOS1AP Regulates Dendrite Patterning of Hippocampal Neurons through a Carboxypeptidase E-Mediated Pathway*. Journal of Neuroscience, 2009. **29**(25): p. 8248-8258.
141. Fernandez, J.R., W.J. Welsh, and B.L. Firestein, *Structural characterization of the zinc binding domain in cytosolic PSD-95 interactor [cypin]: Role of zinc binding in guanine deamination and dendrite branching*. Proteins-Structure Function and Bioinformatics, 2008. **70**(3): p. 873-881.
142. Rodriguez-Tebar, A., G. Dechant, and Y.A. Barde, *Binding of brain-derived neurotrophic factor to the nerve growth factor receptor*. Neuron, 1990. **4**(4): p. 487-92.
143. Cannon, R.C., et al., *An on-line archive of reconstructed hippocampal neurons*. Journal of Neuroscience Methods, 1998. **84**(1-2): p. 49-54.
144. Verwer, R.W.H. and J. Vanpelt, *ANALYSIS OF BINARY-TREES WHEN OCCASIONAL MULTIFURCATIONS CAN BE CONSIDERED AS AGGREGATES OF BIFURCATIONS*. Bulletin of Mathematical Biology, 1990. **52**(5): p. 629-641.
145. Vanpelt, J. and R.W.H. Verwer, *GROWTH-MODELS (INCLUDING TERMINAL AND SEGMENTAL BRANCHING) FOR TOPOLOGICAL BINARY-TREES*. Bulletin of Mathematical Biology, 1985. **47**(3): p. 323-336.
146. Verwer, R.W.H. and J. Vanpelt, *TOPOLOGICAL ANALYSIS OF BINARY-TREE STRUCTURES WHEN OCCASIONAL MULTIFURCATIONS OCCUR*. Bulletin of Mathematical Biology, 1985. **47**(2): p. 305-316.
147. Bjaalie, J.G. and S. Grillner, *Global neuroinformatics: The international neuroinformatics coordinating facility*. Journal of Neuroscience, 2007. **27**(14): p. 3613-3615.
148. Yu, W.M., et al., *Quantitative Neurite Outgrowth Measurement Based on Image Segmentation with Topological Dependence*. Cytometry Part A, 2009. **75A**(4): p. 289-297.
149. D'Alessandro, G. *Neuron_Morpho plugin Homepage*. 2007 [cited; Available from: <http://www.personal.soton.ac.uk/dales/morpho/>].
150. Myatt, D.R. and S.J. Nasuto, *Three-Dimensional Reconstruction of Neurons with Neuromantic*. AISB Quarterly. **125**: p. 1-2.
151. Scorcioni, R., S. Polavaram, and G.A. Ascoli, *L-Measure: a web-accessible tool for the analysis, comparison and search of digital reconstructions of neuronal morphologies*. Nat Protoc, 2008. **3**(5): p. 866-76.

152. Ascoli, G.A., D.E. Donohue, and M. Halavi, *NeuroMorpho.Org: A central resource for neuronal morphologies*. Journal of Neuroscience, 2007. **27**(35): p. 9247-9251.
153. Ascoli, G.A., et al., *Generation, description and storage of dendritic morphology data*. Philosophical Transactions of the Royal Society of London Series B-Biological Sciences, 2001. **356**(1412): p. 1131-1145.
154. Ghosh, A. *Sholl Analysis Plugin (v1.0)*. [cited; Available from: <http://biology.ucsd.edu/labs/ghosh/software/index.html>].
155. Gutierrez, H. and A.M. Davies, *A fast and accurate procedure for deriving the Sholl profile in quantitative studies of neuronal morphology*. Journal of Neuroscience Methods, 2007. **163**(1): p. 24-30.
156. Chen, H.X. and B.L. Firestein, *RhoA regulates dendrite branching in hippocampal neurons by decreasing cypin protein levels*. Journal of Neuroscience, 2007. **27**(31): p. 8378-8386.
157. Samsonovich, A.V. and G.A. Ascoli, *Statistical determinants of dendritic morphology in hippocampal pyramidal neurons: A hidden Markov model*. Hippocampus, 2005. **15**(2): p. 166-183.
158. vanPelt, J., A.E. Dityatev, and H.B.M. Uylings, *Natural variability in the number of dendritic segments: Model-based inferences about branching during neurite outgrowth*. Journal of Comparative Neurology, 1997. **387**(3): p. 325-340.
159. Sugimura, K., et al., *Self-organizing mechanism for development of space-filling neuronal dendrites*. Plos Computational Biology, 2007. **3**(11): p. 2143-2154.
160. Tyson, J.J., K.C. Chen, and B. Novak, *Sniffers, buzzers, toggles and blinkers: dynamics of regulatory and signaling pathways in the cell*. Current Opinion in Cell Biology, 2003. **15**(2): p. 221-231.
161. Milosevic, N.T. and D. Ristanovic, *The Sholl analysis of neuronal cell images: Semi-log or log-log method?* Journal of Theoretical Biology, 2007. **245**(1): p. 130-140.
162. Ascoli, G.A., *Neuroanatomical algorithms for dendritic modelling*. Network-Computation in Neural Systems, 2002. **13**(3): p. 247-260.
163. Donohue, D.E. and G.A. Ascoli, *A comparative computer simulation of dendritic morphology*. Plos Computational Biology, 2008. **4**(6): p. -.
164. Scorcioni, R. and G.A. Ascoli, *Algorithmic reconstruction of complete axonal arborizations in rat hippocampal neurons*. Neurocomputing, 2005. **65**: p. 15-22.
165. van Pelt, J. and A. Schierwagen, *Morphological analysis and modeling of neuronal dendrites*. Mathematical Biosciences, 2004. **188**: p. 147-155.
166. Cuntz, H., A. Borst, and I. Segev, *Optimization principles of dendritic structure*. Theor Biol Med Model, 2007. **4**: p. 21.
167. Brown, E.N., R.E. Kass, and P.P. Mitra, *Multiple neural spike train data analysis: state-of-the-art and future challenges*. Nature Neuroscience, 2004. **7**(5): p. 456-461.
168. Buzsaki, G., *Large-scale recording of neuronal ensembles*. Nature Neuroscience, 2004. **7**(5): p. 446-451.
169. Gold, C., et al., *On the origin of the extracellular action potential waveform: A modeling study*. Journal of Neurophysiology, 2006. **95**(5): p. 3113-3128.
170. Martinez, J., et al., *Realistic simulation of extracellular recordings*. Journal of Neuroscience Methods, 2009. **184**(2): p. 285-293.
171. Lewicki, M.S., *A review of methods for spike sorting: the detection and classification of neural action potentials*. Network-Computation in Neural Systems, 1998. **9**(4): p. R53-R78.

172. Adamos, D.A., E.K. Kosmidis, and G. Neophilidis, *Performance evaluation of PCA-based spike sorting algorithms*. Computer Methods and Programs in Biomedicine, 2008. **91**(3): p. 232-244.
173. Fraser, G.W., et al., *Control of a brain-computer interface without spike sorting*. Journal of Neural Engineering, 2009. **6**(5): p. -.
174. Ventura, V., *Spike train decoding without spike sorting*. Neural Computation, 2008. **20**(4): p. 923-963.
175. Wood, F. and M.J. Black, *A nonparametric Bayesian alternative to spike sorting*. Journal of Neuroscience Methods, 2008. **173**(1): p. 1-12.
176. Mtetwa, N. and L.S. Smith, *Smoothing and thresholding in neuronal spike detection*. Neurocomputing, 2006. **69**(10-12): p. 1366-1370.
177. Kim, S. and J. McNames, *Automatic spike detection based on adaptive template matching for extracellular neural recordings*. Journal of Neuroscience Methods, 2007. **165**(2): p. 165-174.
178. Takekawa, T., Y. Isomura, and T. Fukai, *Accurate spike sorting for multi-unit recordings*. European Journal of Neuroscience, 2010. **31**(2): p. 263-272.
179. Geng, X.L., G.S. Hu, and X. Tian, *Neural spike sorting using mathematical morphology, multiwavelets transform and hierarchical clustering*. Neurocomputing, 2010. **73**(4-6): p. 707-715.
180. Shoham, S., M.R. Fellows, and R.A. Normann, *Robust, automatic spike sorting using mixtures of multivariate t-distributions*. Journal of Neuroscience Methods, 2003. **127**(2): p. 111-122.
181. Koning, M., et al., *Current opportunities and challenges in skeletal muscle tissue engineering*. Journal of Tissue Engineering and Regenerative Medicine, 2009. **3**(6): p. 407-415.
182. Meriggioli, M.N. and D.B. Sanders, *Advances in the diagnosis of neuromuscular junction disorders*. Am J Phys Med Rehabil, 2005. **84**(8): p. 627-38.
183. Rich, M.M., *The control of neuromuscular transmission in health and disease*. Neuroscientist, 2006. **12**(2): p. 134-142.
184. Tourovskaia, A., X. Figueroa-Masot, and A. Folch, *Differentiation-on-a-chip: A microfluidic platform for long-term cell culture studies*. Lab on a Chip, 2005. **5**(1): p. 14-19.
185. Kosar, T.F., et al., *A nanofabricated planar aperture as a mimic of the nerve-muscle contact during synaptogenesis*. Lab on a Chip, 2006. **6**(5): p. 632-638.
186. Stett, A., et al., *Biological application of microelectrode arrays in drug discovery and basic research*. Analytical and Bioanalytical Chemistry, 2003. **377**(3): p. 486-495.
187. Sanes, J.R. and J.W. Lichtman, *Development of the vertebrate neuromuscular junction*. Annual Review of Neuroscience, 1999. **22**: p. 389-442.
188. Clark, P., et al., *Alignment of myoblasts on ultrafine gratings inhibits fusion in vitro*. International Journal of Biochemistry & Cell Biology, 2002. **34**(7): p. 816-825.
189. Molnar, P., et al., *Photolithographic patterning of C2C12 myotubes using vitronectin as growth substrate in serum-free medium*. Biotechnology Progress, 2007. **23**(1): p. 265-268.
190. Engler, A.J., et al., *Myotubes differentiate optimally on substrates with tissue-like stiffness: pathological implications for soft or stiff microenvironments*. Journal of Cell Biology, 2004. **166**(6): p. 877-887.

191. Liao, I.C., et al., *Effect of Electromechanical Stimulation on the Maturation of Myotubes on Aligned Electrospun Fibers*. Cellular and Molecular Bioengineering, 2008. **1**(2-3): p. 133-145.
192. Au, H.T.H., et al., *Interactive effects of surface topography and pulsatile electrical field stimulation on orientation and elongation of fibroblasts and cardiomyocytes*. Biomaterials, 2007. **28**(29): p. 4277-4293.
193. Rowlands, A.S., J.E. Hudson, and J.J. Cooper-White, *From scrawny to brawny: the quest for neomusculogenesis; smart surfaces and scaffolds for muscle tissue engineering*. Expert Review of Medical Devices, 2007. **4**(5): p. 709-728.
194. Monti, R.J., R.R. Roy, and V.R. Edgerton, *Role of motor unit structure in defining function*. Muscle & Nerve, 2001. **24**(7): p. 848-866.
195. Hodson-Tole, E.F. and J.M. Wakeling, *Motor unit recruitment for dynamic tasks: current understanding and future directions*. Journal of Comparative Physiology B-Biochemical Systemic and Environmental Physiology, 2009. **179**(1): p. 57-66.
196. Rochlin, K., et al., *Myoblast fusion: When it takes more to make one*. Developmental Biology, 2010. **341**(1): p. 66-83.
197. Bian, W.N. and N. Bursac, *Engineered skeletal muscle tissue networks with controllable architecture*. Biomaterials, 2009. **30**(7): p. 1401-1412.
198. Karlson, W.J., et al., *Automated measurement of myofiber disarray in transgenic mice with ventricular expression of ras*. Anatomical Record, 1998. **252**(4): p. 612-625.
199. Camelliti, P., A.D. McCulloch, and P. Kohl, *Microstructured cocultures of cardiac myocytes and fibroblasts: A two-dimensional in vitro model of cardiac tissue*. Microscopy and Microanalysis, 2005. **11**(3): p. 249-259.
200. Lam, M.T., et al., *The effect of continuous wavy micropatterns on silicone substrates on the alignment of skeletal muscle myoblasts and myotubes*. Biomaterials, 2006. **27**(24): p. 4340-4347.
201. Gingras, J., et al., *Controlling the Orientation and Synaptic Differentiation of Myotubes with Micropatterned Substrates*. Biophysical Journal, 2009. **97**(10): p. 2771-2779.
202. Huang, N.F., et al., *Myotube assembly on nanofibrous and micropatterned polymers*. Nano Letters, 2006. **6**(3): p. 537-542.
203. Bian, W., et al., *Mesoscopic Hydrogel Molding to Control the 3D Geometry of Bioartificial Muscle Tissues*. Nature Protocols, 2009. **4**(10): p. 1522-1534.
204. Razal, J.M., et al., *Wet-Spun Biodegradable Fibers on Conducting Platforms: Novel Architectures for Muscle Regeneration*. Advanced Functional Materials, 2009. **19**(21): p. 3381-3388.
205. Shimizu, K., H. Fujita, and E. Nagamori, *Alignment of Skeletal Muscle Myoblasts and Myotubes Using Linear Micropatterned Surfaces Ground With Abrasives*. Biotechnology and Bioengineering, 2009. **103**(3): p. 631-638.
206. Schnorrer, F. and B.J. Dickson, *Muscle building: mechanisms of myotube guidance and attachment site selection*. Developmental Cell, 2004. **7**(1): p. 9-20.
207. Du, Y.Z., et al., *Astroglia-mediated effects of uric acid to protect spinal cord neurons from glutamate toxicity*. Glia, 2007. **55**(5): p. 463-472.
208. Berdondini, L., et al., *A microelectrode array (MEA) integrated with clustering structures for investigating in vitro neurodynamics in confined interconnected sub-populations of neurons*. Sensors and Actuators B-Chemical, 2006. **114**(1): p. 530-541.
209. Wang, J.Y., et al., *Microfluidics: A new cosset for neurobiology*. Lab on a Chip, 2009. **9**(5): p. 644-652.

210. Pearce, T.M. and J.C. Williams, *Microtechnology: Meet neurobiology. Lab on a Chip*, 2007. **7**(1): p. 30-40.
211. Gross, P.G., et al., *Applications of microfluidics for neuronal studies*. Journal of the Neurological Sciences, 2007. **252**(2): p. 135-143.
212. Cho, S., A. Wood, and M.R. Bowby, *Brain slices as models for neurodegenerative disease and screening platforms to identify novel therapeutics*. Current Neuropharmacology, 2007. **5**(1): p. 19-33.
213. Dutton, E.K., et al., *Acetylcholine-Receptor Aggregation at Nerve-Muscle Contacts in Mammalian Cultures - Induction by Ventral Spinal-Cord Neurons Is Specific to Axons*. Journal of Neuroscience, 1995. **15**(11): p. 7401-7416.
214. Feng, Z.H., S. Koirala, and C.P. Ko, *Synapse-glia interactions at the vertebrate neuromuscular junction*. Neuroscientist, 2005. **11**(5): p. 503-513.
215. Koirala, S., L.V. Reddy, and C.P. Ko, *Roles of glial cells in the formation, function, and maintenance of the neuromuscular junction*. Journal of Neurocytology, 2003. **32**(5-8): p. 987-1002.
216. Rochon, D., I. Rousse, and R. Robitaille, *Synapse-glia interactions at the mammalian neuromuscular junction*. Journal of Neuroscience, 2001. **21**(11): p. 3819-3829.
217. Kobayashi, T., V. Askanas, and W.K. Engel, *Human-Muscle Cultured in Monolayer and Cocultured with Fetal-Rat Spinal-Cord - Importance of Dorsal-Root Ganglia for Achieving Successful Functional Innervation*. Journal of Neuroscience, 1987. **7**(10): p. 3131-3141.
218. Dagberg, B. and B. Alstermark, *Improved organotypic cell culture model for analysis of the neuronal circuit involved in the monosynaptic stretch reflex*. Journal of Neuroscience Research, 2006. **84**(2): p. 460-469.
219. Gahwiler, B.H., et al., *Organotypic slice cultures: a technique has come of age*. Trends in Neurosciences, 1997. **20**(10): p. 471-477.
220. Langowski, B.A. and K.E. Uhrich, *Microscale plasma-initiated patterning (mu PIP)*. Langmuir, 2005. **21**(23): p. 10509-10514.
221. Offenhausser, A. and W. Knoll, *Cell-transistor hybrid systems and their potential applications*. Trends in Biotechnology, 2001. **19**(2): p. 62-66.
222. Pancrazio, J.J., et al., *Development and application of cell-based biosensors*. Annals of Biomedical Engineering, 1999. **27**(6): p. 697-711.
223. Dittami, G.M., et al., *A multilayer MEMS platform for single-cell electric impedance spectroscopy and electrochemical analysis*. Journal of Microelectromechanical Systems, 2008. **17**(4): p. 850-862.
224. Wilson, K., P. Molnar, and J. Hickman, *Integration of functional myotubes with a Bio-MEMS device for non-invasive interrogation*. Lab on a Chip, 2007. **7**(7): p. 920-922.
225. Midrio, M., *The denervated muscle: facts and hypotheses. A historical review*. European Journal of Applied Physiology, 2006. **98**(1): p. 1-21.
226. Bove, M., et al., *Interfacing Cultured Neurons to Planar Substrate Microelectrodes - Characterization of the Neuron-to-Microelectrode Junction*. Bioelectrochemistry and Bioenergetics, 1995. **38**(2): p. 255-265.
227. Dworak, B.J. and B.C. Wheeler, *Novel MEA platform with PDMS microtunnels enables the detection of action potential propagation from isolated axons in culture*. Lab on a Chip, 2009. **9**(3): p. 404-410.
228. Jenerick, H., *An Analysis of the Striated Muscle Fiber Action Current*. Biophys J, 1964. **4**: p. 77-91.

229. Dimitrov, G.V. and N.A. Dimitrova, *Precise and fast calculation of the motor unit potentials detected by a point and rectangular plate electrode*. Medical Engineering & Physics, 1998. **20**(5): p. 374-381.
230. Hammarberg, B. and E. Stalberg, *Novel ideas for fast muscle action potential simulations using the line source model*. Ieee Transactions on Biomedical Engineering, 2004. **51**(11): p. 1888-1897.
231. Egeland, B.M., et al., *Engineering and development of a stable, low-impedance, bioelectrical peripheral nerve interface*. Journal of the American College of Surgeons, 2009. **209**(3): p. S76-S76.
232. Park, B.Y., R. Zaouk, and M.J. Madou, *Fabrication of Microelectrodes Using the Lift-Off Technique*, in *Methods in Molecular Biology*, S.D. Minter, Editor, Humana Press Inc.: Totowa, NJ. p. 23-26.
233. Buitengeweg, J.R., W.L.C. Rutten, and E. Marani, *Extracellular stimulation window explained by a geometry-based model of the neuron-electrode contact*. Ieee Transactions on Biomedical Engineering, 2002. **49**(12): p. 1591-1599.
234. Springer, M.L., T.A. Rando, and H.M. Blau, *Gene Delivery to Muscle*. Current Protocols in Human Genetics, 2001. **13.4**.
235. Stokke, T. and H.B. Steen, *Binding of Hoechst 33258 to Chromatin Insitu*. Cytometry, 1986. **7**(3): p. 227-234.
236. Invitrogen, *α -Bungarotoxin and Conjugates*. Product Information, 2008.
237. Bruneau, E.G., et al., *The effect of agrin and laminin on acetylcholine receptor dynamics in vitro*. Developmental Biology, 2005. **288**(1): p. 248-258.
238. Uhm, C.S., et al., *Synapse-forming axons and recombinant agrin induce microprocess formation on myotubes*. Journal of Neuroscience, 2001. **21**(24): p. 9678-9689.

8 Curriculum Vitae

Education

- 2003** **B.S.E.**, Princeton University, Mechanical and Aerospace Engineering
- 2004** **M.D.**, University of Medicine and Dentistry of New Jersey – Robert Wood Johnson Medical School (In Progress)
- 2010** **Ph.D.**, Rutgers University, Graduate Program in Biomedical Engineering

Major Employment

- 2004** Financial analyst, Citigroup Healthcare Investment Banking
- 2006** Graduate Assistant, Rutgers University – Biomedical Engineering
- 2007** Teaching Assistant, Rutgers University – Biomedical Engineering
- 2008** Graduate Fellow, Rutgers University – Biomedical Engineering

Publications

1. Chen J, Mwenifumbo S, **Langhammer C**, McGovern JP, Li M, Beye A, Soboyejo WO; Cell/surface interactions and adhesion to Ti-6Al-4V: effects of surface texture, J Biomed Mater Res B Appl Biomater. 2007 Aug;82(2):360-73
2. **Langhammer C**, Garg K, Neubauer J, Rosenthal S, Kinzy T; Medical Student Research Exposure via a Series of Modular Research Programs, Accepted – J Investig Med. 2009 Jan;57(1):11-7
3. Previtera ML, **Langhammer CG**, Firestein BL., Effects of substrate stiffness and cell density on primary hippocampal cultures. J Biosci Bioeng., 2010.
4. **Langhammer, C.G.**, J.D. Zahn, and B.L. Firestein, Identification and Quantification of Skeletal Myotube Contraction and Association In Vitro by Video Microscopy. Cytoskeleton, 2010.
5. **Langhammer, C.G.**, et al., Multi-scale Sholl analysis of digitized neurons. Cytometry: Part A, 2010.
6. Previtera ML, **Langhammer CG**, Langrana NA, Firestein BL., Regulation of Dendrite Arborization by Substrate Stiffness is Mediated by Glutamate Receptors. Annals of Biomedical Engineering, 2010.